

January 2015

Solution Routes to Metal Chalcogenide and Zinc Oxide Thin Films for Device Applications

Ruihong Zhang
Purdue University

Follow this and additional works at: https://docs.lib.purdue.edu/open_access_dissertations

Recommended Citation

Zhang, Ruihong, "Solution Routes to Metal Chalcogenide and Zinc Oxide Thin Films for Device Applications" (2015). *Open Access Dissertations*. 1441.
https://docs.lib.purdue.edu/open_access_dissertations/1441

This document has been made available through Purdue e-Pubs, a service of the Purdue University Libraries. Please contact epubs@purdue.edu for additional information.

**PURDUE UNIVERSITY
GRADUATE SCHOOL
Thesis/Dissertation Acceptance**

This is to certify that the thesis/dissertation prepared

By Ruihong Zhang

Entitled

Solution Routes to Metal Chalcogenide and Zinc Oxide Thin Films for Device Applications

For the degree of Doctor of Philosophy

Is approved by the final examining committee:

Carol A. Handwerker

Co-chair

Rakesh Agrawal

Co-chair

Elliott B. Slamovich

Eric P. Kvam

To the best of my knowledge and as understood by the student in the Thesis/Dissertation Agreement, Publication Delay, and Certification Disclaimer (Graduate School Form 32), this thesis/dissertation adheres to the provisions of Purdue University's "Policy of Integrity in Research" and the use of copyright material.

Approved by Major Professor(s): Rakesh Agrawal and Carol A. Handwerker

Approved by: Elliott B. Slamovich

Head of the Departmental Graduate Program

12/1/2015

Date

SOLUTION ROUTES TO METAL CHALCOGENIDE AND ZINC OXIDE FOR
DEVICE APPLICATIONS

A Dissertation
Submitted to the Faculty
of
Purdue University
by
Ruihong Zhang

In Partial Fulfillment of the
Requirements for the Degree
of
Doctor of Philosophy

December 2015
Purdue University
West Lafayette, Indiana

For my parents.

ACKNOWLEDGEMENTS

I would like to thank my advisors, Prof. Carol Handwerker and Prof. Rakesh Agrawal who have given me enormous guidance and support on my research and course work during my doctorate program. By working with them closely, I was inspired by their enthusiasm in research, and learned how to approach a scientific problem and solve engineering problem efficiently. Under their guidance, I have also learned how to build collaboration and how to collaborate with researchers from different fields. They have always show full support on my new research ideas, encourage me to learn new knowledge and skill sets, and willingly share their ideas and perspectives. I am also grateful to my committee members, Prof. Elliott Slamovich and Prof. Eric Kvam. During my first project research work, I was working closely with Prof. Slamovich. He has provided me great guidance and constructive suggestions on the project. I have also enriched my knowledge in materials science and engineering by taking many of Prof. Kvam's engaging classes and have held many great discussions regarding materials science with him. I also appreciate Prof. John Blendell, Prof. Mysore Dayananda, Prof. Eric Stach, and Prof. Kevin Trumble whom I have discussed specific research questions. I definitely have benefited a lot of from those discussions. I would also like to thank Vicki Cline, Patricia Finney, Donna Bystrom, and Melissa Laguire who have assisted me in many of the grueling administrative aspects during my doctorate program at the School of Materials Engineering.

My graduate studies would not be successful without the collaboration and support from my great lab members: Dr. Wei-Chang D. Yang, Dr. Bryce Walker, Caleb Miskin, Dr. Charles Hages, Dr. Nathan Carter, Dr. Erik Sheets, Kevin Brew, Steve McLeod, Xin Zhao, Mark Koeper,

Brian Graeser, Bobby Balow, Robert Boyne, Xianyi Hu, Dr. Hye Yeon Park, Scott McLary, Chinmay Joglekar, and Bethlehem Negash. My research would not be efficient without the hard work and smart minds of my undergraduates: Stephen M. Szczepaniak, Daw Gen Lim, and Seonghyuk Cho. I would like to thank MSE colleague Dr. Wei-Hsun Chen, Dr. Pylin Sarobol, Luthfia Syarbaini, and Shu-han Hsu. I also appreciate having had the opportunity to work with Dr. Patricia Metcalf, Dr. Jiuning Hu, Dr. Sergey Suslov, Dr. Satoshi Ishii, Kim Kisslinger, Priya Murria, and Laurance Cain.

I want to show my deepest appreciation to my parents for their endless love, encouragement, and support to my life, as well as their dedication to my education. I want to thank my families and friends for their love, understanding, support, and friendship.

Lastly, I would like to thank the NSF Solar Economy IGERT program (0903670-DGE), DOE Sunshot Program (No. DE-EE0005328), and NSF-CMMI-0727960, GOALI.

TABLE OF CONTENTS

	Page
LIST OF TABLES	viii
LIST OF FIGURES	ix
ABSTRACT	xviii
CHAPTER 1. INTRODUCTION	1
1.1 Dissertation Organization.....	1
1.2 Principles of Solar Cell Operation	3
1.3 Thin-Film Solar Cells.....	6
1.4 CZTSSe Absorber Materials	7
1.5 Solution-Based Deposition Approaches.....	10
CHAPTER 2. DEPOSITION OF CZTSSE THIN FILMS USING METAL SALT PRECURSOR SOLUTIONS	12
2.1 Motivation.....	12
2.2 Review of Molecular Precursor Routes to CZTSSe Thin Films	13
2.3 Experimental Section	14
2.3.1 Molecular Precursor Preparation	15
2.3.2 Film Deposition and Solvent Evaporation.....	15
2.3.3 Selenization	16
2.3.4 Device Fabrication	17
2.3.5 Characterization.....	18
2.4 Results and Discussion.....	19
2.4.1 CZTSSe Molecular Precursor Solutions	19
2.4.2 Versatility of Primary Amine-Monothiol Solvent Mixtures	20
2.4.3 CZTSSe Solar Cells Processed from Butylamine-Propanethiol Based Precursor Solutions.....	23

	Page
2.4.4 CZTSSe Solar Cells Processed from Hexamine-Propanethiol Based Precursor Solutions.....	29
2.4.5 Optimization of Cu Concentrations.....	38
2.4.6 Solar Cells Processed from Different Metal Salts.....	45
2.4.6.1 Solar Cells Processed from CuCl, ZnCl ₂ , and Sn(acac) ₂ Cl ₂ Precursor Solution.....	45
2.4.6.2 Solar Cells Processed from CuCl ₂ , ZnCl ₂ , and SnCl ₂ Precursor Solution.....	48
2.5 Conclusion.....	52
CHAPTER 3. MICROSTRUCTURAL EVOLUTION DURING ANNEALING AND SELENIZATION.....	53
3.1 Introduction.....	53
3.2 Experimental Section.....	53
3.3 Results and Discussion.....	54
3.3.1 Microstructure of Precursor Films.....	54
3.3.2 Phase Transformation during Selenization.....	55
3.3.3 Solar Cell Performance.....	60
3.4 Conclusion.....	65
CHAPTER 4. DEPOSITION OF METAL CHALCOGENIDE THIN FILMS USING METAL-METAL CHALCOGENIDE PRECURSOR SOLUTIONS.....	66
4.1 Introduction.....	66
4.2 Experimental Section.....	68
4.2.1 Dissolution of Pure Metals and Metal Chalcogenides.....	68
4.2.2 Preparation of CZTSSe Precursor Solutions.....	68
4.2.3 Deposition of Chalcogenide Thin Films.....	70
4.2.4 Thin Film Characterization.....	70
4.2.5 Solar Cell Fabrication and Characterization.....	71
4.3 Results and Discussion.....	72
4.3.1 Dissolution of Pure Metals.....	72
4.3.2 Dissolution and Deposition of Metal Chalcogenides.....	76
4.3.3 Deposition of CZTS and CZTSSe Thin Films.....	78
4.4 Conclusion.....	88
4.5 Supporting Information.....	89

	Page
CHAPTER 5. HYDROTHERMAL GROWTH OF ZNO THIN FILMS	91
5.1 Introduction	91
5.2 Experimental Section	93
5.2.1 Seed Layer Deposition	93
5.2.1.1 Seed Layers Deposited from Nanoparticle Suspensions	93
5.2.1.2 Seed Layers Deposited from Solution Precursors	94
5.2.1.3 Seed Layer Deposited by PLD	94
5.2.2 Solution Growth of ZnO Thin Films	95
5.2.3 Characterization and Measurement	96
5.3 Results and Discussion.....	97
5.3.1 Modification of Anisotropic Growth of ZnO Nanorods.....	97
5.3.1.1 Modification of ZnO Anisotropic Growth using Chloride Ions	98
5.3.1.2 Effects of Solution pH on Anisotropic Growth	110
5.3.1.3 Device Fabrication.....	112
5.3.2 Effects of Seed Layers on ZnO Thin Films.....	115
5.3.2.1 Seed Layer Characteristics	115
5.3.2.2 ZnO Thin Films Grown from Seed Layers.....	119
5.4 Conclusion.....	129
5.5 Supporting Information.....	130
CHAPTER 6. CONCLUSION.....	132
LIST OF REFERENCES	135
VITA	144
PUBLICATIONS.....	145

LIST OF TABLES

Table	Page
Table 2.1: Combinations of primary amine and monothiol for precursor preparation.	22
Table 2.2: Recipes of CZTSSe precursors based on butylamine-propanethiol solvent mixture....	24
Table 2.3: Highest solar cell PCEs obtained from three recipes.	27
Table 2.4 Compositions of precursor film and selenized film.	34
Table 2.5: Recipes of CZTSSe precursor solutions with different [Cu]/[Sn] ratios.	39
Table 2.6: Device characteristics of CZTSSe cells.	43
Table 3.1: Device characteristics of CZTSSe cells.	60
Table 4.1: Conductivities of solvents and Zn solutions at room temperature.	74
Table 4.2: Average compositions of the precursor solution, precursor film, and selenized film...	83
Table 4.3: Dissolution of metals and metal chalcogenides.	89
Table 5.1: Structural properties of ZnO seed layers.	117

LIST OF FIGURES

Figure	Page
Figure 1.1: a) Equivalent circuit, b) J-V characteristics, and c) major parameters of solar cells. ⁵	6
Figure 1.2: Derivation of kesterite crystal structure from diamond cubic structure. ²⁰	8
Figure 1.3: a) Efficiency map on the phase diagram of CZTS, indicating the copper-poor zinc-rich composition is preferred for high efficiency. ²⁵ b) Isothermal section of Cu ₂ S-SnS ₂ -ZnS phase diagram at 670 K. ²³ Area 1 represents the single phase area for CZTS.	9
Figure 2.1: A schematic of solution deposition of thin-film solar cells.....	14
Figure 2.2: A schematic drawing of spin coating and house-made graphite heating chamber in the glovebox. The heating chamber is designed for annealing the as-coated films under Ar/N ₂ /vacuum condition and preventing the deposition of Se/S inside the glovebox. Note that Se/S vapor is highly toxic to humans.	16
Figure 2.3: Picture of tube furnace for selenization. The inset is the layout of selenium pellets and samples in a graphite box.....	17
Figure 2.4: a) Top-view image of the fabricated solar cell. There are six cells on a one-by-one inch substrate. b) The schematic drawing of the solar cell cross-section....	18
Figure 2.5: Images of molecular precursor solutions prepared using hexylamine-propanethiol solvent mixtures. a) <i>Solution A</i> : cation precursor containing CuCl, ZnCl ₂ , and SnCl ₂ with a concentration ratio of [Cu]:[Zn]:[Sn] = 1.53:1.05:1 and [Sn]=0.1 M in hexylamine and propanethiol (vol. ratio 4:1). b) <i>Solution B</i> : chalcogen precursor with a concentration ratio of [S]:[Se]=4:1 [S]+[Se]=2 M in hexylamine and propanethiol (vol. ratio 2:1). c) <i>CZTSSe-1</i> : mixture of <i>Solutions A</i> and <i>Solution B</i> (vol. ratio 5:1). d) <i>CZTSSe-2</i> : mixture of <i>Solution A</i> with another chalcogen precursor with [S]:[Se]=6:1, shown to illustrate color changes with changing [S]:[Se].	20

Figure	Page
Figure 2.6: a) Solutions of cation oxides and cation salts dissolved in hexylamine and propanethiol with a volume ratio of 4:1. The concentrations of all solutions are 0.3 M. b) Solution of metallic zinc in butylamine and propanethiol with a volume ratio of 1:1. The concentration of zinc solution is 0.5 M.	21
Figure 2.7: CZTSSe precursors prepared using oleylamine (OA) and ethanethiol (ET) (vol. ratio 1:1) (left) and butylamine (BA) and propanethiol (PT) (vol. ratio 1:1) (right). In the above CZTSSe precursors, [Cu]:[Zn]:[Sn]:[S+Se] =1.53:1.05:1:4 and [Sn]=0.1 M.....	22
Figure 2.8: a) XRD patterns for CZTSSe precursor films annealed at different temperatures. The precursor films were prepared using <i>Recipe 1</i> in Table 2.2. Note that the final annealing was performed under selenium atmosphere at 500°C for 20 min.	24
Figure 2.8: (Continued) b) Raman spectrum of the CZTSSe precursor film annealed at 220°C for 5 min. c) XRD patterns for the selenized films prepared using three recipes in Table 2.2.	25
Figure 2.9: Top-view SEM images of a) a precursor film prepared using <i>Recipe 1</i> in Table 2.2, and b) film morphology after selenization.	26
Figure 2.10: Statistics of solar cell PCEs prepared using different precursor film thicknesses and recipes shown in Table 2.2.	27
Figure 2.11: Cross-sectional SEM images of device processed using <i>Recipe 1</i> precursor. a) 4-layer precursor film after selenization. The average total thickness is 1.1 μm . The thickness of the large grain layer (LG) is ~ 720 nm while that of the small grain layer (SG) is ~ 380 nm; b) 6-layer precursor film after selenization. The average total thickness is 1.50 μm . The thickness of LG is ~ 330 nm while that of SG is ~ 1.2 μm	28
Figure 2.12: J-V curves of a CZTSSe device fabricated using precursor <i>Recipe 1</i> in Table 2.2. The inset is a top-view SEM image of the selenized film.	28
Figure 2.13: Images of a precursor film and the selenized film on a Mo-sputtered soda-lime glass substrate.	29
Figure 2.14: a) Top-view SEM image of the precursor film fabricated by spin-coating and subsequent annealing, and b) Cross-sectional SEM image of the precursor film.	30
Figure 2.15: EDX linescan along precursor film surface (>10 μm scan) showing compositional uniformity.	30
Figure 2.16: XRD patterns of the precursor film and the selenized film. The standards of kesterite CZTSe (space group: I4 , JCPDS 01-070-8930) and CZTS (space group: I4 , simulated pattern based on JCPDS 01-75-4122) are marked at the bottom of the plot.	32

Figure	Page
Figure 2.17: a) Raman spectra of the precursor film and the selenized film. The Raman standards for CZTS and CZTSe are labeled at the bottom. ^{2,56-58}	32
Figure 2.17: (Continued) Fitted curves of Raman spectra in a).....	33
Figure 2.18: a) Top-view SEM image of large-grain selenized film, and b) fractured cross-section of the CZTSSe device prepared following procedures described in Section 2.3.4.....	33
Figure 2.19: EDX mapping of the CZTSSe device. A platinum coating was employed to protect the film during the preparation of FIB-cross section.	35
Figure 2.20: SEM-EDX linescan on a fractured cross-section of CTZSSe thin film solar cell. The accelerating voltage of electron beam is 10 kV.	36
Figure 2.21: J–V curves and performance parameters for the best performing cell in the dark and under AM1.5 illumination. The dotted line shows the dark current density, while the solid line represents the light current density. The series resistance and shunt resistance under light are listed. The inset is the final device.	37
Figure 2.22: EQE measurement of 7.86% device under 0 V and -1 V bias. The inset shows the band gap estimated using $[\ln(1-EQE)]^2$ versus the photon energy as well as the inflection of the EQE curve. The estimated band gap is 1.08 eV.	38
Figure 2.23: a) XRD and b) Raman spectra of precursor films prepared after annealing. The solvents used in precursors are hexylamine and propanethiol.	41
Figure 2.24: a) XRD and b) Raman spectra of CZTSSe films prepared from molecular precursors with different [Cu]/[Sn] ratios.	42
Figure 2.25: Selenized film processed using <i>Recipe 1</i> (left) and <i>Recipe 4</i> (right) corresponding to [Cu]:[Zn]:[Sn]=1.45:1.05:1 and 1.76:1.05:1, respectively.....	42
Figure 2.26: Statistics of the total area PCEs of CZTSSe solar cells prepared using four precursor solution recipes.	44
Figure 2.27: EQEs for three devices processed from three recipes.	44
Figure 2.28: a) XRD patterns of the precursor and selenized CZTSSe thin films processed using precursor solution with CuCl, ZnCl ₂ , and Sn(acac) ₂ Cl ₂ in hexylamine and propanethiol (vol. ratio as 4:1). The standards of kesterite CZTSe (space group: I4 , JCPDS 01-070-8930) and CZTS (space group: I4 , simulated pattern based on JCPDS 01-75-4122) are marked at the bottom of the plot. The annealing and selenization condition were the same as those reported in the manuscript. b) SEM image of selenized film processed using the above precursor solution.....	46

Figure	Page
Figure 2.29: J–V curves and key parameters for the best performing cell in the dark and under AM1.5 illumination. The dotted line shows the dark current density, while the solid line represents the light current density.	47
Figure 2.30: Solar cell performance of the six cells on the same one-by-one inch substrate. a) PCE, b) V_{oc} , c) J_{sc} , and d) FF.	48
Figure 2.31: a) XRD patterns and b) Raman spectra of precursor and selenized film processed from $CuCl_2$, $ZnCl_2$, and $SnCl_2$ precursor solutions.....	49
Figure 2.32: J–V curves and performance parameters for the best performing cell in the dark and under AM1.5 illumination. The dotted line shows the dark current density, while the solid line represents the light current density. The series resistance and shunt resistance under light are listed. The inset is the final device.	50
Figure 2.33: Solar cell performance of the six cells on the same one-by-one inch substrate. a) PCE, b) V_{oc} , c) J_{sc} , and d) FF.	51
Figure 3.1: TEM images of the annealed precursor film. The scale bar on left image is 5 nm and the scale abr on the right image is 2 nm.	55
Figure 3.2: Top-view and cross-sectional SEM images of CZTSSe films selenized after 5 min, 10 min, 20 min, and 30 min. The scale bar is 1 μm for a)-d) and 500 nm for e)-h.	56
Figure 3.3: a) GIXRD patterns of films selenized for 5 min, 10 min, 20 min, and 30 min (bottom to top). b) magnified diffraction peaks from (112), (220)/(024), and (132)/(116) planes, which are three major XRD peaks from the kesterite structure. The purple lines show the standard peak position of kesterite CZTSe phase (JCPDS 01-070-8930) and the bright pink lines show the simulated standard peak position of kesterite CZTS phase (JCPDS 01-75-4122).	61
Figure 3.4: Raman spectra of the films selenized for 5 min, 10 min, 20 min, and 30 min. The purple lines show the standard peak position of kesterite CZTSe phase (JCPDS 01-070-8930) and the bright pink lines show the simulated standard peak position of kesterite CZTS phase (JCPDS 01-75-4122).	62
Figure 3.5: SEM-EDX linescans on cross-sections of films selenized for 5 min, 10 min, 20 min, and 30 min.	63
Figure 3.6: Schematic process of selenization.	64

Figure	Page
Figure 4.1: a) GIXRD patterns of the as-dried Zn precursor film, the as-annealed Zn precursor film, and the as-annealed Zn+S precursor film. b) ESI negative mode analysis of Zn solution. (Courtesy by Laurance Cain and Priya Murria at Purdue University) The insets are Zn solutions (0.3 and 0.7 M) prepared in BA-EDT and HA-EDT solvent mixtures (vol. ratio as 1:1). c) Saturated solutions of Cu, Zn, Sn, and In in HA-EDT solvent mixtures.....	75
Figure 4.2: Solutions prepared by dissolving Cu ₂ S, CuS, SnS, SnSe, Cu ₂ Se, and CuSe in HA-EDT solvent mixtures with concentrations of 0.3 M at room temperature. The dissolution was performed in a N ₂ -filled glovebox with both water and oxygen level <0.1 ppm.....	77
Figure 4.3: a) GIXRD patterns of CuS precursor films annealed at 150°C, 300°C, and 350°C, respectively. b) Raman spectrum of a CuS thin film recovered at 300°C. c) GIXRD patterns of SnS precursor films annealed at 150°C and 300°C, respectively. d) Raman spectrum of a SnS thin film recovered at 300°C.....	78
Figure 4.4: GIXRD patterns and film morphology of ternary Cu ₂ Sn(S _x Se _{1-x}) ₃ (0 ≤ x ≤ 1) thin films processed using mixture solutions of Cu ₂ S/Cu ₂ Se, SnS/SnSe, and S/Se. The compositions of the thin films are estimated using SEM-EDX. The standard pattern of Cu ₂ SnS ₃ (PDF 01-070-6338) is labeled at the bottom. Based on Vegard's law, x=0.35 in the Cu ₂ Sn(S _x Se _{1-x}) ₃ thin film.....	79
Figure 4.5: Constituent solutions and resulting precursor solutions in three example solution routes to pure CZTS or CZTSSe (left). Schematic of general deposition procedures using the above precursor solutions (right).....	80
Figure 4.6: SEM images (a-d), GIXRD patterns (e), Raman spectra (f) of a precursor film and a selenized film prepared from <i>Solution 1</i> : CZTS precursor solution. a) and c) Top-view and cross-sectional images of a precursor film. b) and d) Top-view and cross-sectional images of a selenized film. Inset in a) is a low-magnification top-view image for the precursor film. A scratch in the upper right corner was intentionally put on to facilitate the focusing in microscope.....	82
Figure 4.7: Results for <i>Solution 2</i> : CZTSSe precursor solution. a) GIXRD patterns of the precursor film and selenized film. b) Raman spectra of the precursor film and selenized film. c) J–V curves and performance parameters for the best performing cell in the dark and under AM1.5 illumination. The dotted line shows the dark current density, while the solid line represents the light current density. d) External quantum efficiency (EQE) of the same cell.....	83

Figure	Page
Figure 4.8: Results for <i>Solution 2</i> : CZTSSe precursor solution. a) STEM-HAADF images of CZTSSe precursor film. b) and c) Elemental distributions of Cu, Zn, Sn, S, and Se within a single layer of precursor film and across several precursor films. The compositional profiling was analyzed using STEM-EDX. The dot lines mark the layers inside the precursor film. d) High-resolution STEM-HAADF images of nanoparticles in the precursor film.	85
Figure 4.9: Results for <i>Solution 2</i> : CZTSSe precursor solution. a) Top-view SEM image of the selenized film. b) and c) cross-sectional SEM image and STEM-HAADF image of a solar cell. d) STEM-EDX compositional profiling along yellow line in c. Note that S K α and Mo L α overlap each other, thus their compositional profiles are the same.	86
Figure 4.10 J-V curves and performance parameters for the best performing cell processed from <i>Solution 3</i> : CZTSS precursor solution. The dotted line shows the dark current density, while the solid line represents the light current density.	87
Figure 4.11: Solutions of Zn, Sn, In, SnS, SnSe, CuS, Cu ₂ S, Cu ₂ Se, In ₂ S ₃ , In ₂ Se ₃ , and Ag ₂ S (left to right) prepared in HA-EDT solvent mixtures at room temperature in air atmosphere. The solution concentrations are 0.2 M.	89
Figure 4.12: TGA trace of SnS solution.	90
Figure 5.1: Atomic model of 3D wurzite structure of ZnO crystal (left side) and 2D atomic projections of (0110) and 0001 planes (right side). The top and bottom exposed 0001 planes can be either O ²⁻ ion-terminated or Zn ²⁺ ion-terminated. The 3D and 2D models are constructed in CrystalMaker software.	92
Figure 5.2: Experiment setup for the hydrothermal growth.	95
Figure 5.3: SEM images of a) a typical ZnO nanoparticle seed layer fabricated on a glass substrate, and b) the array of nanorods formed from the solution of zinc nitrate and HMTA (1:1, 0.05 M, 10 h hydrothermal growth). c) XRD patterns for the seed layer and the array of nanorods. The black and red patterns represent the seed layer and the array of nanorods after hydrothermal growth, respectively. d) Typical HRTEM image of a ZnO nanorod grown on the seed layer.	98
Figure 5.4: SEM images showing the morphology of the ZnO thin films formed on nanoparticle seed layers (glass substrates) from zinc nitrate and HMTA solution with different Cl ⁻ concentrations after 1 h and 5 h growth. a) and b) [Cl ⁻]/[Zn ²⁺]=0; c) and d) [Cl ⁻]/[Zn ²⁺]=1; e) and f) [Cl ⁻]/[Zn ²⁺]=1.5; g) and h) [Cl ⁻]/[Zn ²⁺]=2.	100
Figure 5.5: Plots of a) average rod diameters and b) rod area density in films formed under different conditions.	101

Figure	Page
Figure 5.6: Patches of electron transparent hexagonal plates formed on the top of films grown from solution with $[\text{Cl}^-]/[\text{Zn}^{2+}]=2$. Glass substrate was used.....	103
Figure 5.7: Cross-section images of ZnO films grown from the following solution after 5 h. a) $[\text{Cl}^-]/[\text{Zn}^{2+}]=0$, b) $[\text{Cl}^-]/[\text{Zn}^{2+}]=1$, c) $[\text{Cl}^-]/[\text{Zn}^{2+}]=1.5$, and d) $[\text{Cl}^-]/[\text{Zn}^{2+}]=2$. Pt, NRL, DL, and SL represent ion-beam deposited platinum layer on the top of films, the low density nanorod layer, the dense film layer, and the seed layer, respectively.....	103
Figure 5.8: a) Schematic illustration of the reflection mode GADDS measurement. Equal area inverse pole figures in sample normal directions of films grown in different solution conditions (left to right): b) film grown from solution of zinc nitrate and HMTA (1:1, 0.05 M), 5 h, and film grown from solution with zinc nitrate and HMTA with $[\text{Cl}^-]/[\text{Zn}^{2+}]=1.5$ and $\text{pH}=5.4\pm 0.1$, 5 h; and c) film growth from solution of zinc nitrate and HMTA with $[\text{Cl}^-]/[\text{Zn}^{2+}]=1.5$ and $\text{pH}=4.8\pm 0.1$, 1 h, and film grown from the same solution for 2 h.....	104
Figure 5.9: SEM images of ZnO films grown on nanoparticle seeds (glass substrates) from solution with $\text{Zn}(\text{NO}_3)_2$, HMTA, and NH_4Cl ($[\text{Zn}^{2+}]: [\text{HMTA}]: [\text{Cl}^-]=1:1:1.5$, $\text{pH}=4.8\pm 0.1$). (a) 1 h growth and (b) 2 h growth.....	105
Figure 5.10: XPS full spectra of ZnO thin film surface (without sputtering) and the interior (with ion sputtering). On the sample surface, Cl 2p, C 1s, O 1s, and Zn 2p show up, while inside the sample only O 1s and Zn 2p peaks have significant intensity.....	107
Figure 5.11: XPS spectra of Cl 2p, O1s, and Zn 2p _{3/2} . The ZnO thin film was ion sputtered from the surface to the bottom during the XPS measurement. The spectra going upward from black lines to orange lines were collected with increasing sputtering time. The black lines represent the spectra of the film surface, and the orange lines represent the spectra of the film bottom.	108
Figure 5.12: Schematic illustration of 2D film growth from solution (a) without and (b) with Cl^- ions. The effect of HMTA was drawn based on an article published by Sugunan et al. ¹²⁴	109
Figure 5.13: SEM images of ZnO film acquired from the solution with $[\text{Cl}^-]/[\text{Zn}^{2+}]=1.5$ at 90°C. (a-c) $\text{pH}=4.8\pm 0.1$, adjusted from 5.4 ± 0.1 , (d-f) $\text{pH}=9.9\pm 0.1$, adjusted from 5.4 ± 0.1 . (a, d) for 1 h growth and (b, c, e, and f) for 2 h growth. Films were grown on glass substrates. Pt, DL, PL, and SL represent the ion beam deposited platinum layer, the dense layer, the porous layer, and the seed layer, respectively.	111
Figure 5.14: Focused ion beam images of ZnO films grown on nanoparticle seed layers (glass substrates) from solution with (a) zinc nitrate and HMTA, $[\text{Cl}^-]/[\text{Zn}^{2+}]=0$ and (b) $[\text{Cl}^-]/[\text{Zn}^{2+}]=1.5$, $\text{pH}=4.8\pm 0.1$. NRL, DL, and SL represent the nanorod layer, the dense layer, and the seed layer, respectively.	112

Figure	Page
Figure 5.15: Cross-section of a) a single seed layer on Si wafer (300 nm SiO ₂ /p++ Si wafers) and b) ~100 nm ZnO thin film formed from 15-min hydrothermal growth on the seed layer. Ion-beam Pt and e-beam Pt represent the ion beam deposited and electron beam deposited platinum layers, respectively. DL is the dense layer.....	113
Figure 5.16: a) Transmittance spectrum of ZnO film with ~100 nm thickness on a glass substrate. The inset shows the square on the absorption coefficient versus photon energy. b) Current–voltage characteristics of ZnO film plotted for different back gate biases. Inset shows the configuration of devices.....	114
Figure 5.17: Anisotropic growth of ZnO nanorods from a solution of zinc nitrate and HMTA after 5 h on (a) a seeded glass substrate (nanoparticles with diameter ~70 nm) and (b) an unseeded glass substrate. The inset is morphology of nanorods at higher magnification.....	116
Figure 5.18: Top-view and side-view SEM images of three types of seed layers. a) and b) shows top-view and side-view images of SL1. c) and d) shows top-view and side-view images of SL2. e) shows top-view image of SL3. f) HRTEM image of a nanoparticle formed in SL1.	118
Figure 5.19: XRD patterns of the seed layers. The notation, Si-w, represents the peak/s contributed by SiO ₂ (300 nm)/Si wafers. The peak/s are attributed to the miscut of Si wafer and the existance of crystalline SiO ₂	119
Figure 5.20: p-XRD of films grown on SL1 and SL2 from Solution 1 and Solution 2 and p-XRD of the film grown on SL3 from Solution 1.....	120
Figure 5.21: Top-view SEM images of ZnO films grown on SL1 and SL2 in solution 1. a)-d) films grown on SL1 for 15 min, 30 min, 60 min, and 120 min. e)-h) films grown on SL2 for 15 min, 30 min, 60 min, and 120 min.	124
Figure 5.22: Top-view SEM images of ZnO films grown on SL1 and SL2 in solution 2. a)-d) films grown on SL1 for 15 min, 30 min, 60 min, and 120 min. e)-h) films grown on SL2 for 15 min, 30 min, 60 min, and 120 min.	125
Figure 5.23: Cross-section SEM images of ZnO films grown on SL1 and SL2 in solution 1. a)-d) films grown on SL1 for 15 min, 30 min, 60 min, and 120 min. e)-h) films grown on SL2 for 15 min, 30 min, 60 min, and 120 min.	126
Figure 5.24: Cross-section SEM images of ZnO films grown on SL1 and SL2 in solution 2. a)-d) films grown on SL1 for 15 min, 30 min, 60 min, and 120 min. e)-h) films grown on SL2 for 15 min, 30 min, 60 min, and 120 min.	127
Figure 5.25: a) Average diameters of nanorods (plotted based on Figure 5.27) , b) number density of nanorods, and c) film thickness versus growth time.	128
Figure 5.26 Cross-sectional SEM image of a ZnO film grown from SL3 after 120-min solution growth.	130

Figure	Page
Figure 5.27: Distributions of nanorod diameters in films grown from SL1 and SL2 in Solution 1 (a and c) and Solution 2 (b and d).	131

ABSTRACT

Zhang, Ruihong. Ph.D., Purdue University, December 2015. Solution Routes to Metal Chalcogenides and Zinc Oxide Thin Films for Device Applications. Major Professor: Rakesh Agrawal and Carol A. Handwerker.

Semiconductor thin films and their fabrication methods have been intensively investigated in order to fulfill a wide spectrum of applications in electronic devices, optical devices, and photoelectronic devices. Solution deposition of semiconductor thin films draws increasing attention since it offers low cost, high-throughput production, and better compatibility with flexible or polymeric substrates compared to the vacuum deposition. This dissertation mainly focuses on the solution routes for depositing two groups of semiconductor thin films: kesterite copper zinc tin sulfide/selenide/sulfoselenide ($\text{Cu}_2\text{ZnSn}(\text{S}_{1-x}\text{Se}_x)_4$ ($0 \leq x \leq 1$) (CZTSSe) and zinc oxides (ZnO). The corresponding thin film devices based on the solution routes are also presented.

Compared to fossil fuels, the higher cost of photovoltaic electricity is the main barrier for its extensive application. To advance photovoltaic electricity as a promising energy alternative, the candidate materials and processing routes should be cost effective for beyond terawatt scale. Kesterite CZTSSe is an attractive absorber material since it contains earth-abundant elements (i.e. copper, zinc, tin, and sulfur) and has a high light absorption coefficients (i.e. $10^4 \sim 10^5 \text{ cm}^{-1}$). The molecular solution routes, which offers a facile control of the film composition and the scalability for mass production, has the demonstrated advantages in fabricating CZTSSe thin films. In this study, metal salt precursor solutions and metal-metal chalcogenide precursor solutions based on versatile amine-thiol solvent mixtures are developed to deposit high-quality CZTSSe thin films, and solar cells with power conversion efficiencies (PCEs) more than 8% and 7% are fabricated

based on the corresponding solution routes, respectively. The effects of the metal salts, the solvents, and the precursor compositions (e.g. Cu/Sn ratios) on the PCEs are studied systematically in order to achieve better solar cell performances. The microstructural evolution of solution-processed CZTSSe precursor films during the selenization is examined, and a mechanism is proposed to explain the rapid microstructural and compositional changes as well as the formation of fine-grained layers during the selenization. In addition, the versatility of using the amine-thiol solvent system in depositing semiconductor thin films is illustrated in terms of the rapid dissolution of bulk metals, metal salts, organometallic compounds, and metal chalcogenides at room temperature in this solvent system, and the deposition of binary, ternary, and quaternary metal chalcogenide thin films from the as-dissolved or combined precursor solutions. The molecular precursor route based on this versatile solvent system opens a door for low-cost fabrication of semiconductor thin films.

Solution-processed ZnO thin films are promising candidates for cost-effective thin film electronics. In this study, an aqueous solution route is utilized to grow ZnO thin films with different morphologies at low temperature (90°C). Effects of the seed layers and solution conditions on morphologies of individual ZnO nanorods and thin films are investigated. Particularly, this study presents a solution method to modify the anisotropic growth behavior of hexagonal ZnO, which successfully results in a two-dimensional continuous polycrystalline film within a short-time growth. This method is then applied to the fabrication of ZnO thin film transistors. Continuous active layers with thicknesses of ~ 100 nm are acquired with solution growth for 15 min. The applicability of this method for low-cost transparent thin film transistors is demonstrated in terms of film microstructure, film transmittance, and device I-V measurements.

CHAPTER 1. INTRODUCTION

1.1 Dissertation Organization

This dissertation focuses on the molecular precursor routes to deposit metal chalcogenide thin films for photovoltaic (PV) application (Chapter 1-4), and the hydrothermal growth of ZnO thin films for transparent electronic device application (Chapter 5). Chapter 1 introduces the principles of solar cell operation and key parameters representing the performance of solar cells; reviews the advantages of thin-film solar cell technology over crystalline-silicon based photovoltaics; and summarizes the properties of earth-abundant $\text{Cu}_2\text{ZnSn}(\text{S}_{1-x}\text{Se}_x)_4$, $0 \leq x \leq 1$ (CZTSSe) absorber materials. In addition, the deposition methods for kesterite CZTSSe are reviewed, with an emphasis on why solution deposition has the potential to advance PV technology to the terawatt scale.

Chapters 2-4 focus on two non-hydrazine molecular precursor routes, which are based on a versatile amine-thiol solvent system for the deposition of CZTSSe, and other metal chalcogenide thin films. Chapter 2 reports the fabrication of CZTSSe solar cells using metal salt precursor solutions. The detailed procedures of this developed solution route, including the precursor preparation, film deposition, solvent evaporation, and selenization, are described. The microstructures, compositions, and phases of fabricated kesterite thin films are reported along with the corresponding solar cell power conversion efficiencies (PCEs). Currently, solar cell efficiency of 8.09% has been achieved for a cell area of 0.456 cm^2 under standard AM 1.5 illumination. In Chapter 2, the versatility of the amine-thiol solvent mixture is also illustrated by a series of dissolution experiment.

Chapter 3 further discusses the phase transformation and microstructural evolution of CZTSSe precursor films during the solvent evaporation/annealing as well as the selenization. The phase and composition of the annealed films are characterized using transmission electron microscope (TEM) and scanning transmission electron microscope (STEM) equipped with energy dispersive X-ray detector (EDX). The microstructural evolution during the selenization process is captured by selenizing a series of precursor films for different periods of time. The film structures and compositions are characterized using a scanning electron microscope (SEM) equipped with EDX. The phases formed at different selenization periods are characterized using X-ray diffraction (XRD) and Raman spectroscopy. The results of this ex-situ study reveals the mechanism of the grain growth and phase transformation of molecular precursor-processed films during heat treatment.

Chapter 4 introduces another molecular precursor route based on metal-metal chalcogenide precursor solutions. Since the versatile amine-dithiol solvent mixtures enables the rapid dissolution of pure metals (e.g. Cu, Zn, Sn, and In) and metal chalcogenides (e.g. CuX, SnX, Cu₂X, In₂X₃, etc., X=S or Se) at high concentrations, specific metal-metal chalcogenide precursor solutions are designed for the deposition of multinary chalcogenide thin films (e.g. CuS, SnS, Cu₂Sn(S_{1-x}Se_x)₃ (0 ≤ x ≤ 1), and CZTS/CZTSSe). The practicality of using this solution route to replace hydrazine-based solution route is demonstrated by the fabrication and characterization of CZTSSe thin-film solar cells.

Chapter 5 reports a low-cost hydrothermal growth method to produce continuous and dense ZnO polycrystalline films. Aiming to grow densely-packed ZnO thin films for applications such as active layers in thin-film transistors (TFTs) or transparent conductive layers (TCOs) in solar cells, the nucleation and crystal growth of individual nanorods are well-controlled. Systematic studies on the effects of seed layers and additive ions (i.e. chloride ions) to the final film structures are performed, leading to an optimized low-temperature hydrothermal growth method for dense ZnO thin films.

1.2 Principles of Solar Cell Operation

The photovoltaic effect is a conversion process in which electricity is generated from light when a semiconductor is exposed to sunlight. This photovoltaic energy conversion in solar cells consists of two essential steps: the photogeneration of electron-hole pairs in the absorber layer, and the separation of the electron-hole pairs due to the built-in electric field provided by the p-n junction in a solar cell. For the standard AM 1.5 solar spectrum, the ideal band gap (E_g) of absorber materials is 1~1.5 eV.¹⁻⁴

The physics and performance characteristics of solar cells in response to applied bias and light are introduced in the following paragraphs. When sunlight shines on the solar cell, all the light with $E > E_g$ is absorbed, and one electron-hole pair is generated by the absorption of each photon. The built-in electric field across the p-n junction decreases local recombination and facilitates carrier separation. The voltage resulting from this electric field is called the built-in bias (V_{bi}). Under equilibrium condition (i.e. no external bias and no illumination), the diffusion current of majority carriers across the junction is balanced by the drift current of minority carriers back across the junction. The V_{bi} bias is influenced by the doping level of both sides in the p-n junction:

$$V_{bi} = \frac{k_B T}{q} \ln \left(\frac{N_d N_a}{n_i^2} \right) \quad (\text{Equation 1.1})$$

where k_B is Boltzmann's constant, T is temperature in Kelvin, N_d is the concentration of donor atoms, and N_a is the concentration of acceptor atoms.

The net electric field (V_j) can be changed by applying an external bias (V , bias applied to the p-side) across the p-n junction. Then the net electric field, V_j , is given by $V_j = V_{bi} - V$. When a forward bias is applied across the p-n junction, the net electric field in the depletion region is decreased. The barrier to the diffusion of carriers from one side to another is reduced, thus the diffusion current from the majority carriers increases. The drift current is unchanged due to the limited number of minority carriers generated within a diffusion length away from the edge of the depletion region or

inside the depletion region. When the reverse bias is applied across the p-n junction, the net electric field at the depletion region increases, resulting in a higher resistance to the diffusion of majority carriers. While the diffusion current decreases dramatically, the drift current increases slightly, due to the increased depletion region. The drift current is still limited by the generation of minority carriers, thus the total drift current is low. These current density-voltage (J-V) characteristics are known as the diode behavior and can be described by the following equation:

$$J_{dark} = J_0 \left(e^{\frac{qV}{k_B T}} - 1 \right) \quad (\text{Equation 1.2})$$

where J_0 is a constant, k_B is Boltzmann's constant, T is temperature in Kelvin, and m is the ideality factor. For an ideal diode $m=1$ and for non-ideal thin-film solar cells $1 < m < 2$.

When a p-n junction is exposed to illumination, the p-n junction operates in superposition.⁵ An ideal solar cell can be represented by a current source connected in parallel with a rectifying diode (Figure 1.1a). The J-V characteristics can be obtained from the corresponding characteristic of a diode in the dark by shifting the diode characteristic along the current density axis by the light-generated current, J_L . The overall current density inside the solar cell is equal to the summation of the photogenerated current and the dark current, as shown in:

$$J(V) = J_{dark}(V) - J_L \quad (\text{Equation 1.3})$$

For an ideal diode, the equation can be written as

$$J(V) = J_0 \left(e^{\frac{qV}{k_B T}} - 1 \right) - J_L \quad (\text{Equation 1.4})$$

For non-ideal thin-film solar cells, the J-V behavior is different from the typical crystalline Si and III-V solar cells due to the parasitic resistance, thus a more general equation is used to describe the J-V characteristics according to Hegedus et al.:⁶

$$J(V) = J_0 e^{\frac{q(V-RJ)}{mk_B T}} + GV - J_L \quad (\text{Equation 1.5})$$

where R represents the series resistance and G represents the shunt conductance. J_0 is the diode current which is equal to

$$J_0 = J_{00} \exp\left(-\frac{\Phi_b}{mk_B T}\right) \quad (\text{Equation 1.6})$$

with the barrier height Φ_b and prefactor J_{00} corresponding to the specific recombination mechanism dominating the forward current J_0 . For $G \ll J_0/V_{oc}$, the open-circuit voltage is given by:

$$V_{oc} = \frac{\Phi_b}{q} - \frac{mk_B T}{q} \ln\left(\frac{J_{00}}{J_L}\right) \quad (\text{Equation 1.7})$$

The measurement of the current density-voltage (J-V) characteristics is commonly performed under a standard illumination condition, 100 mW/cm² AM 1.5 spectrum at 25°C. Typical parameters indicating the solar cell performance are short circuit current (J_{sc}), open circuit voltage (V_{oc}), fill factor (FF), power conversion efficiency (PCE, η), and quantum efficiency (QE). Parasitic resistance, series resistance (R_s) and shunt resistance (R_{sh}), directly influence the PCE. In an ideal case, the solar cell short circuit current is equal to the photocurrent. The J-V characteristics of a solar cell are shown in Figure 1.1b. FF is defined by the ratio between the maximum power density ($P_{max}=J_{max} \times V_{max}$) and the product of J_{sc} and V_{oc} (Figure 1.1c):

$$FF = \frac{J_{max} V_{max}}{J_{sc} V_{oc}} \quad (\text{Equation 1.8})$$

The power conversion efficiency (η) represents the highest fraction of the incident sunlight energy that has been converted into electricity power. It is described as:

$$\eta = \frac{FF J_{sc} V_{oc}}{P_{incident}} \quad (\text{Equation 1.9})$$

where the $P_{incident}$ is the incident power.

The quantum efficiency (QE) represents the number of electrons collected by the solar cell per incident photon at each wavelength. QE drops to zero beyond the wavelength corresponding to the band gap of the absorber material. The external quantum efficiency (EQE) includes the effect of both the electronic losses during photogeneration and collection in the absorber; and the optical losses refer to the absorption and reflection in window, transparent conductor, and other layers. Since the optical losses do not change with the applied biases, comparing the external quantum

efficiencies at different biases is meaningful to separate the electronic losses and the optical losses, providing insight into the recombination mechanism in the solar cells. Ideally, the photocurrent can be calculated by integrating EQE with respect to the wavelength.

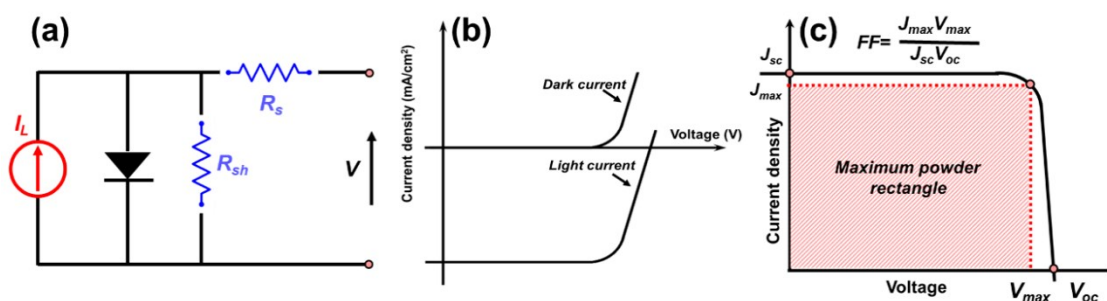


Figure 1.1: a) Equivalent circuit, b) J-V characteristics, and c) major parameters of solar cells.⁵

1.3 Thin-Film Solar Cells

In the current photovoltaic market, over 80% of solar cells are silicon-based solar cells.⁷ The record efficiency for the single-junction crystalline silicon solar cells is 25.6%.⁶ Compared to the conventional silicon technology, thin-film solar cells have several advantages. Firstly, the absorber layer, which normally is a direct-band gap semiconductor, has a higher light absorption coefficient ($10^4 \sim 10^5 \text{ cm}^{-1}$) than crystalline silicon. Sunlight absorbed by silicon with thickness $>100 \text{ }\mu\text{m}$ can be effectively absorbed by only 1-2 μm of those materials.^{4,8,9} The cost of raw materials and handling expense can be reduced significantly due to the thin-film structure. Secondly, thin-film solar cells are compatible with flexible substrates for portable devices.^{6,10} Lastly, the typical absorber layers of thin-film solar cells are polycrystalline films. The grain boundaries in this structure are less active as recombination centers compared to silicon-based solar cells.¹¹ Therefore, low-cost solution-based deposition also can process high-efficiency thin-film solar cells, making the price of photovoltaics competitive to fossil energy.

Commercially, typical materials used in thin-film technology include CdTe and Cu(In,Ga)(S,Se)₂ (CIGSSe). Their record efficiencies are both 20.1%.^{12,13} The issue of elemental abundance and the presence of heavy metal cadmium are drawbacks for these two inorganic absorber materials. Perovskite solar cells are emerging thin-film solar cells which contain a hybrid organic-inorganic lead or tin halide-based material as absorber layers. The lab record achieved for perovskite solar cells is 15%.^{14,15} However, compared to the inorganic absorbers, these absorbers are very air sensitive and unstable.¹⁶ Additional protection layers or special module designs are required for practical manufacturing.

Kesterite copper zinc tin sulfide/selenide/sulfoselenide, Cu₂ZnSn(S,Se)₄, has been recognized as one of the most promising absorber materials to replace CdTe and CIGSSe in thin-film PV technologies. Compared to these two materials, elements required in CZTSSe are more earth-abundant. For example, the abundance of tellurium, indium, and gallium in the earth crust is between 0.001 ppm and 0.05 ppm, while the abundance of copper, zinc, tin, sulfur, and selenium are 50, 75, 2.2, 260, and 0.05 ppm.¹⁷ In addition, increasing demand for indium from the growing display industry for the production of transparent conductive coatings, poses a threat to cost savings for the thin-film solar cells industry. In order to advance PV technology to the terawatt scale, the use of earth-abundant absorbers like CZTSSe is highly favored.

1.4 CZTSSe Absorber Materials

Kesterite copper zinc tin sulfide, selenide and sulfoselenide, Cu₂ZnSnS₄ (CZTS), Cu₂ZnSnSe₄ (CZTSe), Cu₂ZnSn(S,Se)₄ (CZTSSe) are attractive absorber materials that have been well-studied, since they contain earth-abundant elements, and have higher absorption coefficients ($>10^4 \text{ cm}^{-1}$) than silicon.^{1-4,8,9,18-20} The bandgap of the CZTSSe thin films can be tuned from 1.0 to 1.5 eV by varying the sulfur to selenium ratio. The kesterite structure of CZTS/CZTSSe/CZTSe can be derived from the diamond cubic structure of silicon simply by ion substitution.²⁰ For example,

kesterite structure can be formed by substituting two III-group cations with one II-group cation and one IV-group cation from the chalcopyrite structure, as shown in Figure 1.2. In this kesterite structure, planes containing cations $\text{Cu}+\text{Zn}/\text{Cu}+\text{Sn}/\text{Zn}+\text{Cu}/\text{Sn}+\text{Cu}$ alternatively stack along the $\langle 001 \rangle$ direction. As quaternary compounds, kesterite CZTS/CZTSe/CZTSSe contain many lattice defects, vacancies, antisites, and interstitials. The deep-level antisite defects (e.g. Cu_{Zn} and Cu_{Sn}) are responsible for V_{oc} loss. Empirical studies reveal that a copper-poor, zinc-rich composition is desired for high-efficiency CZTSSe solar cells, as depicted in Figure 1.3a, since the concentration of shallow V_{Cu} relative to Cu_{Zn} can be enhanced using this copper-poor zinc-rich growth condition.^{2,20-22} In addition to bulk defects, the formation of secondary phases is another challenge when processing CZTSSe thin-film solar cells. Figure 1.3b is a pseudoternary phase diagram for $\text{Cu}_2\text{S}-\text{ZnS}-\text{SnS}_2$ system. It shows that a few mol% deviation from the compositions within the central area 1 will result in the formation of secondary phases such as Cu_2S , ZnS , SnS_2 , and Cu_2ZnS_3 along with CZTS. The formation of those secondary phases will result in lower bandgap and lower shunt resistance. Furthermore, since the desired copper-poor and zinc-rich condition has deviated from the formula stoichiometry, a precise control in composition during processing of CZTSSe is extremely important.²²⁻²⁴

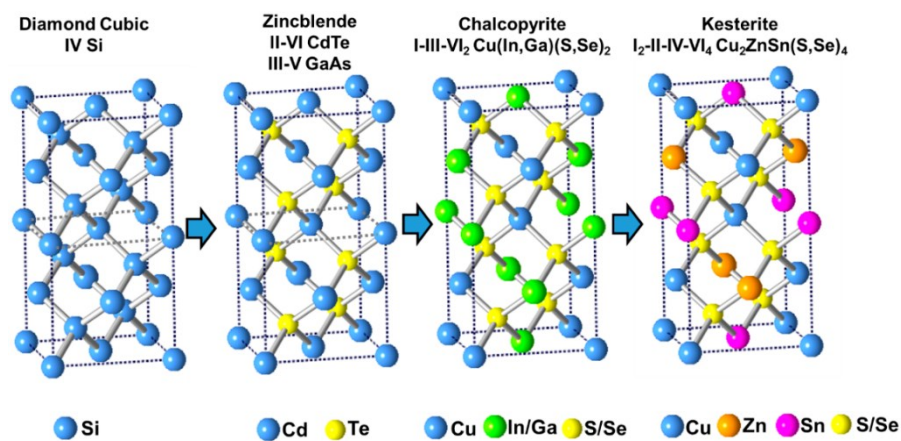


Figure 1.2: Derivation of kesterite crystal structure from diamond cubic structure.²⁰

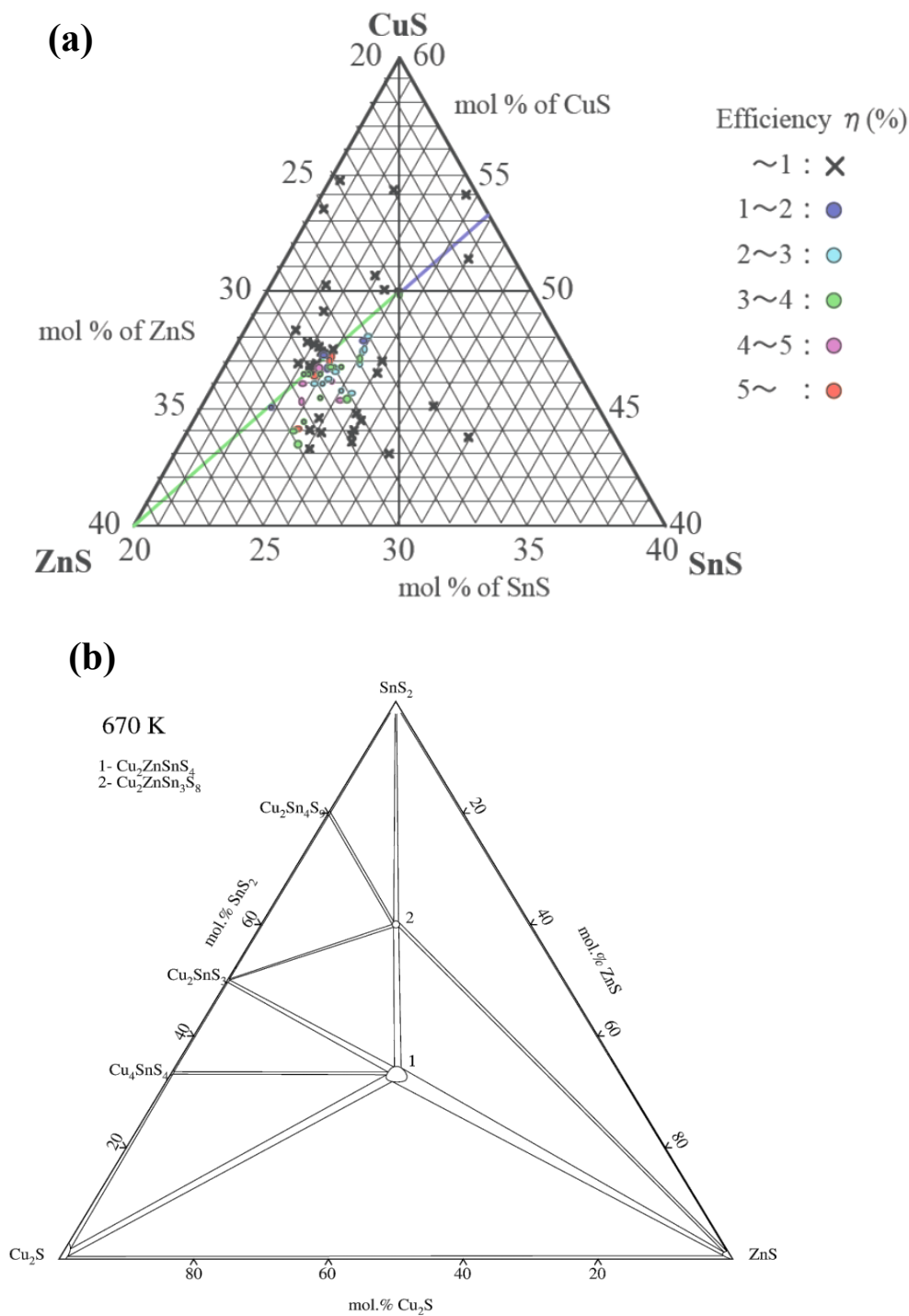


Figure 1.3: a) Efficiency map on the phase diagram of CZTS, indicating the copper-poor zinc-rich composition is preferred for high efficiency.²⁵ b) Isothermal section of Cu_2S - SnS_2 - ZnS phase diagram at 670 K.²³ Area 1 represents the single phase area for CZTS.

1.5 Solution-Based Deposition Approaches

Sputtering and evaporation are two prevailing vacuum-based deposition approaches for CZTS/CZTSSe/CZTSe thin films.^{4,8,19,26-30} For co-sputtered CZTSSe thin films, the current record PCE is 9.3%, according to Chawla et al.²⁶ For the co-evaporation method, Repin et al. from NREL reported the record PCE of 9.1% for CZTSe films¹⁹ and Shin et al. from IBM reported the record PCE of 8.4% for CZTS films.²⁸ Although the above vacuum-based methods have resulted in good efficiencies for CZTSSe-family solar cells, the difficulty in controlling the volatile species and the consequent formation of secondary phases still limit the quality of resulting films.^{19,30} In contrast, solution-based deposition not only offers a low-cost process, but also produces solar cells with even higher efficiencies than sputtering or evaporation approaches. Solution-based deposition can be further divided into two categories: colloidal deposition^{3,31-37} and molecular precursor deposition.³⁸⁻⁴³ Guo et al. first synthesized CZTS nanoparticles and processed CZTSSe solar cells with CZTS inks.³² As reported by Miskin et al., the highest efficiency using this colloidal method was 9.0%.³⁴ With the addition of Ge in the lattice of CZTS nanoparticles, Hages et al. processed CZTGeSSe solar cells with higher V_{oc} and PCE of 460 mV and 9.4%, respectively.⁴⁴ Compared to the above colloidal method, the direct solution method, in which molecular precursor solutions are directly used for the deposition of absorber layers, has the advantages in i) simplifying the fabrication procedures; ii) improving the compositional uniformity; and iii) eliminating/reducing the carbon-species contamination from long-chain ligands used for nanoparticle synthesis.^{17,32,33} The most successful direct solution method so far is based on hydrazine solutions developed by IBM.^{40-42,45,46} The champion device for CZTSSe thin-film solar cell was processed using a hydrazine solution, which contains Cu_2S , $SnSe$, S , and Se . The PCE achieved is 12.6% in a total area of 0.42 cm^2 with $V_{oc}=513\text{ mV}$, $J_{sc}=35.2\text{ mA/cm}^2$, and $FF=69.80\%$.⁴⁶ This result indicates the promise of using a pure solution to deposit device-quality and multinary-chalcogenide thin films. Despite this huge success, researchers have been striving to find alternate low-toxicity and environment-friendly solvent

systems to replace hydrazine, since hydrazine is highly toxic and dangerously unstable. This is also one of the important motivation for developing new solution method for CZTSSe deposition in this dissertation.

CHAPTER 2. DEPOSITION OF CZTSSE THIN FILMS USING METAL SALT PRECURSOR SOLUTIONS

2.1 Motivation

Solution-based deposition of CZTSSe materials offers a number of potential advantages over vacuum deposition in terms of lower cost of raw materials and equipment, higher throughput production, and better compatibility with flexible substrates. Solution-based deposition can be further divided into two groups: colloidal deposition^{3,31-37} and molecular precursor deposition.^{38-43,46} Compared to the colloidal deposition method, the molecular precursor method offers the potential of eliminating/reducing the undesired fine grain layer that results from residual carbon-containing capping ligands and the compositional non-uniformity of nanoparticles.^{34,47,48} Meanwhile, by circumventing additional steps associated with the nanoparticle synthesis, it offers a facile control of the thin-film composition, and promises the scalability for mass production. With a hydrazine-based slurry and a hydrazine-based pure solution, IBM has achieved a record power conversion efficiency of 11.1% and 12.6%, respectively, for kesterite CZTSSe solar cells.^{42,46} Despite its efficacy, hydrazine is highly toxic and dangerously unstable, and thus various handling precautions are required during film preparation. Developing alternate CZTSSe molecular precursors that are more cost-effective, have lower toxicity, and produce higher efficiencies than hydrazine-based solutions is the motivation of this study.

2.2 Review of Molecular Precursor Routes to CZTSSe Thin Films

Currently, a few non-hydrazine approaches have been adopted to deposit CZTSSe thin films. They can be grouped into three major categories: hydrazine-derivative solution approaches,^{49,50} metal salts/thiourea-based solution approaches,^{39,43,51} and metal oxide-based solution approaches.^{52,53} As an example of the first approach, Hsu et al. used hydrazinocarboxylic acid to dissolve zinc powders, which enabled the preparation of pure solution precursor containing hydrazinium chalcogenides of copper, zinc, and tin; and this resulted in a solar cell efficiency of 7.2% on a cell area of 0.12 cm².⁴⁹ Unfortunately, this approach still relies on the reaction between the metal chalcogenides and hydrazine to form the hydrazinium metal complexes as solutes in the ethanolamine/dimethylsulfoxide-based precursor. Among all the studies using thiourea as the sulfur source, Xin et al. obtained the highest power conversion efficiency, i.e., 8.32%, on an active area of 0.43 cm².⁴³ It is interesting to note that in terms of human toxicity, the lowest toxicity solutions reported for the direct solution approach are ethanol-water based solution with dissolved metal salts and thiourea; the highest efficiency obtained for such a method is 5.29%.⁵¹ In the third category of using metal oxides as metal sources, Tian et al. dissolved copper (I) oxide, zinc oxide, and tin (II) oxide in a mixture of 2-methoxyethanol, thioglycolic acid, and monoethanolamine; achieving a solar cell efficiency of 6.83% on an active area of 0.368 cm².⁵²

A simple solution-based approach for the deposition of Cu₂ZnSn(S,Se)₄ using a primary amine-monothiol mixture is developed in this study. The versatility of this solvent mixture in dissolving different cation sources and chalcogens opens a door to a variety of metal chalcogenide molecular precursor designs. The process involves incorporating the metal sources and chalcogens into a primary amine-monothiol solvent mixture at room temperature, spin coating a precursor film, and heat treating the precursor films in both an inert gas and selenium atmosphere.⁵⁴ With this solution approach, high-quality kesterite CZTS and CZTSSe thin films were formed after low-temperature

annealing and selenization. Solar cells were fabricated based on these CZTSSe thin films, resulting in a total area power conversion efficiency of 8.09% for a cell area of 0.456 cm² under standard AM 1.5 illumination.⁵⁵

2.3 Experimental Section

The fabrication of the CZTSSe solar cell using the developed solution route includes four procedures as depicted in Figure 2.1. The whole approach includes four steps: precursor preparation, film deposition and solvent evaporation, high-temperature selenization, and device fabrication. The details for each step are described as follows.

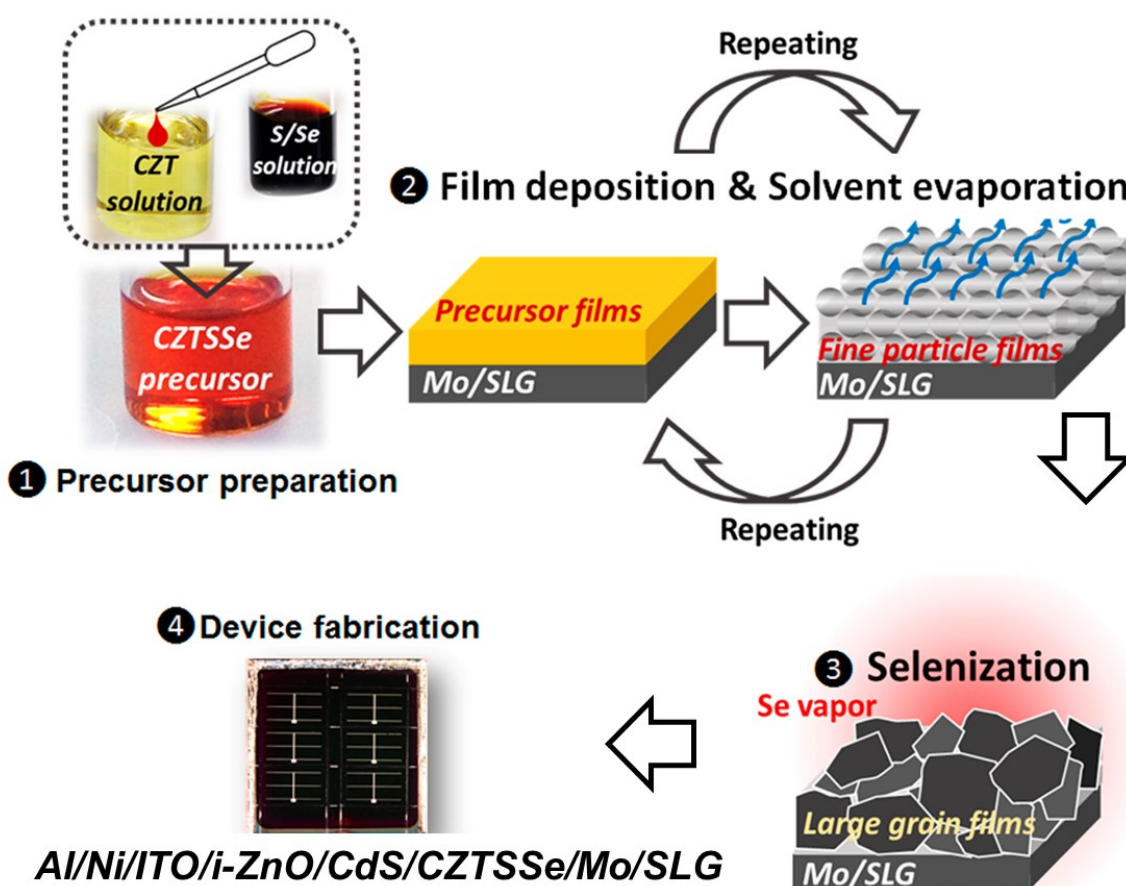


Figure 2.1: A schematic of solution deposition of thin-film solar cells.

2.3.1 Molecular Precursor Preparation

In the present work, “molecular precursor” or “precursor solution” refers to a pure solution in which the elements are homogeneously mixed at a molecular level. The CZTSSe molecular precursors were prepared by dissolving the cation sources and elemental chalcogens in a solvent mixture of a primary amine and a monothiol. The general preparation procedures for CZTSSe precursor solutions are: 1) dissolving the cation sources in a mixture of primary amine/s and monothiol/s to prepare *solution A*; 2) dissolving the anion sources in a mixture of primary amine/s and monothiol/s to prepare *solution B*. Here, the cation sources refer to elemental metals (Zn, Cu, etc.), metal salts (Cu(OAc)₂, CuCl, SnCl₂, etc.), organometallic complexes (Cu(acac)₂, Sn(acac)₂Cl₂, etc.), and metal oxides (ZnO, Cu₂O, SnO, etc.). The anion sources refer to elemental sulfur (S) and selenium (Se). The primary amine can be butylamine, hexylamine, etc. and the monothiol can be ethanethiol, propanethiol, etc. The solvent mixture can be with one or more types of primary amine and monothiol; 3) mixing cation and anion precursors at a specific volume ratio to prepare *CZTSSe precursor solution*. Solution conditions are optimized in order to obtain high-efficiency solar cells. Herein, the solution condition refers to the types of dissolved cation/anion sources, the concentrations of Cu and Zn with respect to Sn, the absolute concentrations of Sn, the types of primary amine/s and monothiol/s in the solvent mixture, and the amine/thiol volume ratios.

2.3.2 Film Deposition and Solvent Evaporation

The CZTSSe precursor solution was spin coated on a one-by-one inch molybdenum-sputtered (~800 nm) soda lime glass (SLG) substrate. After spin coating a layer, the coated layer was annealed inside a heating chamber with an argon atmosphere at 250°C for 5 mins in order to evaporate the solvents. This coating step was repeated until the desired film thickness was obtained. The film deposition and solvent evaporation procedure is performed inside a nitrogen glovebox

with < 0.1 ppm water and oxygen. Figure 2.2 shows the designed heating chamber, as well as the spin coating and solvent evaporation setup in the glovebox.

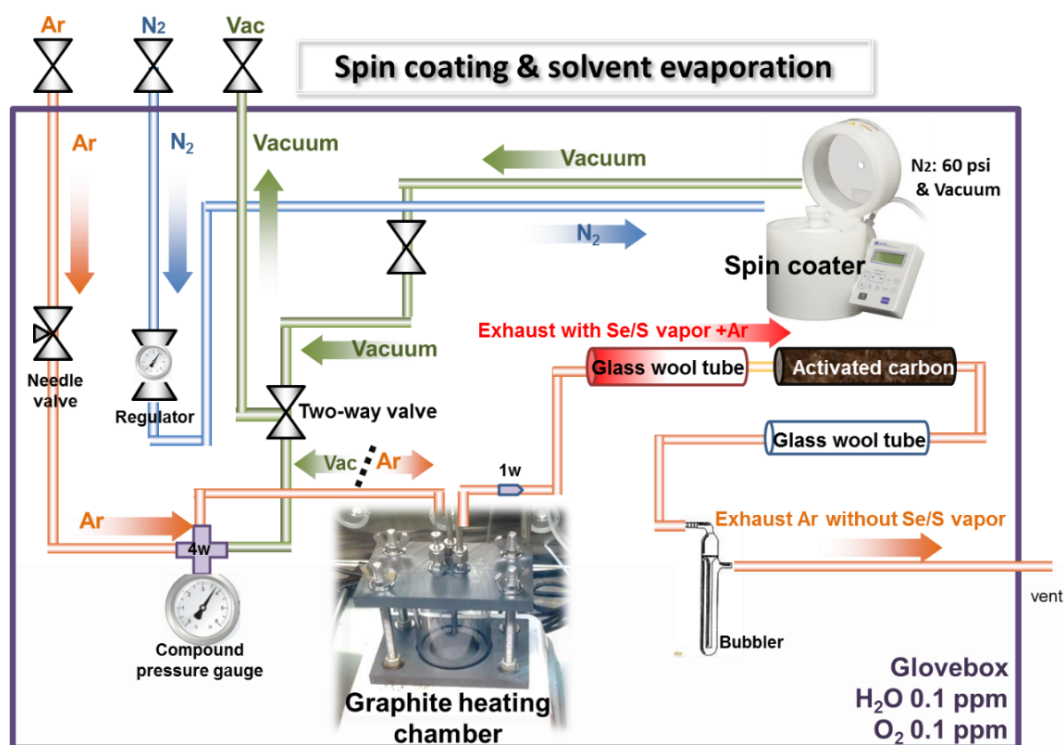


Figure 2.2: A schematic drawing of spin coating and house-made graphite heating chamber in the glovebox. The heating chamber is designed for annealing the as-coated films under Ar/N₂/vacuum condition and preventing the deposition of Se/S inside the glovebox. Note that Se/S vapor is highly toxic to humans.

2.3.3 Selenization

The thin film was finally annealed at 500°C in a selenium atmosphere for 30 mins to achieve a higher crystallinity and promote grain growth. A temperature controlled tube furnace was used for the selenization purpose, as shown in Figure 2.3. The samples and selenium pellets were put into a sealed graphite box (inset in Figure 2.3). The sample box was parked at the cold zone of the quartz tube while the temperature inside the tube furnace was ramping. After the temperature at the center of tube became stable at 500°C, the graphite box was pushed into the center of the tube furnace by

a push-pull rod. The melted selenium pellets created a saturated selenium atmosphere around the samples. The amount of selenium pellets was well-controlled to create a saturated atmosphere. Before pre-heating, the tube furnace also was purged three times using Ar to ensure the purity of the gas atmosphere. After the desired time passed, the furnace was quickly cooled to the room temperature. A constant flow of Ar was applied into the tube in order to facilitate the cooling of the samples.

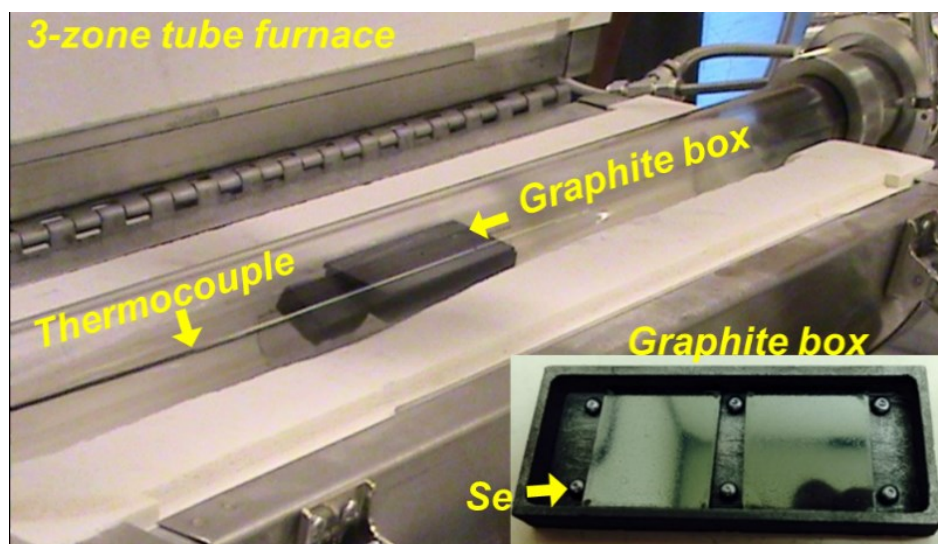


Figure 2.3: Picture of tube furnace for selenization. The inset is the layout of selenium pellets and samples in a graphite box.

2.3.4 Device Fabrication

Solar cells were fabricated from the above-described CZTSSe films by creating the following additional layers: chemical bath deposition of ~50 nm cadmium sulfide (CdS), sputtering of ~80 nm intrinsic zinc oxide (ZnO) and ~220 nm tin-doped indium oxide (ITO). On the top of the device, Ni/Al metal contacts were deposited by electron-beam deposition. For some devices, a ~100 nm antireflective magnesium fluoride (MgF_2) coating was applied on the top to enhance the light absorption. The top-view of a solar cell is shown in Figure 2.4a and the cross-section schematic

drawing is shown in Figure 2.4b. There are six cells with a total area of 0.47 cm^2 on a one-by-one inch substrates. The active area of the solar cells is normally $\sim 0.45\text{-}0.46 \text{ cm}^2$.

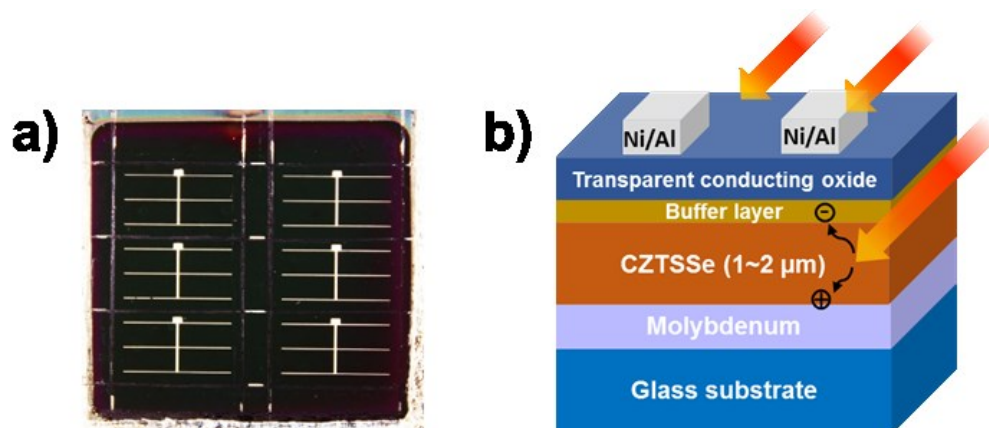


Figure 2.4: a) Top-view image of the fabricated solar cell. There are six cells on a one-by-one inch substrate. b) The schematic drawing of the solar cell cross-section.

2.3.5 Characterization

The material phases, film morphology, and compositions were characterized using X-ray diffraction (XRD) (Rigaku), Raman spectroscopy with an excitation wavelength of 633 nm (HORIBA HR800 system), and scanning electron microscopy (SEM) equipped with energy X-ray dispersive spectroscopy (EDX) (FEI Quanta) equipped with an Oxford EDX silicon drift detector (SDD, X-MaxN 80 mm²).

The J-V characteristics were measured with a four-point probe station using a Keithley 2400 series sourcemeter and a Newport Oriel simulator with AM 1.5 illumination. The solar simulator was calibrated to 100 mW/cm^2 using a Si reference cell certified by NIST. External quantum efficiency (EQE) was studied under 0 V and -1 V bias in order to gain more insight into the solar cell performance.

A linear superposition of Gaussian and Lorentzian distributions is used to fit the Raman spectra in this study. Equation 2.1 shows the fitting function used in Labspec software.

$$\begin{aligned}
 I_G(x) &= \frac{A}{\omega} \sqrt{\frac{4 \ln(2)}{\pi}} \exp\left(-4 \ln(2) \frac{(x-x_c)^2}{\omega^2}\right) \\
 I_L(x) &= \frac{2A}{\pi} \frac{\omega}{4(x-x_c)^2 + \omega^2} \\
 I(x) &= gI_G(x) + (1-g)I_L(x)
 \end{aligned}
 \tag{Equation 2.1}$$

where A is the peak amplitude, ω is the peak FWHM, x_c is the location of the peak maximum, and g is the weighting factor for the Gaussian contribution.

2.4 Results and Discussion

2.4.1 CZTSSe Molecular Precursor Solutions

In the particular experiment for high-efficiency solar cell fabrication, *Solution A* was prepared by dissolving CuCl, ZnCl₂, and SnCl₂ into a mixture of hexylamine and propanethiol (volume ratio 4:1). After stirring the solution at room temperature for 2 hrs, the metal chloride salts were fully dissolved. *Solution B* was prepared by dissolving Se powders and S flakes into a combination of hexylamine and propanethiol (volume ratio 2:1). In *Solution B*, the total concentration of chalcogens [S+Se] was 2 M, and the ratios of [S]:[Se] were adjusted to modify the grain growth during selenization and the band gap of the resulting absorber film. For typical devices reported here, the concentration ratio of [S]:[Se] was equal to 4:1. The *CZTSSe precursor solution* was prepared by mixing *Solution A* with *Solution B* in a volume ratio of 5:1. After complete mixing, the solutions are transparent orange; and the color varied slightly with concentration ratio of [S]:[Se], as shown in Figure 2.5. All operations were performed at ambient temperature (25°C±2°C) in a N₂ glovebox with < 0.1 ppm water and oxygen.

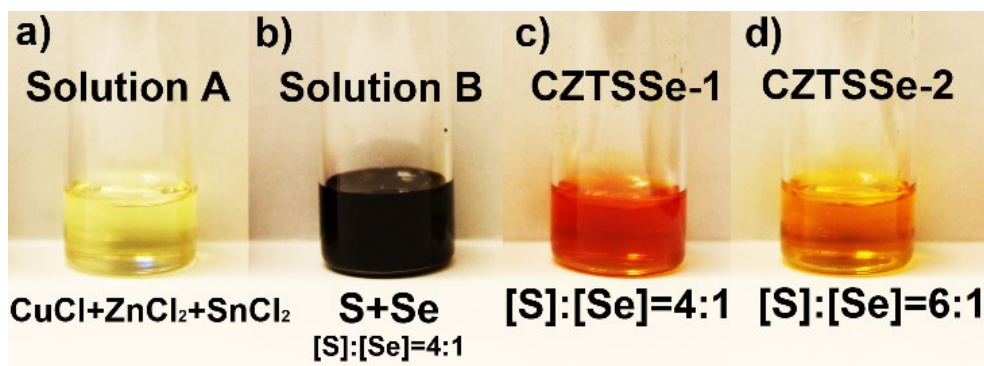


Figure 2.5: Images of molecular precursor solutions prepared using hexylamine-propanethiol solvent mixtures. a) *Solution A*: cation precursor containing CuCl, ZnCl₂, and SnCl₂ with a concentration ratio of [Cu]:[Zn]:[Sn] = 1.53:1.05:1 and [Sn] = 0.1 M in hexylamine and propanethiol (vol. ratio 4:1). b) *Solution B*: chalcogen precursor with a concentration ratio of [S]:[Se] = 4:1 [S]+[Se] = 2 M in hexylamine and propanethiol (vol. ratio 2:1). c) *CZTSSe-1*: mixture of *Solutions A* and *Solution B* (vol. ratio 5:1). d) *CZTSSe-2*: mixture of *Solution A* with another chalcogen precursor with [S]:[Se] = 6:1, shown to illustrate color changes with changing [S]:[Se].

Dynamic light scattering measurement was performed using Zetasizer Nano ZS90 (Malvern, measurement range 0.3 nm-10.0 μ m) on CZTSSe-1 precursor solution in Figure 2.5. The solution was stored in a sealed quartz cuvette for the measurement. No particles were detected, indicating the precursor is a pure solution.

2.4.2 Versatility of Primary Amine-Monothiol Solvent Mixtures

The versatility of the developed primary amine-monothiol solvent mixture is exhibited in two aspects. 1) The primary amine-monothiol solvent mixtures can dissolve a variety of cation sources; 2) The primary amine/s and monothiol/s with different carbon chain lengths can be used for this type of mixture.

The examples shown in Figure 2.6 are solutions prepared by individually dissolving 0.6 mmol of Cu₂O, ZnO, CuCl, CuCl₂, ZnCl₂, Cu(OAc)₂, Cu(acac)₂, Zn(OAc)₂, SnCl₂, and Sn(acac)₂Cl₂ in 2-ml solvent mixtures of hexylamine and propanethiol (a volume ratio of 4:1). The metallic Zn solution is prepared by dissolving 1 mmol of Zn powder in a 2-ml solvent mixture of butylamine

and propanethiol (volume ratio 1:1). The dissolution process was performed at ambient temperature ($25^{\circ}\text{C}\pm 2^{\circ}\text{C}$) in a N_2 glovebox with < 0.1 ppm water and oxygen. All the chemicals were purchased from Sigma Aldrich and used without any further purification.

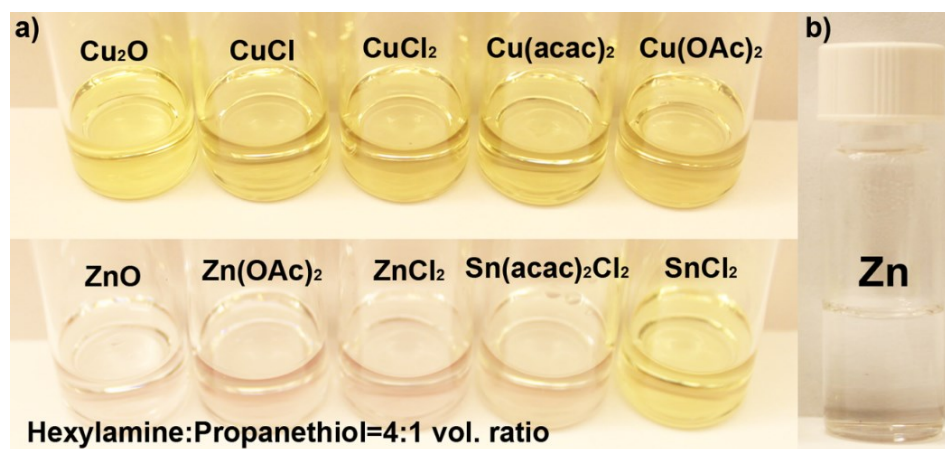

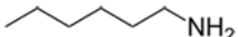

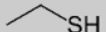




Figure 2.6: a) Solutions of cation oxides and cation salts dissolved in hexylamine and propanethiol with a volume ratio of 4:1. The concentrations of all solutions are 0.3 M. b) Solution of metallic zinc in butylamine and propanethiol with a volume ratio of 1:1. The concentration of zinc solution is 0.5 M.

Table 2.1 shows the combinations of primary amines and monothiols that have been used in the preparation of CZTSSe precursor solutions. Figure 2.7 presents the CZTSSe precursor solutions prepared by using the mixture of oleylamine and ethanethiol and the mixture of butylamine and propanethiol. In general, in the solvent mixture, the longer chain of the primary amine/monothiol is, the longer the dissolution time is at room temperature. Although primary amines and monothiols with different boiling points can be used as the solvents, the use of relative low boiling point amines and thiols ($< 250^{\circ}\text{C}$) is necessary, in order to fabricate carbon-free thin films with no fine grains.

Table 2.1: Combinations of primary amine and monothiol for precursor preparation.

Thiol \ Amine	Butylamine	Hexylamine	Oleylamine
			
Ethanethiol 	√	√	√
Propanethiol 	√	√	-
Butanethiol 	√	√	-

√ : the combination can dissolve CuCl, ZnCl₂, SnCl₂, S, and Se with the solution condition of [Cu]:[Zn]:[Sn]:[S+Se] = 1.53:1.05:1:4 and [Sn]=0.1 M;

- : the combination cannot dissolve CuCl, ZnCl₂, SnCl₂, S, and Se with the solution condition of [Cu]:[Zn]:[Sn]:[S+Se] = 1.53:1.05:1:4 and [Sn]=0.1 M;

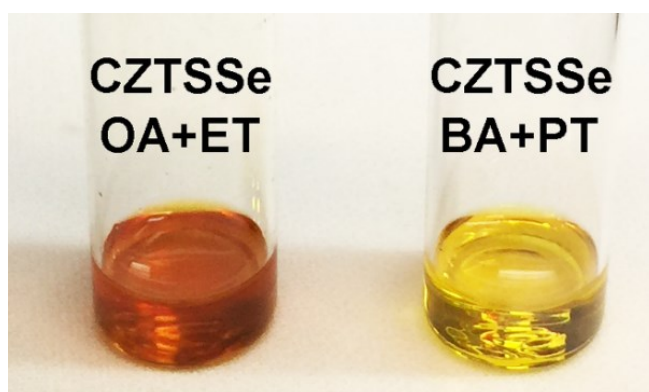


Figure 2.7: CZTSSe precursors prepared using oleylamine (OA) and ethanethiol (ET) (vol. ratio 1:1) (left) and butylamine (BA) and propanethiol (PT) (vol. ratio 1:1) (right). In the above CZTSSe precursors, [Cu]:[Zn]:[Sn]:[S+Se] = 1.53:1.05:1:4 and [Sn]=0.1 M.

2.4.3 CZTSSe Solar Cells Processed from Butylamine-Propanethiol Based Precursor Solutions

CZTSSe molecular precursors were prepared as described in section 2.3.1 by mixing *Solution A* containing CuCl, ZnCl₂, and SnCl₂, with *Solution B* containing S, and Se dissolved in butylamine and propanethiol (volume ratio 1:1). Three precursor recipes employed were shown in Table 2.2. Figure 2.8a shows XRD patterns of the as-deposited and annealed precursor films which were prepared using *Recipe 1* precursor solution. The room-temperature dried precursor film only shows four sharp peaks at low angles in XRD pattern, which do not match with any phases found in JCPDS inorganic material database. Single-crystal XRD analysis with assistance of solution chemistry analysis need to be used to identify the structure of the long-range order. Precursor films annealed at 220°C, 270°C, and 300°C show diffraction at 26.5°, 28.0° and 30.0° corresponding to (010), (002) and (011) planes of wurtzite CZTS. The size of CZTSSe nanoparticles formed at 220°C is 10-20 nm based on Scherrer equation. Figure 2.8b illustrates the Raman spectrum collected from the precursor film annealed at 220°C. The peak at 336 cm⁻¹ corresponds to wurtzite CZTS, while another peak at 225 cm⁻¹ belongs to CZTSe.⁵⁶ The shift of the A1 mode for CZTS and CZTSe was observed due to the coexistence of S and Se in the crystal lattice.^{45,50,56} XRD patterns in Figure 2.8a and c reveal that the precursor films prepared using all three recipes were converted into kesterite CZTSe large-grained films after selenization at 500°C for 20 min. No secondary phases have been detected.

The morphologies of a precursor film and a selenized film prepared using *Recipe 1* are shown in Figure 2.9. The cracks formed on the precursor film are attributed to the solvent evaporation during the annealing process. After selenization, a film composed of faceted grains with 0.5-1 μm diameters was obtained, indicating the grain growth occurred simultaneously with the phase transformation. The precursor film thickness was optimized by varying the total number of coatings. The solar cell efficiencies achieved from different precursor film thicknesses are summarized in Figure 2.10. It shows that a 4-layer coating results in much higher efficiencies than a 6-layer coating

followed by an 8-layer coating. After selenization, a film around 1 μm thick was obtained from the 4-layer precursor film. This selenized film consists of a large-grained layer with a thickness of 720 nm and a small-grained layer of 380 nm, shown in Figure 2.11a. The 6-layer precursor film resulted in an increased total film thickness compared to the case of 4-layer precursor film after selenization in the same condition. Unfortunately, the thickness of large-grained layer decreased, while the thickness of small-grained layer increased to $>1 \mu\text{m}$ (Figure 2.11b). The recombination of electrons and holes in the small-grained layer is higher than that of the large-grained layer due to the increased number of grain boundaries. Therefore, the continual increase in precursor film thickness did not benefit the solar cell efficiencies, and the carrier collection became worse when the total film thickness was beyond $\sim 1 \mu\text{m}$.

Table 2.2: Recipes of CZTSSe precursors based on butylamine-propanethiol solvent mixture.

Precursor recipe	[Cu]/[Sn]	[Cu]:[Zn]:[Sn]:[S]+[Se]
R1	1.45	1.45:1.05:1:4
R2	1.76	1.76:1.05:1:4
R3	2	2:1.05:1:4

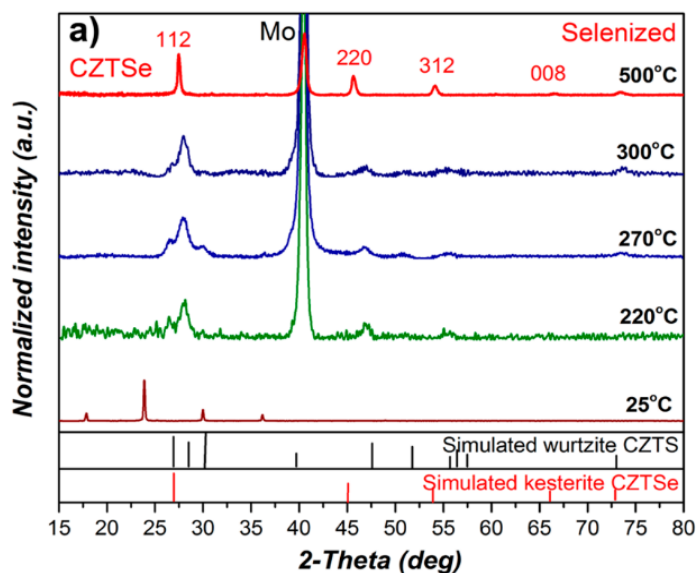


Figure 2.8: a) XRD patterns for CZTSSe precursor films annealed at different temperatures. The precursor films were prepared using *Recipe 1* in Table 2.2. Note that the final annealing was performed under selenium atmosphere at 500°C for 20 min.

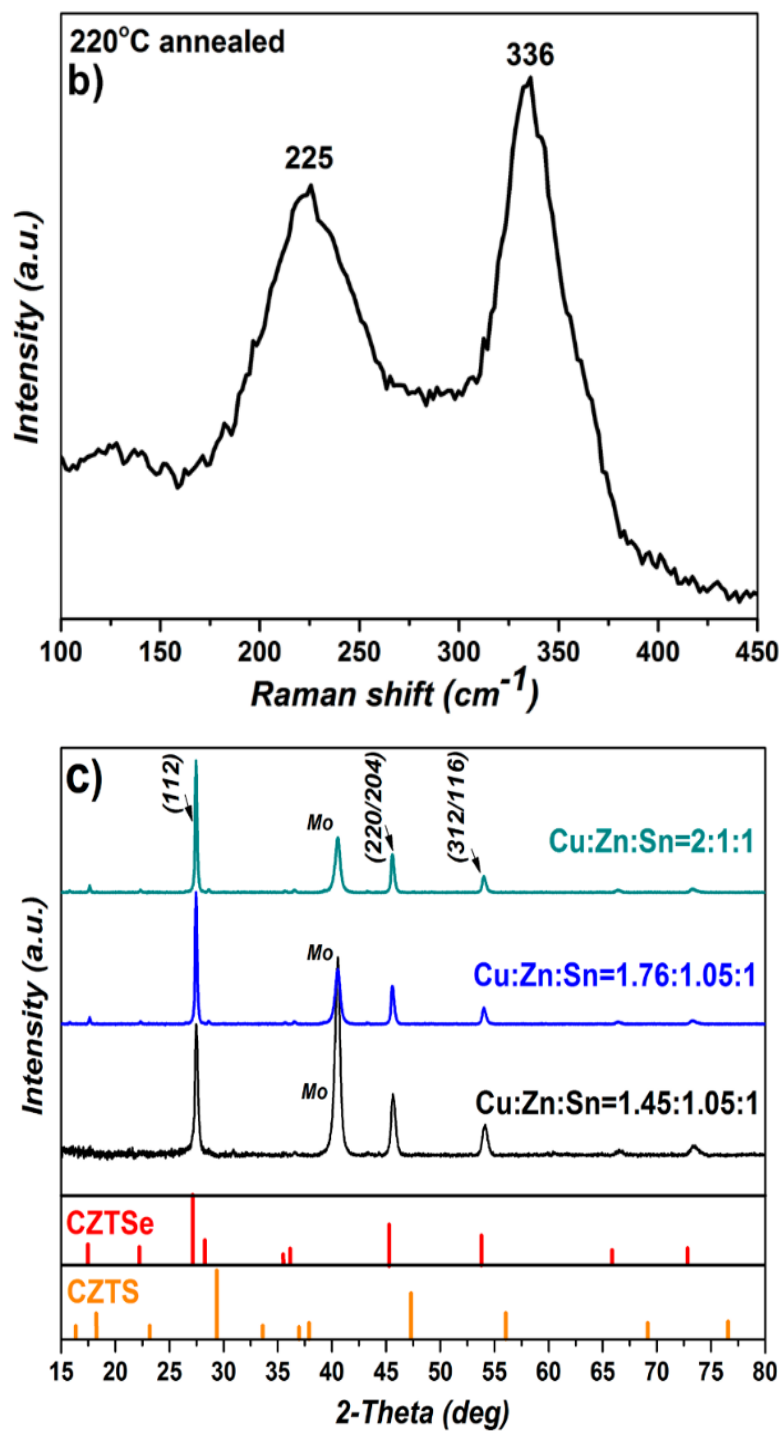


Figure 2.8: (Continued) b) Raman spectrum of the CZTSSe precursor film annealed at 220°C for 5 min. c) XRD patterns for the selenized films prepared using three recipes in Table 2.2.

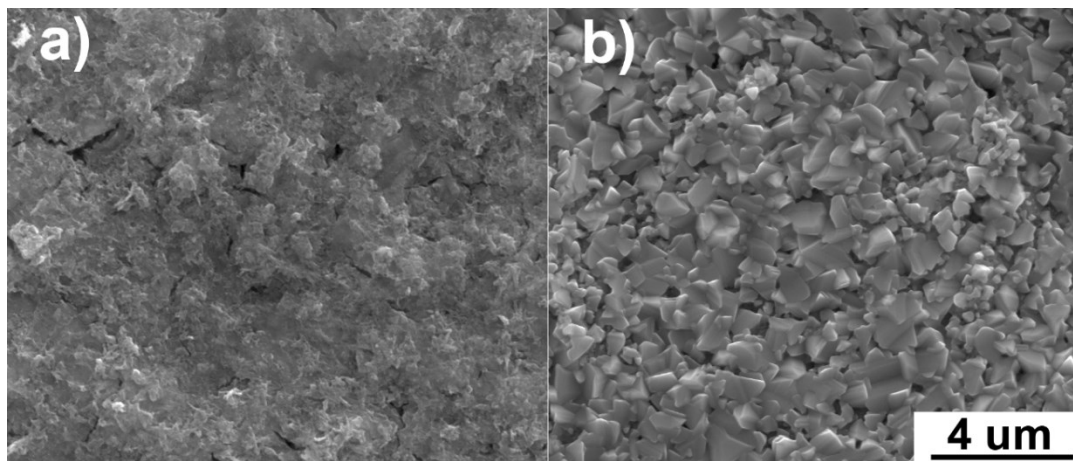


Figure 2.9: Top-view SEM images of a) a precursor film prepared using *Recipe 1* in Table 2.2, and b) film morphology after selenization.

The solar cell efficiencies and key parameters of solar cells processed using different recipes are summarized in Figure 2.10 and Table 2.3. Comparing the solar cells processed from the 4-layer precursor films, it can be found that *Recipe 1* results in the highest efficiency, followed by *Recipe 2*, and then *Recipe 3*. So far, the highest PCE achieved using a solvent mixture of butyalmine-propanethiol based CZTSSe molecular precursor is 3.66%. The J-V curve under AM 1.5 illumination is shown in Figure 2.12. Note that the V_{oc} of all devices (≤ 320 mV) is much lower than the V_{oc} (370 mV $\leq V_{oc} \leq 430$ mV) of CZTSSe thin film solar cells prepared using nanoparticle inks.^{3,34} The phase transformation from wurtzite to kesterite of CZTSSe during the selenization process may lead to the lower V_{oc} observed. In particular, pinholes generated during the wurtzite-kesterite phase transformation lead to a significant decrease in the shunt resistance, J_{sc} , and FF as reported in the study of Yang et al.³⁷

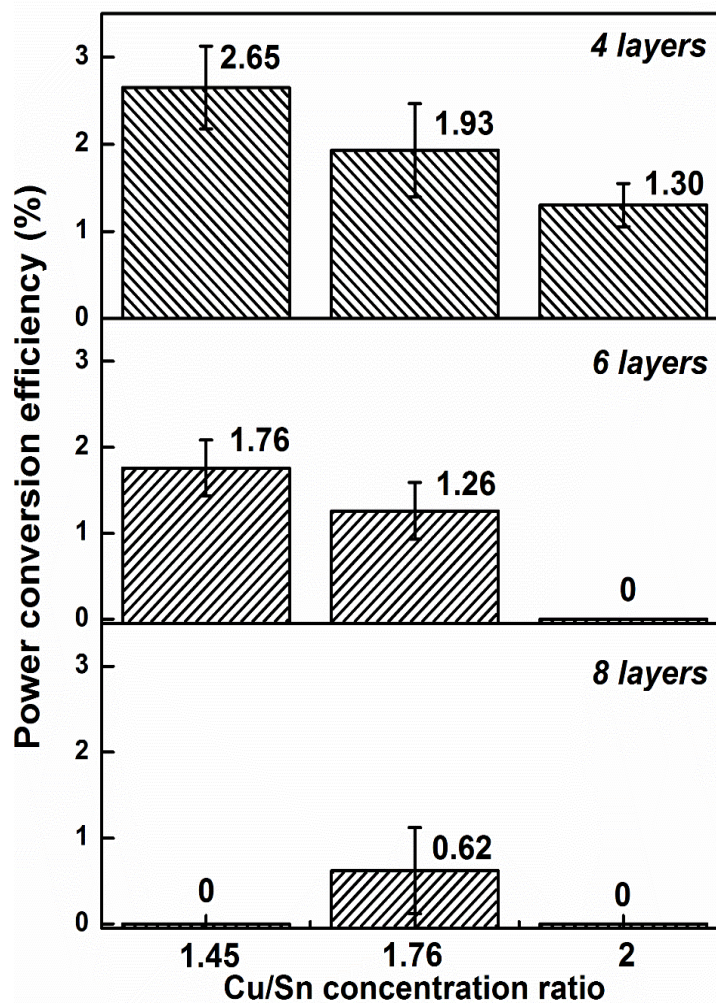


Figure 2.10: Statistics of solar cell PCEs prepared using different precursor film thicknesses and recipes shown in Table 2.2.

Table 2.3: Highest solar cell PCEs obtained from three recipes.

Solution recipe	V_{oc}	J_{sc}	FF	PCE
Cu:Zn:Sn:S+Se	(mV)	(mA/cm ²)	(%)	(%)
R1 1.45:1.05:1:4	320	30.5	37.8	3.66
R2 1.76:1.05:1:4	270	26.1	43.8	3.04
R3 2:1:1:4	190	30.3	33.6	1.80

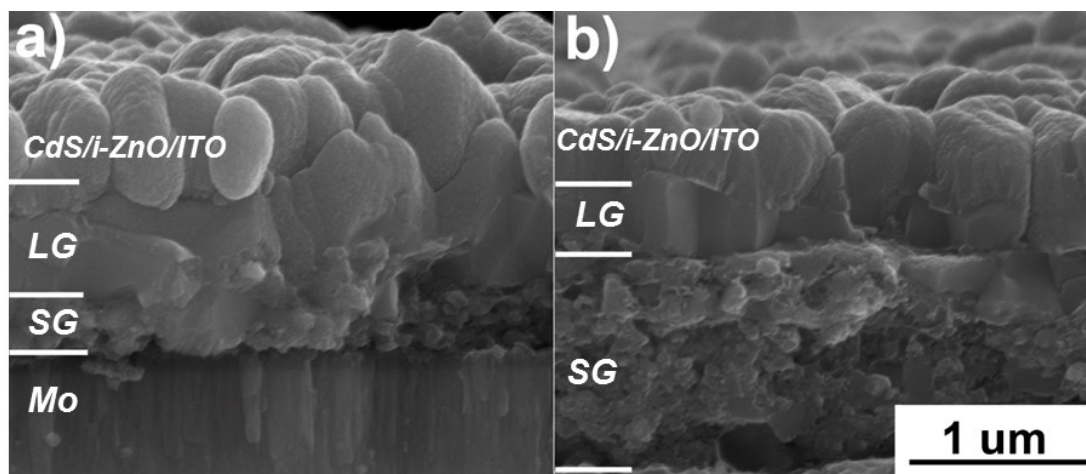


Figure 2.11: Cross-sectional SEM images of device processed using *Recipe 1* precursor. a) 4-layer precursor film after selenization. The average total thickness is 1.1 μm . The thickness of the large grain layer (LG) is ~ 720 nm while that of the small grain layer (SG) is ~ 380 nm; b) 6-layer precursor film after selenization. The average total thickness is 1.50 μm . The thickness of LG is ~ 330 nm while that of SG is ~ 1.2 μm .

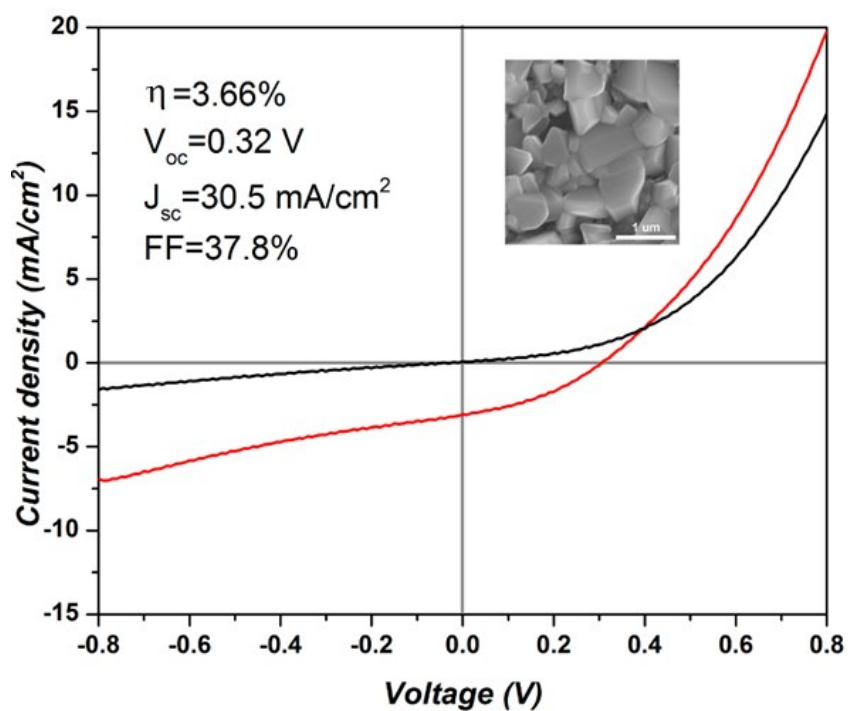


Figure 2.12: J-V curves of a CZTSSe device fabricated using precursor *Recipe 1* in Table 2.2. The inset is a top-view SEM image of the selenized film.

2.4.4 CZTSSe Solar Cells Processed from Hexylamine-Propanethiol Based Precursor Solutions

The hexylamine-propanethiol based precursor is prepared following the procedures described in section 2.4.1. After eight-spin coating step, a CZTSSe precursor film with a thickness of 800 nm to 1 μm was fabricated. The film shows good optical reflectivity after the solvent evaporation process, indicating a low film porosity (Figure 2.13). The top-view SEM image (Figure 2.14a) confirms that this film is smooth and continuous despite a few shallow cracks. EDX linescans were employed to measure the composition fluctuation at microscale within the CZTSSe precursor film. Figure 2.15 shows the elemental distributions of Cu, Zn, Sn, S, and Se across $>10 \mu\text{m}$ on the top surface. In comparison to the hydrazine slurry-processed CZTSSe precursor film, a more uniform elemental distribution is obtained using this molecular solution method.⁴⁰ Figure 2.14b is a typical cross-sectional SEM image of an 8-layer precursor film. It shows a uniform film structure throughout the film thickness.

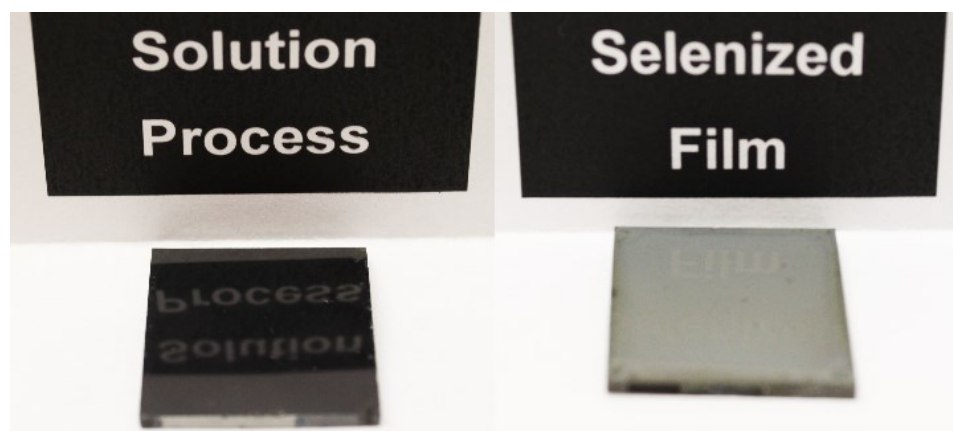


Figure 2.13: Images of a precursor film and the selenized film on a Mo-sputtered soda-lime glass substrate.

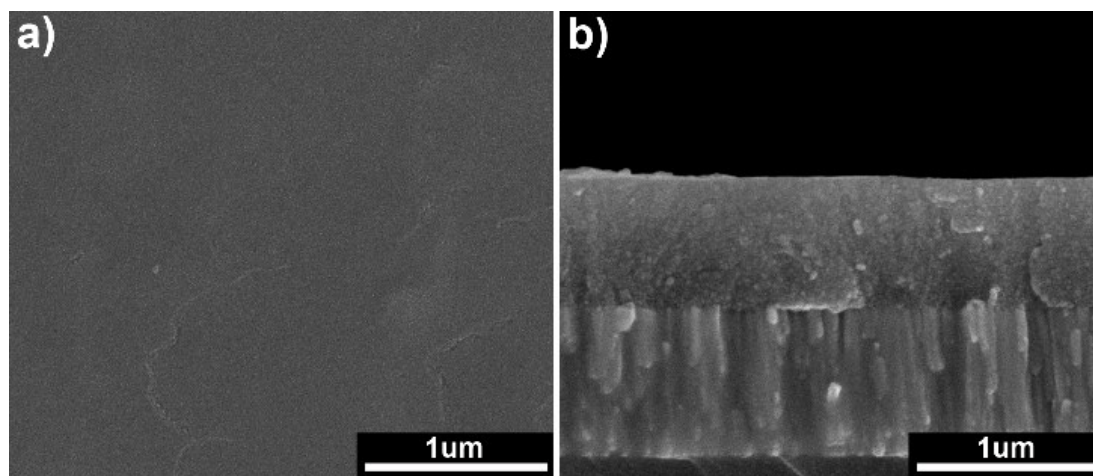


Figure 2.14: a) Top-view SEM image of the precursor film fabricated by spin-coating and subsequent annealing, and b) Cross-sectional SEM image of the precursor film.

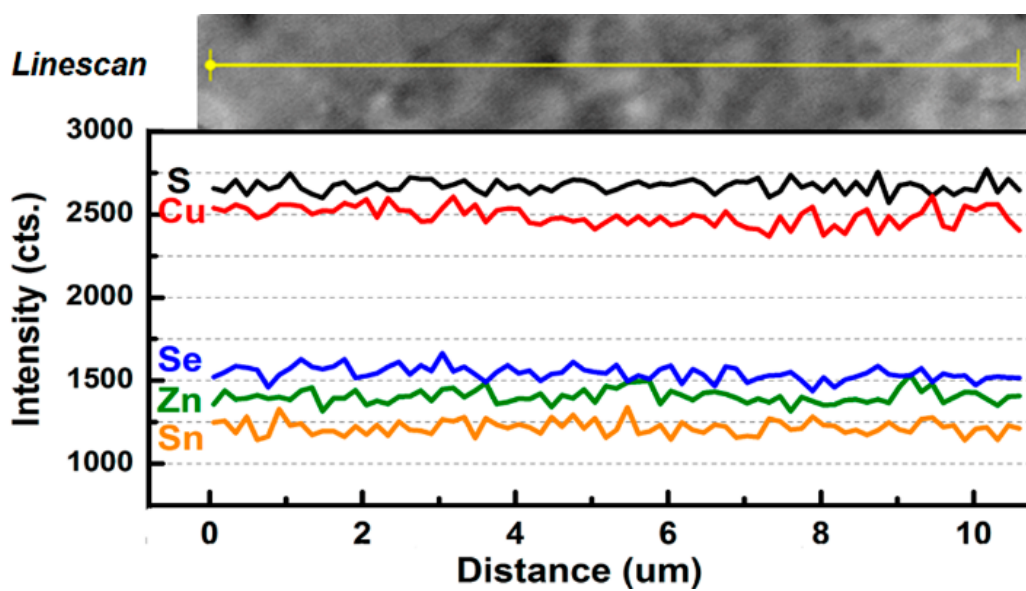


Figure 2.15: EDX linescan along precursor film surface (>10 μm scan) showing compositional uniformity.

Grazing incident XRD was employed to measure the nucleated phase after low-temperature annealing at 250°C. As shown in Figure 2.16, all the XRD peaks are consistent with the kesterite CZTS standard with a very slight shift to lower angles, indicating the substitution of some Se atoms

at S positions. In order to get more insight into the phases present in the precursor film, Raman spectra were obtained with an excitation laser wavelength of 632.8 nm. In Figure 2.17a, the peaks at 334 cm^{-1} , and 364 cm^{-1} correspond to kesterite CZTS, while peaks at 223 cm^{-1} , 238 cm^{-1} , and 297 cm^{-1} correspond to sulfoselenide which contains both S and Se at the anion sites in the crystal lattice. The peak position and the details of peak fitting are shown in Figure 2.17b. This bimodal behavior in the Raman spectra has been previously reported for samples with intermediate values of $[S]/([S]+[Se])$, with similar peak broadening and position shifts as we report here.^{45,50,56}

In summary, four objectives have been achieved using this newly developed CZTSSe molecular precursor: (1) four to five cations/anions were dissolved at significant concentrations to obtain the above molecular precursor; (2) the precursor solution remained stable, allowing the deposition of compositionally homogeneous precursor films; (3) the choice of the specific amine-thiol mixture and subsequent drying process enabled the formation of continuous and smooth precursor films; (4) the kesterite CZTSSe phase was obtained after the solvent evaporation process.

Based on the SEM-EDX analysis (see Table 2.4), the film contains copper, zinc, tin, sulfur, selenium, and trace chloride. The concentration of chloride ions dropped to a very low level in the as-annealed precursor film. It has been demonstrated that a higher temperature annealing (e.g. $\geq 300^\circ\text{C}$) can decrease the concentration of chloride in the precursor film below the detection limit of EDX. The chlorine ions may leave the film in various forms, such as chlorine gas, Se_2Cl_2 (boiling point at 127°C) and/or SeCl_4 (sublimes at 191.4°C). The disassociation mechanism of the chloride ions deserves further study. After the film deposition and solvent evaporation/annealing steps, the films contain a combination of CZTSSe nanoparticles and amorphous phases, which has been confirmed by the characterization on precursor film deposited on Si_3N_4 grid using HRTEM.

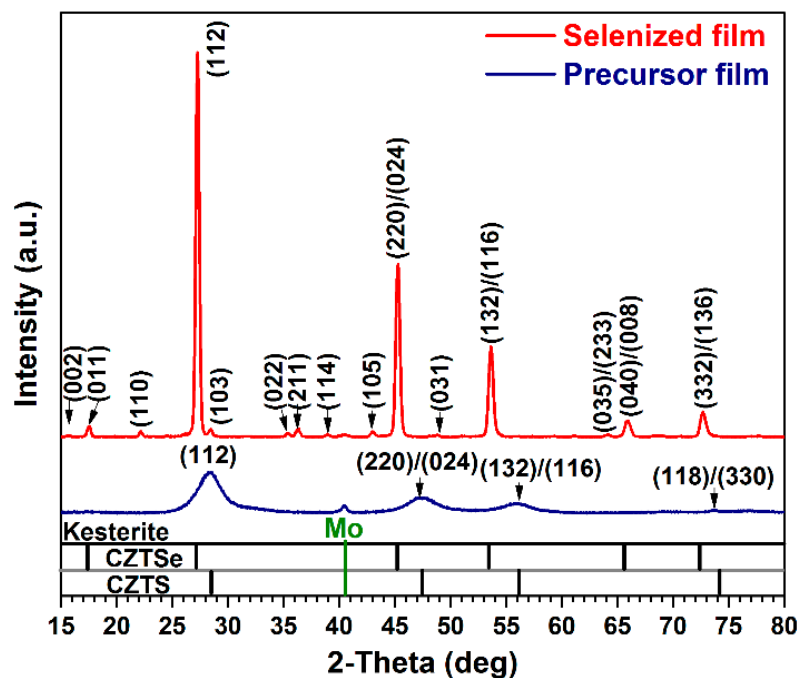


Figure 2.16: XRD patterns of the precursor film and the selenized film. The standards of kesterite CZTSe (space group: $I\bar{4}$, JCPDS 01-070-8930) and CZTS (space group: $I\bar{4}$, simulated pattern based on JCPDS 01-75-4122) are marked at the bottom of the plot.

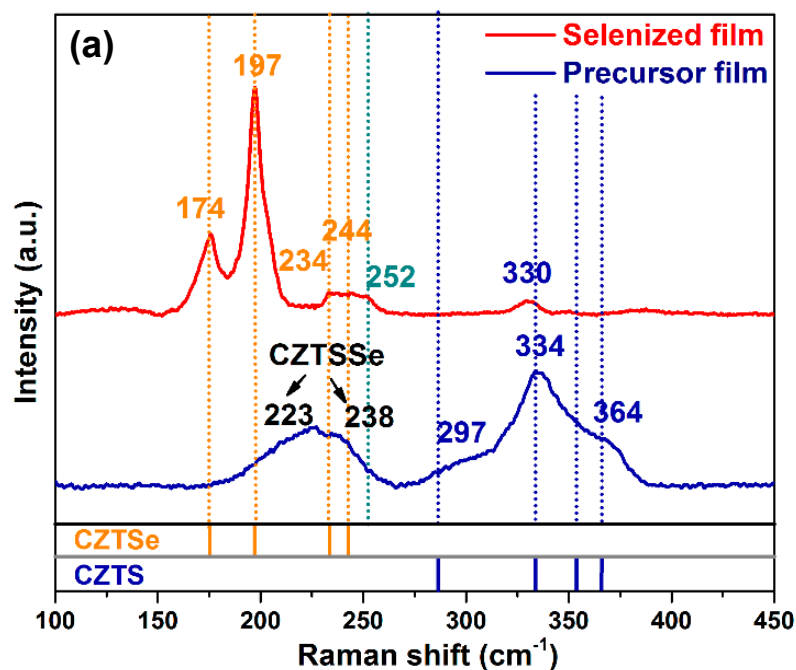


Figure 2.17: a) Raman spectra of the precursor film and the selenized film. The Raman standards for CZTS and CZTSe are labeled at the bottom.^{2,56-58}

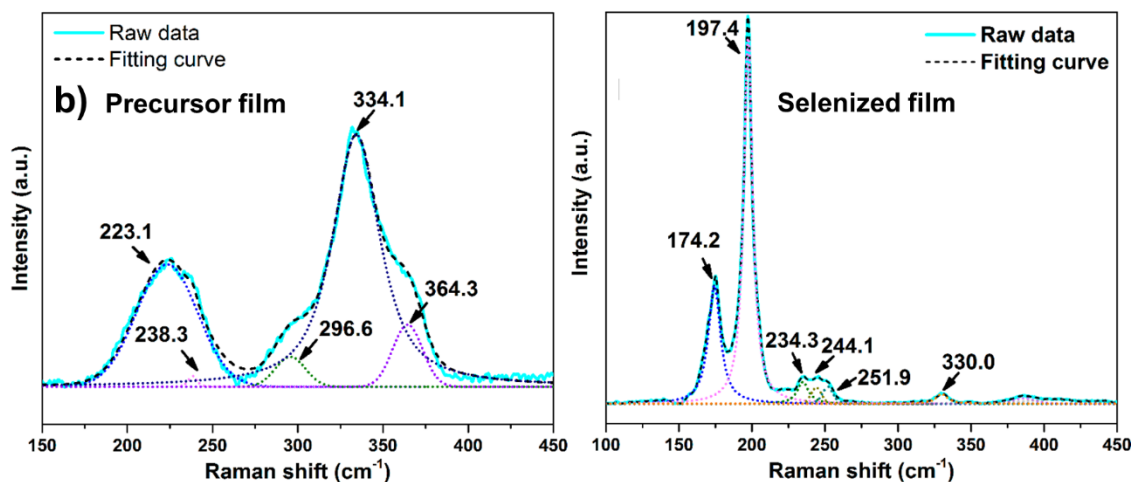


Figure 2.17: (Continued) Fitted curves of Raman spectra in a).

The selenization was performed at 500°C for 30 min under saturated selenium atmosphere in a tube furnace with a constant Ar flow at 10 sccm. After selenization, the film converted into a high-crystallinity CZTSSe thin film, as shown in Figure 2.18. The top-view SEM image in Figure 2.18 shows a typical microstructure, which consists of a high-density film with a rough, highly faceted surface, and an average in-plane grain size of approximately 600 nm. The fractured cross-section of a full device in Figure 2.18b shows that the fine-grained layer near the molybdenum substrate is much thinner (< 150 nm) compared to those created by other direct solution methods.^{43,50,52}

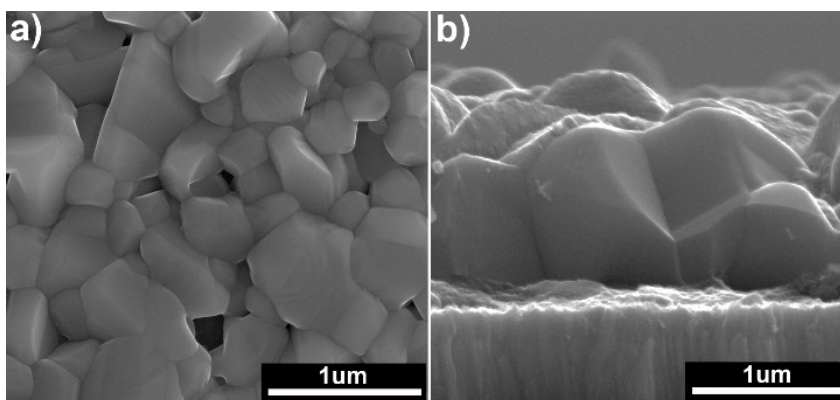


Figure 2.18: a) Top-view SEM image of large-grain selenized film, and b) fractured cross-section of the CZTSSe device prepared following procedures described in Section 2.3.4.

The XRD pattern in Figure 2.16 indicates the formation of a high-crystallinity kesterite CZTSSe film, with a small amount of S substituting for Se. In the corresponding Raman spectrum (Figure 2.17), peaks at 174 cm^{-1} , 197 cm^{-1} (A1 mode), 234 cm^{-1} , and 244 cm^{-1} refer to kesterite CZTSe, while the peak at 330 cm^{-1} refers to kesterite CZTS. Although the peak at 252 cm^{-1} might indicate the presence of ZnSe in the selenized film, the ZnSe phase should not contribute to the spectra under a 633 nm laser excitation.^{57,58} Since XRD and Raman spectroscopy with 633 nm laser excitation cannot totally rule out the existence of secondary phases (e.g. ZnS/ZnSe), other characterization techniques are required for more accurate phase identification (e.g. Raman spectroscopy with 325 nm laser excitation).

Focused ion beam milling (FIB) was used to prepare a cross-section of a CZTSSe solar cell and then SEM-EDX mapping was performed on this cross-section. The compositional uniformity of Cu, Zn, Sn, S, and Se in the absorber thin film is confirmed by the elemental mapping in Figure 2.19. A SEM-EDX linescan (Figure 2.20) on the fractured cross-section also indicates no phase separation can be observed in CZTSSe film. As shown in Table 2.4, the composition of the selenized film is $\text{Cu}_{1.73\pm 0.01}\text{Zn}_{1.07\pm 0.01}\text{Sn}_1(\text{S},\text{Se})_{4.43\pm 0.02}$, and the concentration ratio of $[\text{S}]/([\text{S}]+[\text{Se}])=0.08$.

Table 2.4 Compositions of precursor film and selenized film.

Atomic ratio	Solution	Precursor	Selenized
[Cu]/[Sn]	1.53	1.62 ± 0.02	1.73 ± 0.01
[Zn]/[Sn]	1.05	1.06 ± 0.02	1.07 ± 0.01
[S]+[Se]/[Sn]	4	4.27 ± 0.01	4.43 ± 0.02
[Cl]/[Sn]	5.63	0.3 ± 0.01	-

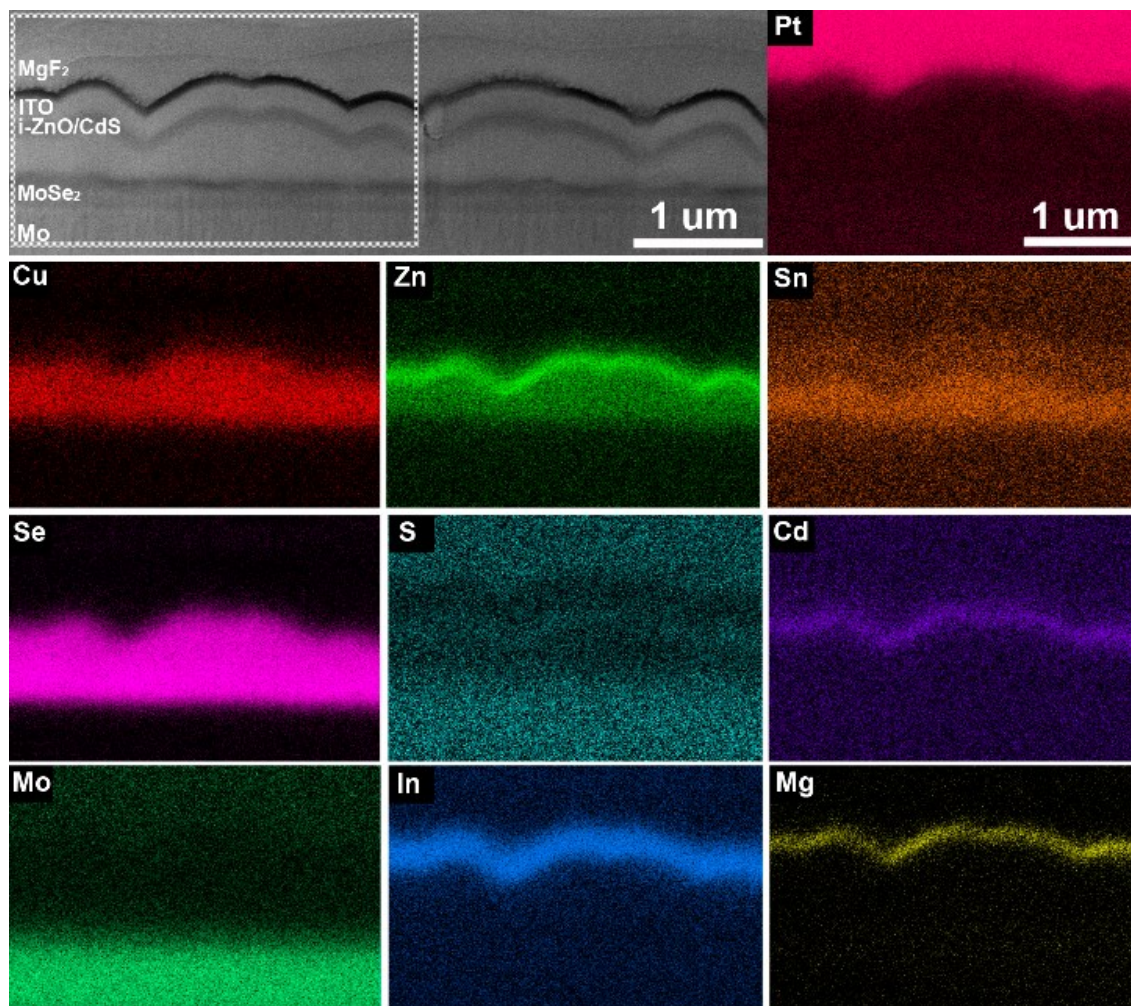


Figure 2.19: EDX mapping of the CZTSSe device. A platinum coating was employed to protect the film during the preparation of FIB-cross section.

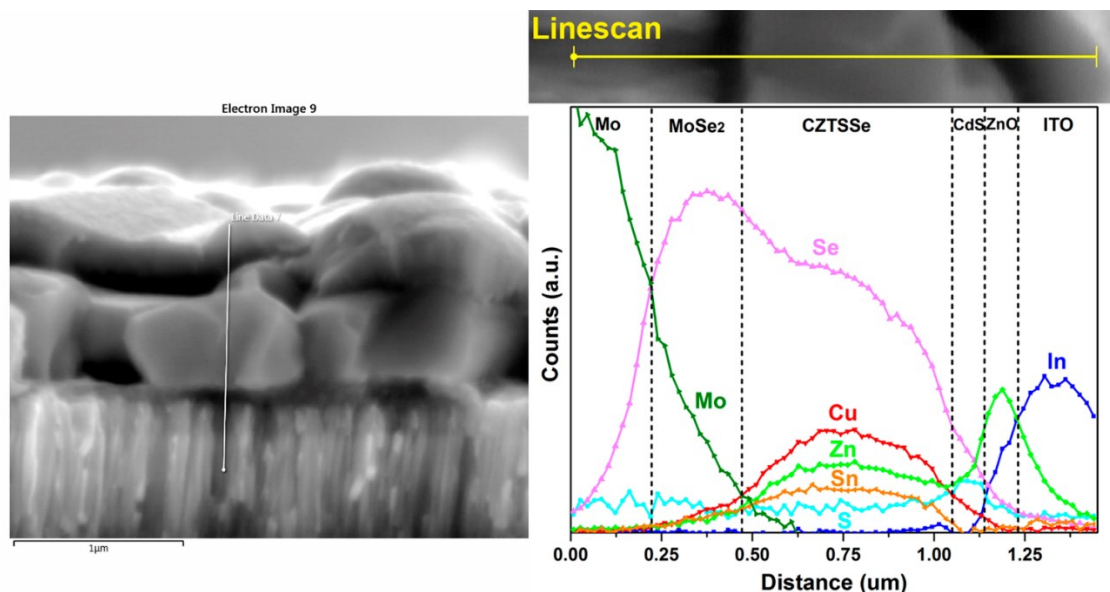


Figure 2.20: SEM-EDX linescan on a fractured cross-section of CTZSSe thin film solar cell. The accelerating voltage of electron beam is 10 kV.

The photovoltaic performance of the solar cells prepared using the aforementioned precursor route was measured under standard AM1.5 illumination. Figure 2.21 shows the current density-voltage (J-V) curves based on a total cell area of 0.47 cm². The solar cell has a total area power conversion efficiency of 7.86 % (8.09% for an active area of 0.456 cm²) with V_{oc} =382 mV, J_{sc} =34.4 mA/cm², and fill factor=60.1%. For further insight into device performance, external quantum efficiency (EQE) response was measured at 0 V and -1 V (Figure 2.22). For both measurements, the EQE is >95% in the visible range and gradually decays in the longer wavelengths. The collection efficiency at the longer wavelength range is more likely limited by the low carrier lifetime, which is confirmed by the measurement of EQE (-1 V)/EQE (0 V) ratio. The linear increase of EQE (-1 V)/EQE (0 V) ratio at longer wavelength indicates that when the depletion width is increased, the collection efficiency is increased. The low lifetime could be a result of a high defect density in the bulk material.^{18,59-62} The bandgap of the CZTSSe film is estimated based on the plot of $[\ln(1-EQE)]^2$ versus the photon energy, as well as the inflection of the EQE curve

(i.e. the peak of the $dEQE/dE$ curve, where $E=hc/\lambda$) (inset in Figure 2.22). The two estimation methods result in the same bandgap value of 1.08 eV. This low bandgap value should be attributed to a high Se concentration in lattice after selenization, which is shown in the film composition in Table 2.4.

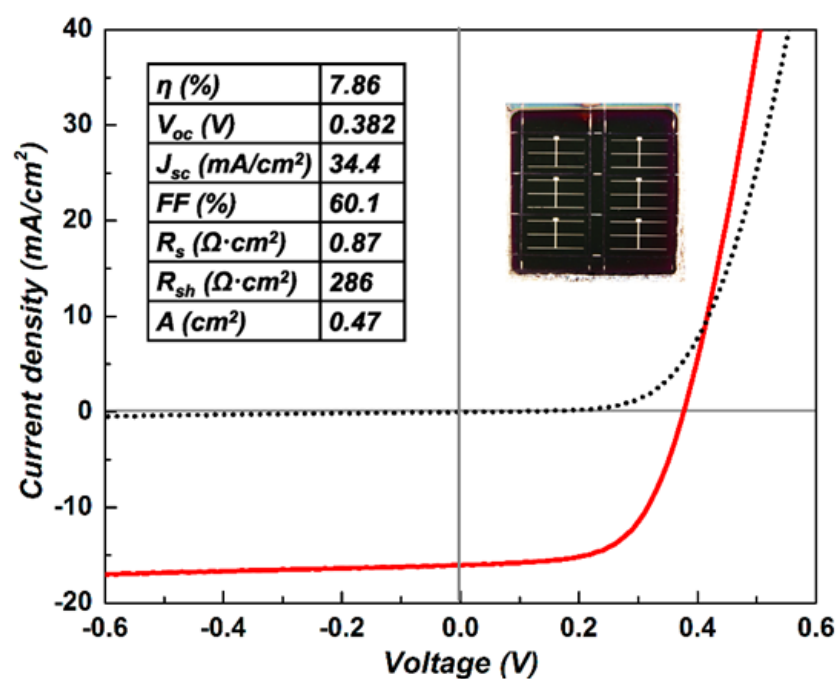


Figure 2.21: J–V curves and performance parameters for the best performing cell in the dark and under AM1.5 illumination. The dotted line shows the dark current density, while the solid line represents the light current density. The series resistance and shunt resistance under light are listed. The inset is the final device.

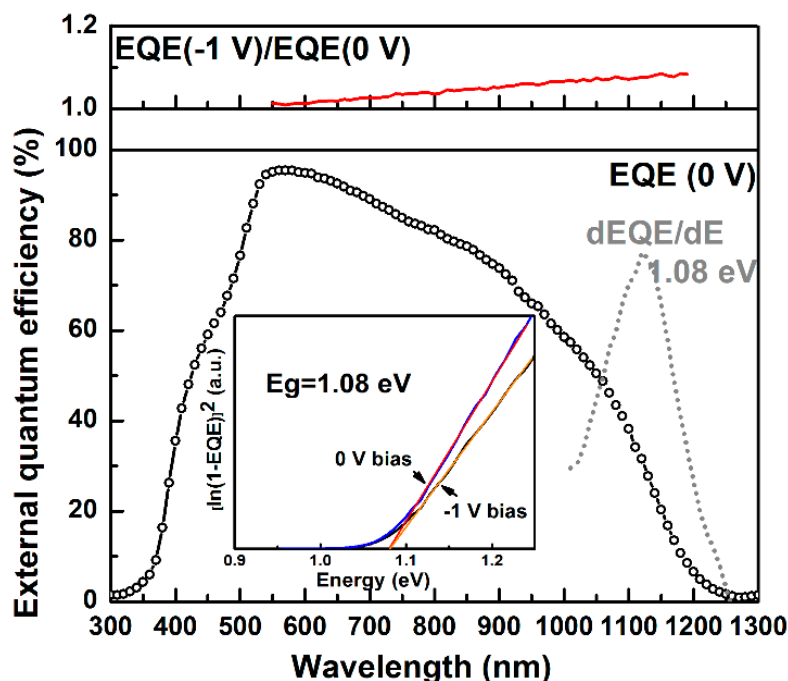


Figure 2.22: EQE measurement of 7.86% device under 0 V and -1 V bias. The inset shows the band gap estimated using $[\ln(1-EQE)]^2$ versus the photon energy as well as the inflection of the EQE curve. The estimated band gap is 1.08 eV.

2.4.5 Optimization of Cu Concentrations

It has been well-known that the concentration of copper ions relative to other cations is critical to bulk defect densities (e.g., $[2Cu_{Sn} + Sn_{Zn}]$ and $[V_{Cu} + Zn_{Cu}]$) and the propensity for secondary phase formation in CZTSSe.^{2,21-23} This section reviews the film quality and solar cell performances processed from precursor solutions with different $[Cu]/[Sn]$ ratios.

Table 2.5 shows the four recipes with different ratios of $[Cu]/[Sn]$ ranging from 1.45 to 1.74. Figure 2.23 and Figure 2.24 show the GIXRD patterns and Raman spectra of the precursor films and the corresponding selenized films, respectively.

Table 2.5: Recipes of CZTSSe precursor solutions with different [Cu]/[Sn] ratios.

Precursor recipe	[Cu]:[Sn]	[Cu]+[Zn]:[Sn]	[Cu]:[Zn]:[Sn]:[S]+[Se]
R1	1.45	0.7	1.45:1.05:1:4
R2	1.53	0.75	1.53:1.05:1:4
R3	1.64	0.8	1.64:1.05:1:4
R4	1.74	0.85	1.75:1.05:1:4

For the precursor films processed using four different [Cu]/[Sn] ratios, a kesterite CZTS phase (with some replacement of Se at S sites) was detected using both XRD and Raman techniques. Based on the XRD patterns (Figure 2.23a), there was no CuS, Cu_{2-x}S, wurtzite ZnS, SnS, Sn₂S₃, or SnS₂. The first three high-intensity peaks of zinc-blend ZnS may overlap with the peaks of kesterite CZTS phase due to the peak broadening effect of low-crystalline films. However, peaks at 33.5° and 77.8° are not present in XRD patterns, revealing that the possibility of its existence is low. For cubic Cu₂SnS₃, since most of its peaks overlap with kesterite CZTS, it is difficult to distinguish them only based on XRD. But it should be pointed out that the distinguishable peak at 32.9° from Cu₂SnS₃ was not observed for any [Cu]/[Sn] ratio. Although Raman spectra (Figure 2.23b) show slight changes in relative peak intensities and fitting peak positions in sulfoselenide peaks between 200 cm⁻¹ and 250 cm⁻¹ as Cu concentration increases, there is no clear trend observed. It is well-known that the typical Raman spectra for CZTS are 288±2 cm⁻¹, 338±1 cm⁻¹, and 368±2 cm⁻¹. However, the peak at ~297 cm⁻¹ shows up for all recipes under Raman measurement. The peak at ~297 cm⁻¹ also has been reported in the study of Mitzi et al., in which a pure CZTS thin film was prepared using a hydrazine-based precursor.⁴⁵ There are three hypotheses about this peak. Firstly, this peak may correspond to some metal complexes with metal-sulfur bonds. Secondly, Since there is ~20% Se existing in the precursor film, a shift in the characteristic peaks of CZTS may occur according to some reports about Raman study of Cu₂ZnSn(Se_xS_{1-x})₄. In the study of Grossberg et al., Raman spectra of Cu₂ZnSn(Se_xS_{1-x})₄ thin films with varied x values are plotted. For example, the A1-mode peak (338 cm⁻¹) shifts to the left when x increases from 0 to 0.26 and the A1-mode

peak also starts to broaden.⁵⁶ Therefore, the peak at $\sim 297\text{ cm}^{-1}$ might show up due to the shift and broadening effect in the sulfoselenide thin films. Third, in the studies of Miskin et al. and Yang et al., the CZTS nanoparticles synthesized have a Raman peak between 288 cm^{-1} and 303 cm^{-1} . Their explanation is that both kesterite CZTS and tetragonal/cubic Cu_2SnS_3 (CTS) may contribute to this peak at $\sim 297\text{ cm}^{-1}$.^{34,48}

Figure 2.24 and Figure 2.25 show SEM images, GIXRD patterns, and Raman spectra of selenized films prepared from precursors using different $[\text{Cu}]/[\text{Sn}]$ ratios. The kesterite sulfoselenide phase was obtained for all solution conditions. For the films processed using *Recipe 1* and *Recipe 4*, the morphology of the final films is the same after selenization. It should be noted that the selenized films became less copper-poor compared to the starting precursor solutions due to the loss of tin during heat treatment. This phenomenon has been shown in Table 2.4. In order to achieve the ideal copper-poor zinc-rich condition in resulting films, the $[\text{Cu}]/[\text{Sn}]$ ratios in precursors were adjusted to lower values than target values. For example, precursor solutions with $[\text{Cu}]/[\text{Sn}]=1.45$ and 1.53 were chosen to process films with target ratios as ~ 1.76 and ~ 1.80 . Since no significant amounts of secondary phases were observed, it is believed that the changes in $[\text{Cu}]/[\text{Sn}]$ ratio within $1.45\sim 1.74$ range was accommodated by changes in bulk defect concentrations rather than by the formation of secondary phases during the annealing and subsequent selenization.

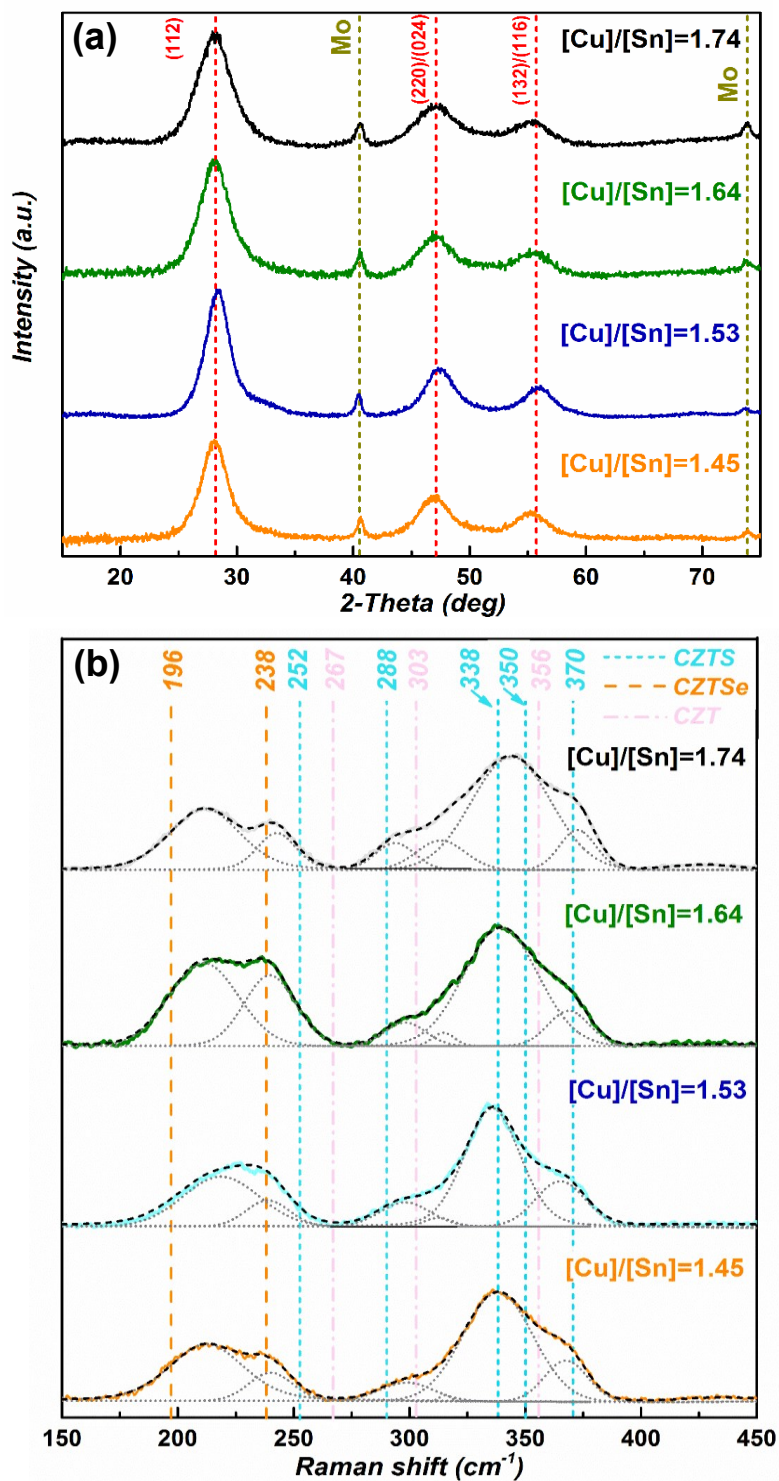


Figure 2.23: a) XRD and b) Raman spectra of precursor films prepared after annealing. The solvents used in precursors are hexylamine and propanethiol.

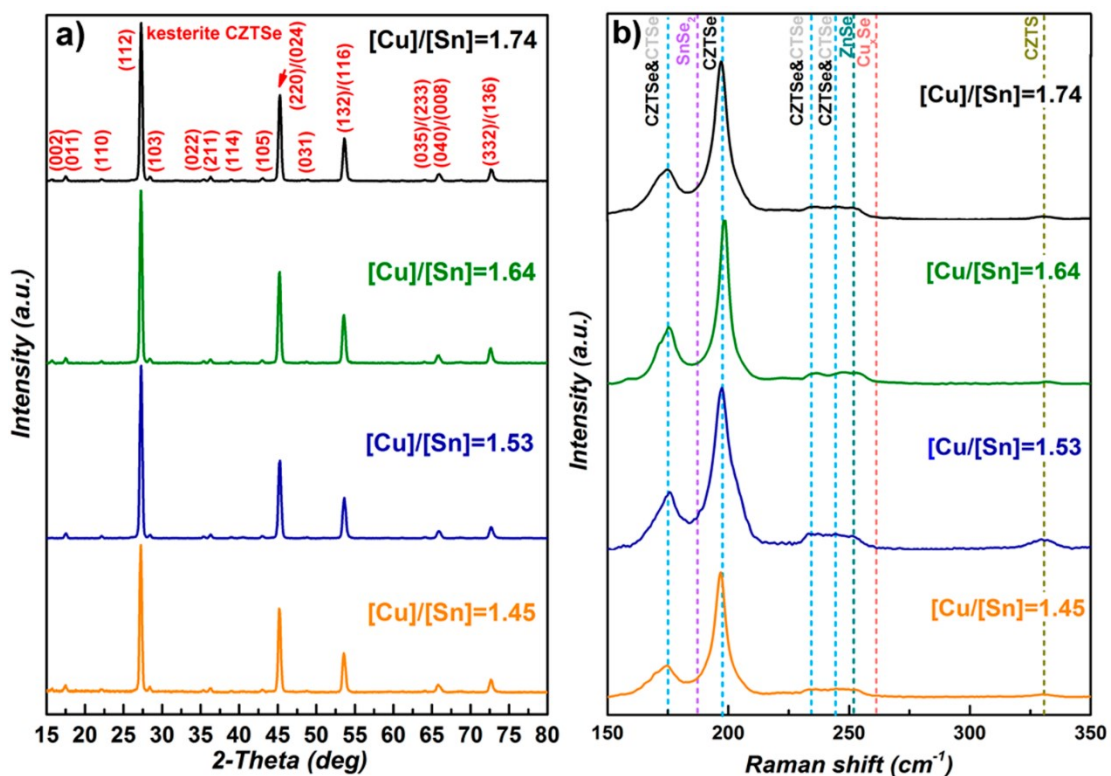


Figure 2.24: a) XRD and b) Raman spectra of CZTSSe films prepared from molecular precursors with different [Cu]/[Sn] ratios.

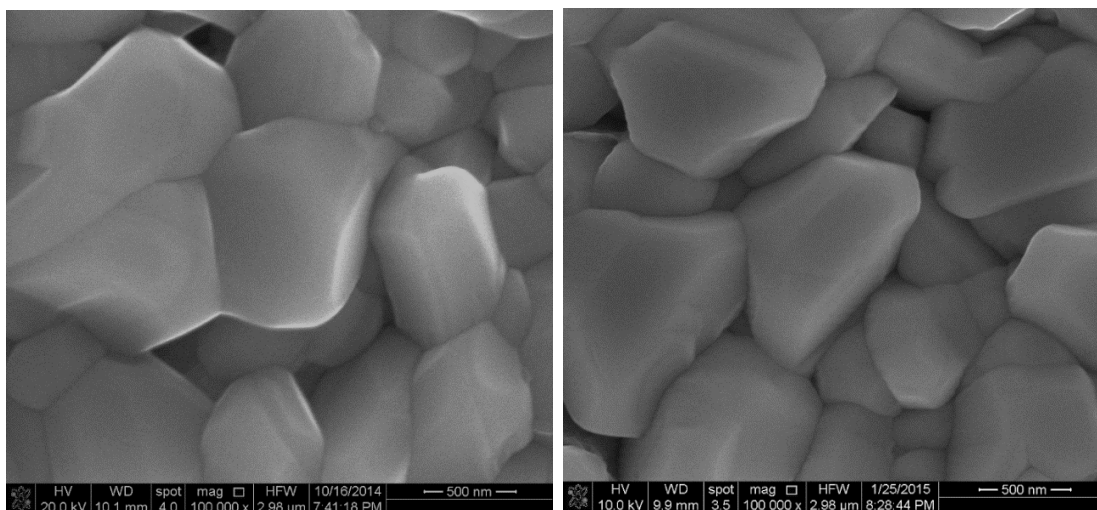


Figure 2.25: Selenized film processed using *Recipe 1* (left) and *Recipe 4* (right) corresponding to [Cu]:[Zn]:[Sn]=1.45:1.05:1 and 1.76:1.05:1, respectively.

Solar cells were fabricated using the aforementioned four precursor recipes and the total area power conversion efficiencies (PCEs) on a total cell area of 0.47 cm^2 were measured under standard AM1.5 illumination. The characteristics of the champion cells and the average total area PCEs with standard deviations for four precursor recipes are summarized in Table 2.6 and Figure 2.26, respectively. At least six device measurements contributed to the data point for each precursor recipe. It should be noted that devices prepared from *Recipe 1* and *Recipe 2* precursor solutions were coated with antireflective coatings, while devices prepared from *Recipe 3* and *Recipe 4* precursor solutions were not coated. The use of antireflective coatings did not influence the trend.

In general, solar cells processed using *Recipe 2* have the highest PCEs ($> 7\%$). The increased concentration in Cu in *Recipe 3* and *Recipe 4* resulted in decreased PCEs. The concentrations of mid-bandgap antisite defects, such as Cu_{Sn} and Cu_{Zn} , should be high in both cases, leading to high recombination rates inside the bulk materials. The EQE in Figure 2.27 shows that the life time of carriers in the cell processed using *Recipe 3* is generally poorer than the cell processed using *Recipe 1*, especially in the longer wavelength range. The high recombination rate in the bulk directly limits the carrier collection. Solar cells processed from *Recipe 1* demonstrated relatively good PCEs ($> 6.5\%$). The possible bulk defects and phase segregation due to the deviation from stoichiometry might have caused lower PCEs compared to cells processed using *Recipe 2*.

Table 2.6: Device characteristics of CZTSSe cells.

Solution recipe	V_{oc}	J_{sc}	FF	PCE
[Cu]:[Sn]	(mV)	(mA/cm^2)	(%)	(%)
R1 1.45:1	381	34.1	58.4	7.24*
R2 1.53:1	382	34.4	60.1	7.86*
R3 1.64:1	367	31.4	55.5	6.34
R4 1.74:1	270	30.0	30.7	2.47

For a total area of 0.47 cm^2 . * With an antireflective coating.

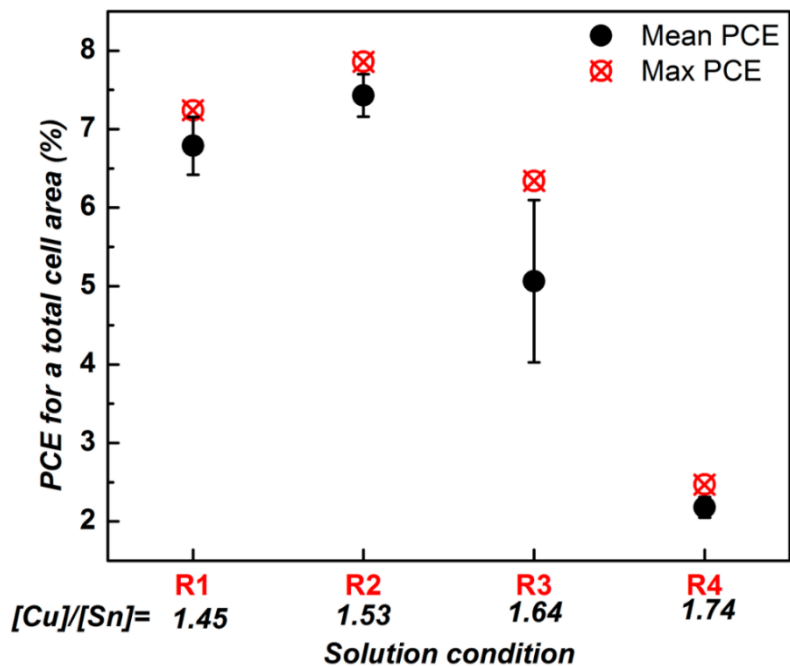


Figure 2.26: Statistics of the total area PCEs of CZTSSe solar cells prepared using four precursor solution recipes.

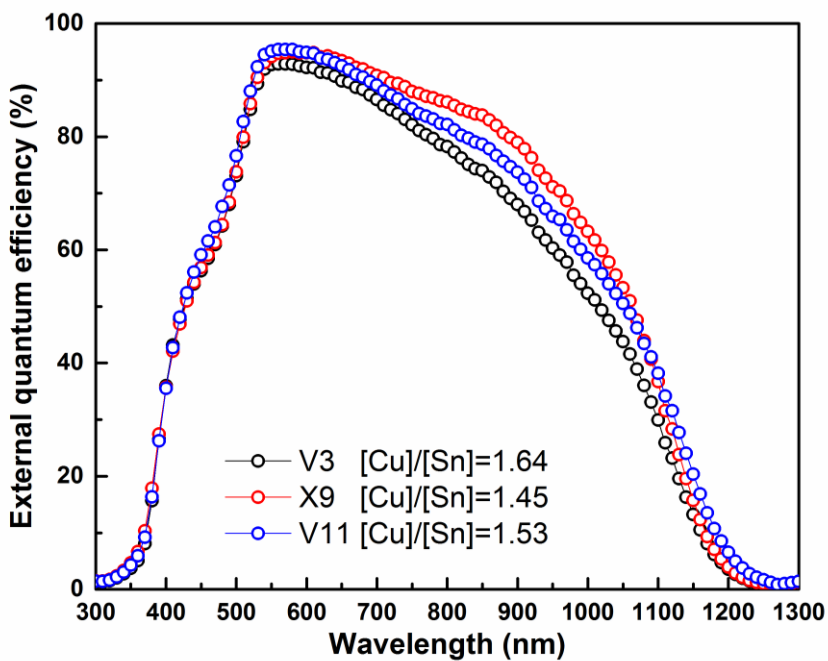


Figure 2.27: EQEs for three devices processed from three recipes.

2.4.6 Solar Cells Processed from Different Metal Salts

During the development of CZTSSe precursor solutions, different metal cation sources were employed. This section presents CZTSSe solar cells prepared using a precursor solution containing CuCl, ZnCl₂, and Sn(acac)₂Cl₂ and a precursor solution containing Cu(II)Cl₂, ZnCl₂, and SnCl₂.

2.4.6.1 Solar Cells Processed from CuCl, ZnCl₂, and Sn(acac)₂Cl₂ Precursor Solution

In the lattice of kesterite CZTSSe structure, Sn should have the valence of 4+. The addition of Sn⁴⁺ rather than Sn²⁺ is preferred in order to maintain its valence in the lattice. The molecular precursor with [Cu]:[Zn]:[Sn]=1.45:1.05:1, [Sn]=0.1 M was prepared following the procedures in section 2.4.1. The XRD patterns in Figure 2.28a show that the kesterite CZTS phase formed after solvent evaporation/annealing step, while the kesterite CZTSSe phase was obtained after selenization. Large grains are formed from the precursor film after selenization as shown in Figure 2.28b. It should be noted that when the precursor solution with [Cu]:[Sn]=1.45:1 (*Recipe 1* in Table 2.5) was adopted, the composition of the resulting film was [Cu]:[Sn]=2:1 based on EDX measurement. This means 27.5% of initial Sn has been lost during the annealing and subsequent selenization. The amount of Sn loss is twice the amount when SnCl₂ is used as the Sn source in the precursor solution. Therefore, when Sn(acac)₂Cl₂ is used as the Sn source, it is necessary to either increase the concentration of Sn relative to Cu in the precursor solution or change the annealing/selenization environment to reduce Sn loss in order to create the desired [Cu]/[Sn] ratio in the final film.

The J-V characteristic of a solar cell and the key parameters of six cells processed using the Sn(acac)₂Cl₂-containing precursor are shown in Figure 2.29 and Figure 2.30, respectively. The solar cell PCEs are lower than the PCEs obtained when SnCl₂ used as the Sn source. The low V_{oc} of six cells (250~270 mV) directly limits the solar cell performance. Two factors resulted in the low V_{oc}. First, the precursor film deposited using Sn(acac)₂Cl₂-containing precursor is much rougher than

the precursor film prepared using SnCl_2 -containing precursor. The high roughness increases the propensity for pinhole formation during selenization process. Second, the high Cu concentration, $[\text{Cu}]:[\text{Sn}]=2:1$, in the final film increases the concentrations of mid-bandgap trapping levels and the propensity to form low-bandgap secondary phases.

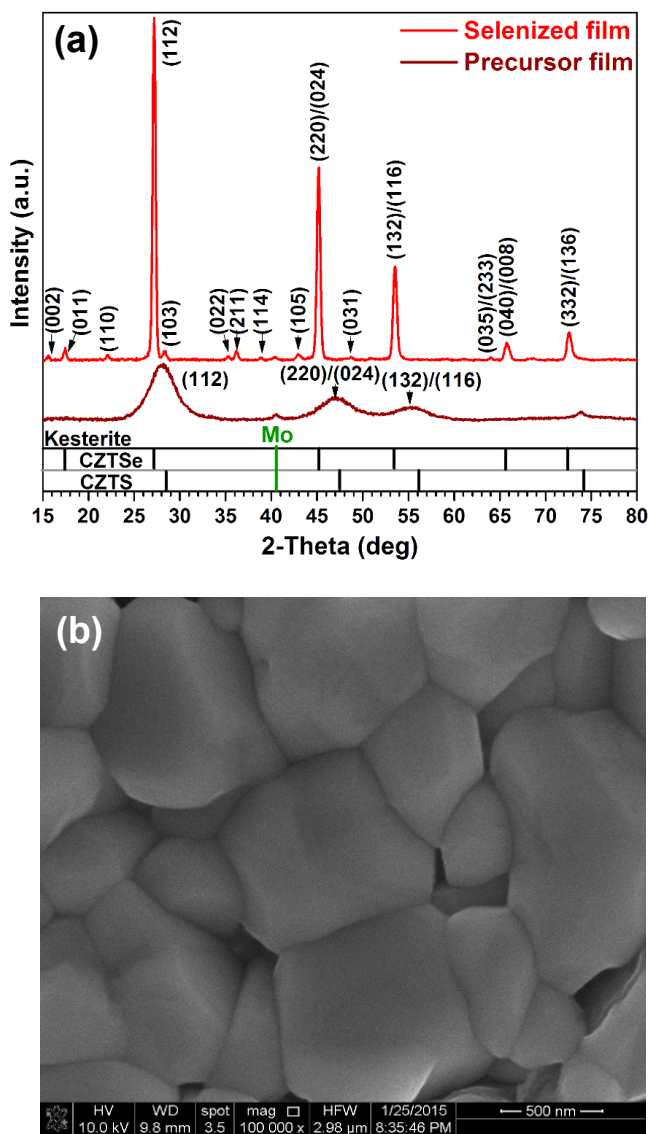


Figure 2.28: a) XRD patterns of the precursor and selenized CZTSSe thin films processed using precursor solution with CuCl , ZnCl_2 , and $\text{Sn}(\text{acac})_2\text{Cl}_2$ in hexylamine and propanethiol (vol. ratio as 4:1). The standards of kesterite CZTSe (space group: $\overline{14}$, JCPDS 01-070-8930) and CZTS (space group: $\overline{14}$, simulated pattern based on JCPDS 01-75-4122) are marked at the bottom of the plot. The annealing and selenization condition were the same as those reported in the manuscript. b) SEM image of selenized film processed using the above precursor solution.

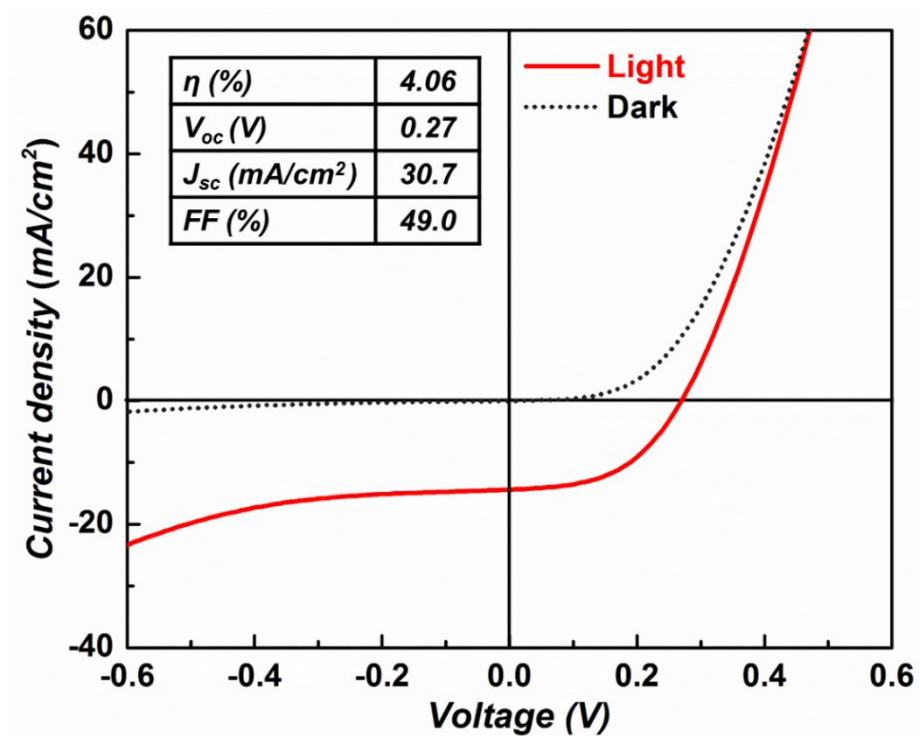


Figure 2.29: J–V curves and key parameters for the best performing cell in the dark and under AM1.5 illumination. The dotted line shows the dark current density, while the solid line represents the light current density.

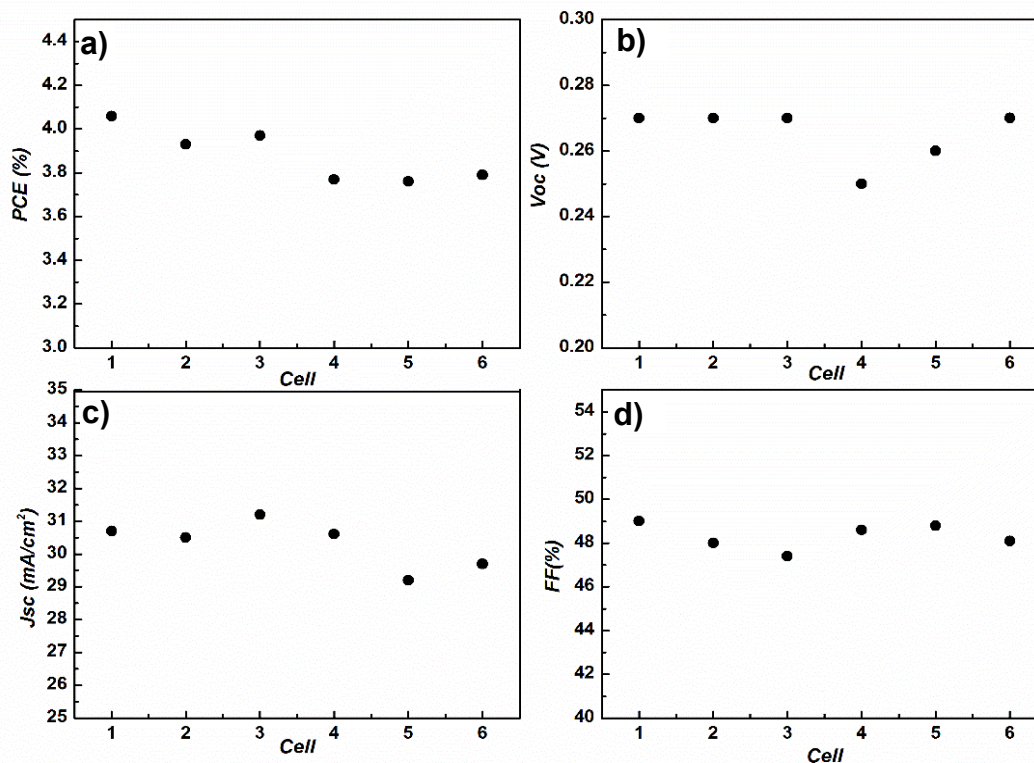


Figure 2.30: Solar cell performance of the six cells on the same one-by-one inch substrate. a) PCE, b) V_{oc} , c) J_{sc} , and d) FF.

2.4.6.2 Solar Cells Processed from CuCl_2 , ZnCl_2 , and SnCl_2 Precursor Solution

Based on mass spectrometry analysis, the solvent mixture of primary amine and monothiol can reduce Cu^{2+} to Cu^+ during the dissolution. To test if CuCl_2 is a good Cu source, a precursor solution containing dissolved CuCl_2 , ZnCl_2 , SnCl_2 , S, and Se was prepared, following the procedures described in section 2.4.1. In the precursor, $[\text{Cu}]:[\text{Zn}]:[\text{Sn}]=1.54:1.05:1$ and $[\text{Sn}]=0.1$ M. As shown in the XRD pattern and Raman spectra (Figure 2.31), kesterite CZTSSe was obtained after the solvent evaporation and selenization process. The J-V characteristics and key parameters of six cells are shown in Figure 2.32 and 2.33. Although perfect kesterite CZTSSe was formed after selenization, the solar cell performance is not comparable to that of solar cells processed from typical precursors using CuCl as the Cu source. The reasons why requires more studies regarding how the relative concentrations of different copper complexes that formed in the precursor solution

can influence the film quality, and how the extra chloride ions affect the electronic defects in the bulk material.

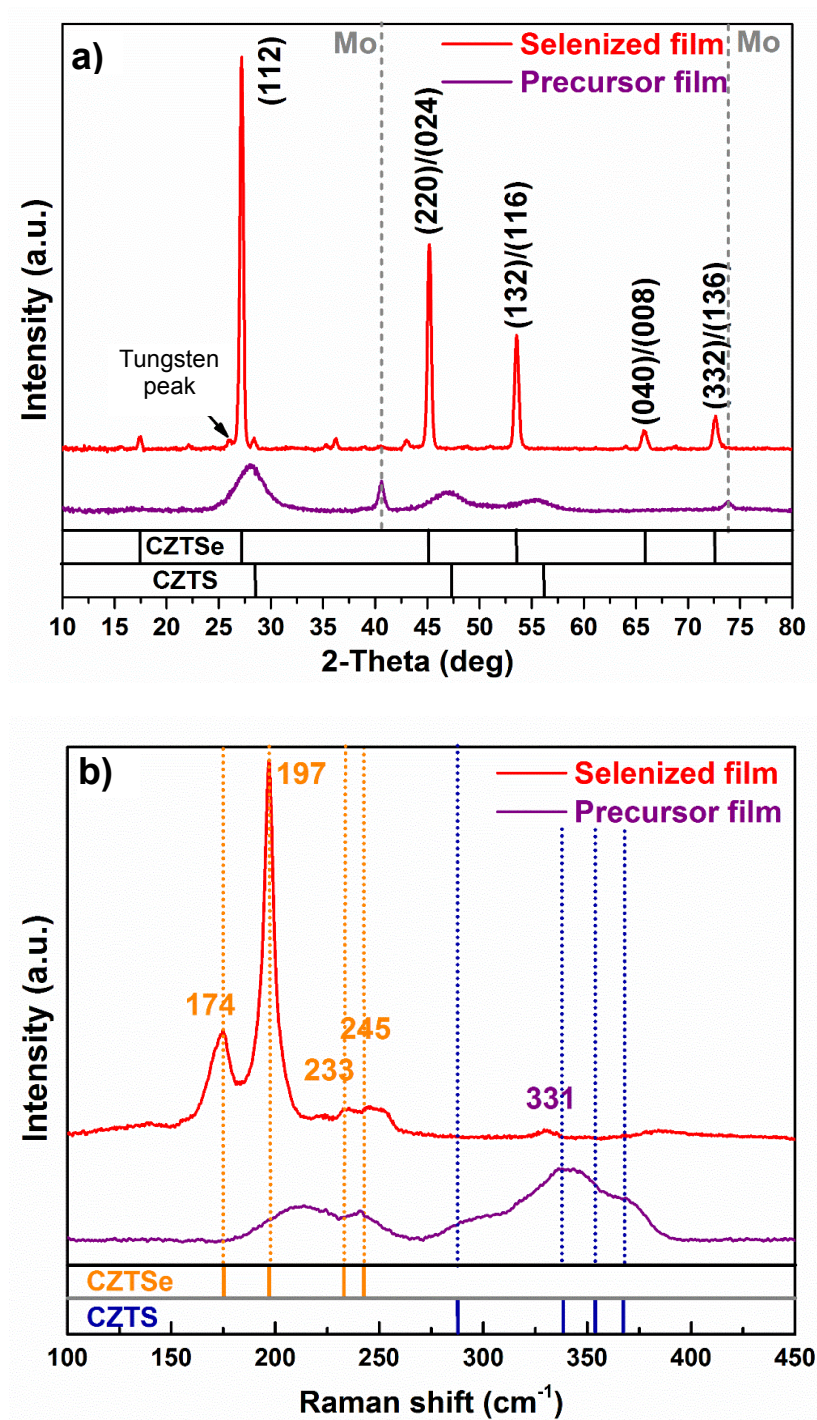


Figure 2.31: a) XRD patterns and b) Raman spectra of precursor and selenized film processed from CuCl_2 , ZnCl_2 , and SnCl_2 precursor solutions.

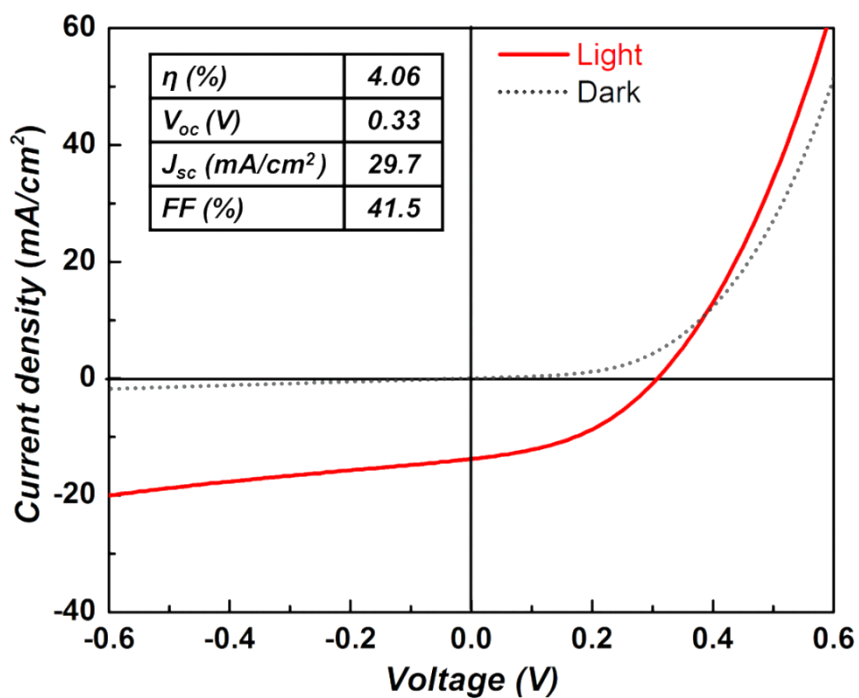


Figure 2.32: J–V curves and performance parameters for the best performing cell in the dark and under AM1.5 illumination. The dotted line shows the dark current density, while the solid line represents the light current density. The series resistance and shunt resistance under light are listed. The inset is the final device.

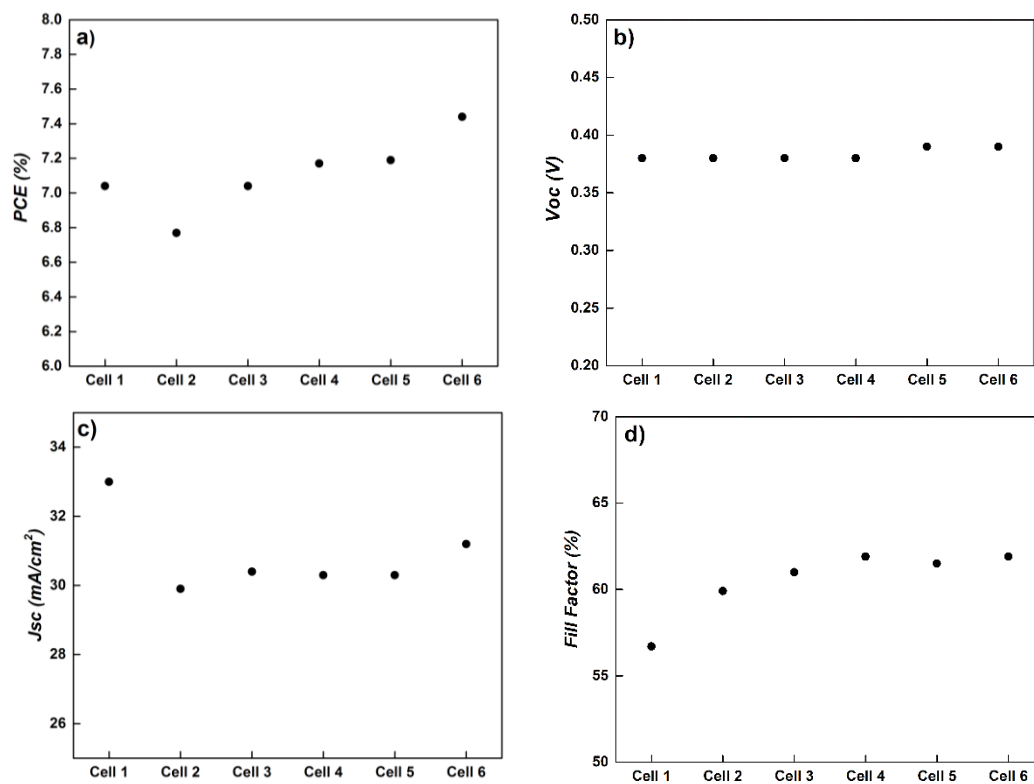


Figure 2.33: Solar cell performance of the six cells on the same one-by-one inch substrate. a) PCE, b) V_{oc} , c) J_{sc} , and d) FF.

2.5 Conclusion

This chapter presents a versatile molecular precursor route to CZTSSe thin film solar cells. The precursor solutions are composed of dissolved metal salts and elemental chalcogens in a mixture of a primary amine and a monothiol. The versatility of this molecular precursor route has been demonstrated in three aspects: 1) pure solutions can be obtained by dissolving different types of cation and anion sources in the amine-thiol solvent mixtures. 2) amine/s and thiol/s employed in a solvent mixture can be any type of primary amine and monothiol, offering the flexibility to change the dissolution process, film fabrication process, and film morphology. 3) cation-to-anion and anion-to-anion ratios can be adjusted freely and independently. The most-studied molecular precursor is prepared by dissolving CuCl, ZnCl₂, SnCl₂, S, and Se in a mixture of hexylamine and propanethiol (vol. ratio 4:1). After the deposition and the annealing processes, kesterite CZTS phase has been formed with no secondary phases detected. The kesterite CZTS was converted into a highly-crystalline CZTSSe phase during the selenization. The homogeneity of this precursor solution ensures the phase purity, the composition uniformity of the final film, and in turn a good solar cell performance. With this molecular precursor route, a power conversion efficiency of 7.86% (8.09%) has been achieved for a total area of 0.47 cm² (an active area of 0.456 cm²) under AM 1.5 illumination. The further optimization of the precursor composition, annealing temperature, and selenization condition should result in higher PCEs.

CHAPTER 3. MICROSTRUCTURAL EVOLUTION DURING ANNEALING AND SELENIZATION

3.1 Introduction

Heat treatment including annealing and selenization of precursor films is a crucial procedure to fabricate electronic-quality CZTS/CZTSSe/CZTSe absorbers. The resulting large-grained structure is desired for the photovoltaic application. Although phase formation and grain growth during the selenization have been investigated by several studies for the colloidal routes,^{63,64} the similar studies has not been performed for the molecular precursor routes. In this study, the structure of the as-annealed precursor film is characterized using high resolution transmission electron microscopy (HRTEM). The phase and microstructural evolution during the selenization is investigated by selenizing precursor films for different periods of time at the same conditions. The film structures, compositions, and phases formed at different selenization periods are examined using SEM equipped with EDX, XRD, and Raman spectroscopy. The corresponding solar cell performances are also reported with the microstructure characterization.

3.2 Experimental Section

To study the microstructure of the as-annealed precursor film, a diluted CZTSSe precursor solution was drop-cast as a thin layer on a Si₃N₄ TEM grid and then annealed at 250°C for 5 min. The CZTSSe precursor solution was diluted to 1/60 of the original concentration using the same solvent mixture of hexylamine and propanethiol (volume ratio 4:1). The films were analyzed in a probe-corrected TEM (Titan, 300kV).

To study the phase evolution of CZTSSe precursor films during the selenization process, films processed in the same conditions were selenized at different times: 5 min, 10 min, 20 min, and 30 min. The preparation of precursor solutions and precursor films was described in section 2.3.1 and 2.3.2., and the selenization setup was presented in section 2.3.3.

After the selenization process, each sample was separated into two pieces. The smaller one was used for morphology and structure characterization, while the larger one was fabricated into solar cells. The morphology and composition were characterized using SEM equipped with SDD-EDX detector. The phase/s were identified using GIXRD and Raman technique. The solar cells were fabricated following the same procedures described in section 2.3.4 and the solar cell efficiencies were measured under the calibrated solar simulator. The correlation between the characteristics of the absorber layers and the solar cell performance was established for each interval of selenization.

3.3 Results and Discussion

3.3.1 Microstructure of Precursor Films

The annealed precursor film was characterized under probe-corrected TEM at 300kV. Figure 3.1 shows that the precursor film is composed of small nanoparticles and amorphous materials after being annealed at 250°C for 5 min. The average size of the nanoparticles ranges from 1 to 4 nm. The size distribution of these in-situ formed nanoparticles is much smaller than that of nanoparticles synthesized from heated solutions with ligands.^{3,34}

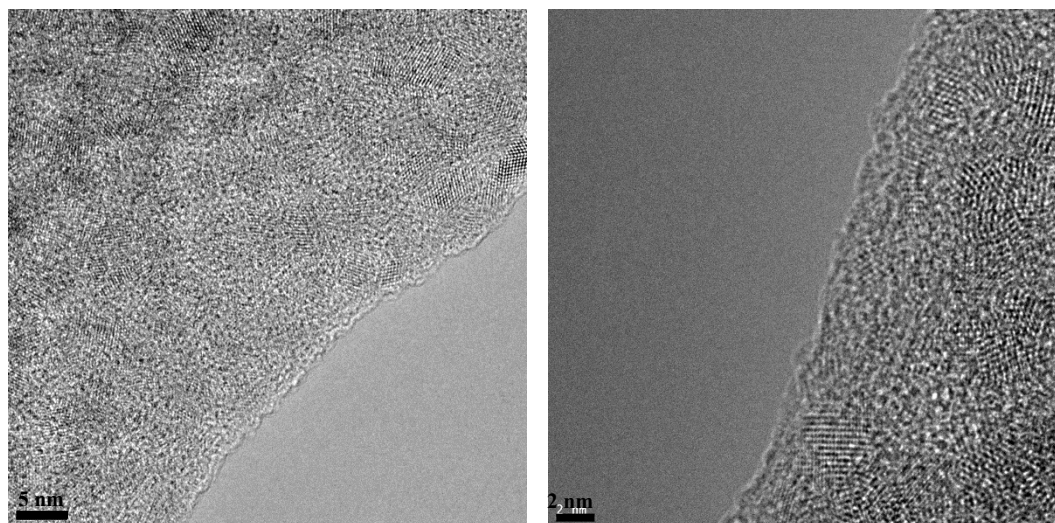


Figure 3.1: TEM images of the annealed precursor film. The scale bar on left image is 5 nm and the scale bar on the right image is 2 nm.

3.3.2 Phase Transformation during Selenization

The top-view and cross-sectional SEM images of CZTSSe films selenized at different times are shown in Figure 3.2. After 5 min selenization, a number of sharp-angled crystals with average size of ~200 nm formed at the film surface. The thickness of this large-grained layer is about 200-300 nm. After 10 min selenization, the size of large crystals increased significantly and the number of crystals dropped concurrently. The average size of grains is >500 nm. Based on Figure 3.2f, about half of the film has been converted into a large-grained layer. The fine-grained layer was consumed by the growth of large-grained layer, meaning it supplied cations to the growth of CZTSe large grains. As the films were selenized for a longer period of time (20 and 30 min), the polyhedron-shaped grains developed rounded corners, but the size of the grains did not change noticeably. A comparison between the top-view SEM images in Figure 3.2c and d, and cross-sectional SEM images in Figure 3.2g and h, revealed that the film roughness was decreased and the continuity was improved after selenization beyond 20 min. In addition, the large-grained layer is prevented from growing thicker, indicating cations were depleted in the fine-grained layer at the bottom.

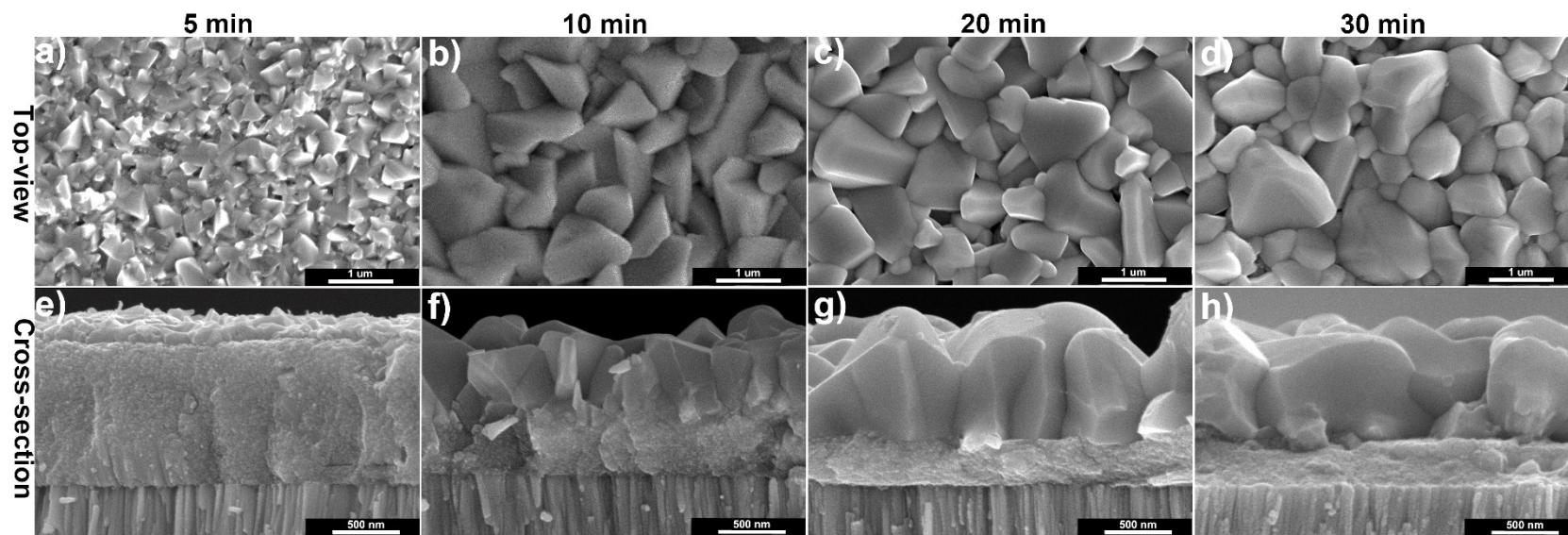


Figure 3.2: Top-view and cross-sectional SEM images of CZTSSe films selenized after 5 min, 10 min, 20 min, and 30 min. The scale bar is 1 μm for a)-d) and 500 nm for e)-h).

Since the selenization involves the reaction between the selenium vapor/condensed liquid phase of selenium and the solid phases in the precursor film, the phase transformation was taking place while the morphology of grains was changing. The phase evolution during the same selenization process was tracked using GIXRD and Raman spectroscopy on the as-selenized films. Figure 3.3a shows the GIXRD patterns from CZTSSe films selenized for 5 min, 10 min, 20 min, and 30 min, and Figure 3.3b shows the magnified views of the reflections corresponding to (112), (220)/(024), (132)/(116) planes. After 5-min selenization, the peaks of (112), (220)/(024), and (132)/(116) became much sharper compared to the peaks shown on GIXRD pattern of the precursor film (Figure 2.16). Continual selenization further improved the size and the crystallinity of CZTSSe grains. As shown in Figure 3.3b, films selenized for 10 min, 20 min, and 30 min exhibit smaller full width at half maximum (FWHM) on major peaks in contrast to films selenized for 5 min. The diffraction peaks corresponding to (110), (103), and (105) planes are clearly resolved in the GIXRD patterns of films selenized beyond 5 min. Note that the large-grained layer is the main contributor to the intensity in XRD, and thus the GIXRD patterns mainly represent the phase changes of the large-grained layers in those samples. As shown in Figure 3.3b, the reflection peaks of (112), (220)/(024), and (132)/(116) from films selenized at different periods of time appear between the corresponding peaks of kesterite CZTS and kesterite CZTSe phase, indicating the formation of kesterite CZTSSe in all cases. With the increase of selenization time, a linear shift of those peaks toward a lower 2-theta angle was observed, indicating Se atoms substituted for S atoms in the lattice during the selenization. This result has a good agreement with Vegard's law, illustrating a linear relation between the lattice parameters and the Se/S ratios.⁶⁵

Owing to its high sensitivity to a small amount of materials, Raman spectroscopy was employed to examine the phase evolution process as a complementary characterization technique. In addition, since the penetration depth of 633 nm-laser on CZTSSe is about 200 nm, the characterization represents the changes at the top surface. Figure 3.4 shows the Raman spectra of as-selenized

samples after different periods of time. The sulfoselenide phase was detected after 5-min selenization, while the sulfoselenide phase converted into selenide phases when selenization was beyond 5 min. This means the phase transformation started at the surface and gradually extended into the film. Herein, “sulfoselenide” means in the formula of $\text{Cu}_2\text{ZnSn}(\text{S}_{1-x}\text{Se}_x)_4$, $0.1 \leq x \leq 0.9$, and “selenide” means in the formula of $\text{Cu}_2\text{ZnSn}(\text{S}_{1-x}\text{Se}_x)_4$, $x \geq 0.9$.

The composition profiles of the films selenized for different periods of time were characterized in SEM equipped with SDD-EDX detector. The truelines generated by Aztec software are plotted to show the relative concentration of Cu, Zn, Sn, S, Se, Mo, and C along the film thickness. As shown in Figure 3.5a, Se vapor penetrated the whole precursor film as early as 5-min selenization. In the fine-grained layer, the concentration of Se is higher near the front of the large-grained layer, and gradually decreases toward the Mo substrate interface. The perturbations in Cu, Zn, Sn and Se profile correspond to the large grains formed on the top of the film. After 10 min-selenization, the Se profile changed significantly. The Se profile shows a higher concentration in the fine-grained layer than in the large-grained layer. The concentration of the Cu, Zn, Sn and S are uniformly distributed inside the large-grained layer. However, the Cu, Zn, Sn, and S show gradients inside the fine-grained layer, having a higher concentration from the side close to the large-grained layer to a lower concentration at the Mo substrate-interface. It is interesting that the positions where the cation concentrations are low correspond to the positions where Se concentrations are high in the fine-grained layer. After 20-min and 30-min selenization, Cu, Zn, Sn, and S are still uniformly distributed in the large-grained layers, while those elements are depleted from the fine-grained layers. The changes in the concentration profiles of the cations indicate the diffusion of Cu, Zn, and Sn from the fine-grained layer to the large-grained layer during the selenization process. The composition fluctuation in the large-grained layers selenized after 30 min is smaller compared to the film selenized after 20 min, meaning that the composition was homogenized during the extra 10-min heat treatment. The C distributions are very uniform in those films processed from

molecular precursors in contrast to the films processed from colloidal inks.⁴⁴ Compared to the long-chain ligands used for stabilizing nanoparticles in colloidal inks, the low-boiling point solvents in the precursors were easily removed after annealing and subsequent high-temperature selenization.

To sum up the above phenomena, i) large selenide grains first nucleated at the top surface of the precursor film, then the large grains then grew downward to form the large-grained layer; ii) the fine-grained layer kept shrinking due to the out diffusion of Cu, Zn, and Sn to the large-grained layer; iii) the phase transformation of sulfoselenide into selenide phase happened as the microstructure was changing; iv) there are three stages during the selenization: stage 1 (within 5 min) which is dominated by the process of nucleation and grain growth, stage 2 (between 10 min to 20 min) which is dominated by the grain growth and coalescence, and stage 3 (beyond 20 min) which is dominated by the densification; v.) the presence of low-temperature Cu-Se phase⁶⁶ and the liquid phase-assisted reaction⁶⁷ may contribute to the fast grain growth of CZTSSe and lead to the formation of the fine-grained layer. The schematic of this process is presented in Figure 3.6. The Se-influenced layer is where Se has penetrated and condensed. According to relevant literature, the cations, especially Cu, have the highest solubility in condensed liquid Se. Therefore, the cations can be transported by a liquid pathway from the fine-grained layer to the growth front of the large-grained layer. It should be noted that the fine-grained layer formed after 30-min selenization is rich in selenium, but depleted in other cations, as shown in Figure 3.5d. The condensed liquid selenium might be trapped by the densified large-grained layer during the final stage of reaction. In another quick experiment, a single layer of precursor layer is applied on the substrate. Since the large-grained layer formed from this single precursor layer is not continuous, no fine-grained layer was observed in the final structure. The porous large-grained layer allowed Se to escape during the cooling process.

3.3.3 Solar Cell Performance

Table 3.1 shows the efficiencies and typical characteristics of solar cells fabricated from the films selenized for different periods of time. In general, the V_{oc} , J_{sc} , and FF were improved with the selenization time within 30 min. The V_{oc} shows the highest value after 20-min selenization, while J_{sc} and FF show the highest value after 30-min selenization. Those changes correspond to the changes in the microstructure and compositions of the selenized films. In contrast to film selenized for 5 min, the thickness of the fine-grained layer shrunk significantly, while the thickness of the large-grained layer increased after 10-min selenization. The series resistance decreased due to the changes, and contributing to the doubled J_{sc} as well as increased V_{oc} . The highest V_{oc} is achieved after 20-min selenization, which might be attributed to the higher S concentration in this film compared to the film selenized for 30 min. The FF also was improved during the selenization, especially during the subsequent 10-min selenization after 20 min. The improved composition fluctuation and continuity of the large-grained layer improved the FF. Low-temperature post-annealing and the elimination of Se-rich fine-grained layer might further improve the efficiencies by decreasing the detrimental defect densities and series resistance.

Table 3.1: Device characteristics of CZTSSe cells.

Selenization time (min)	V_{oc} (mV)	J_{sc} (mA/cm ²)	FF (%)	PCE (%)
5	300	14.4	34.0	1.48
10	360	26.1	42.4	4.02
20	400	29.1	55.9	6.55
30	382	29.9	59.9	6.77

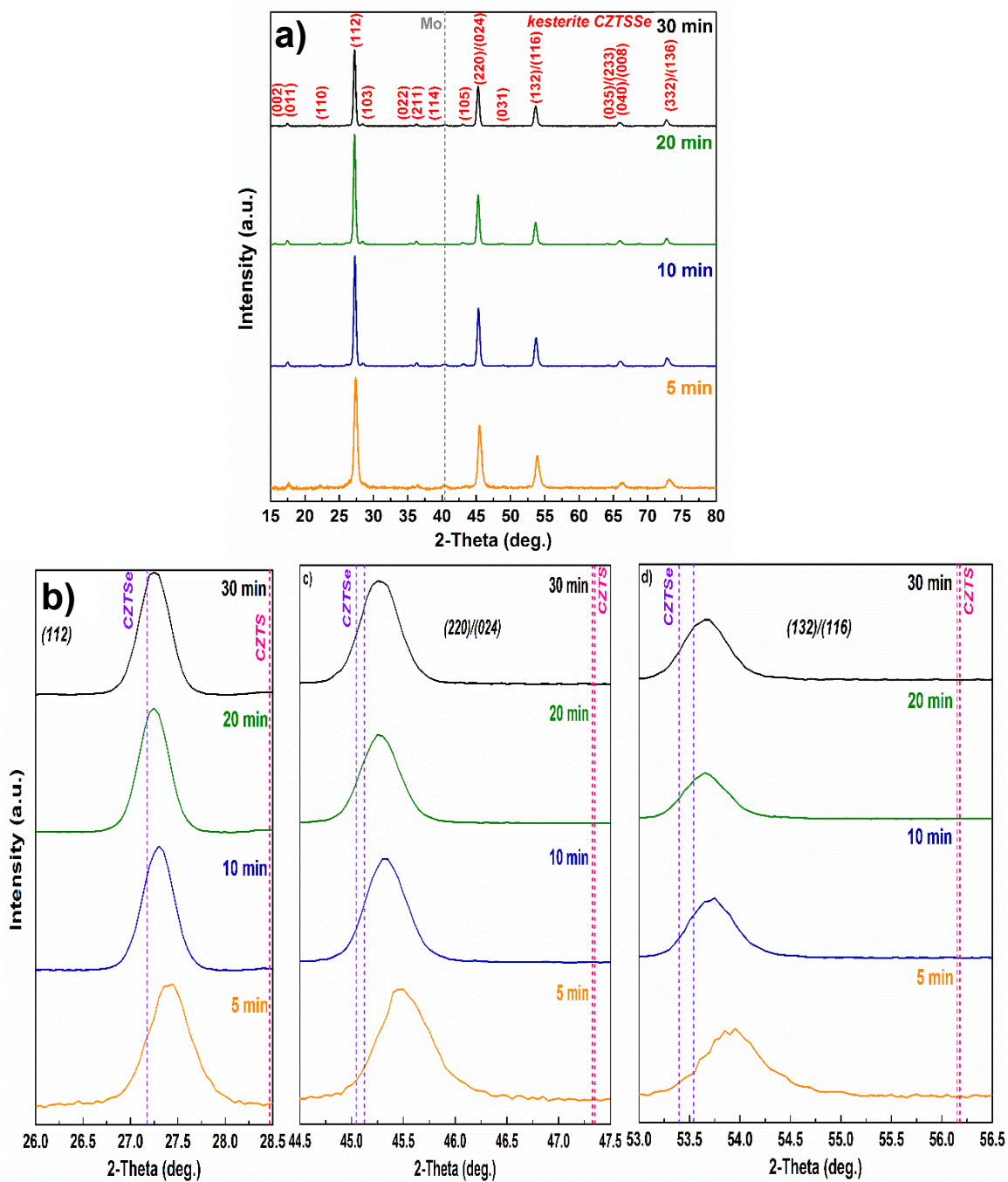


Figure 3.3: a) GIXRD patterns of films selenized for 5 min, 10 min, 20 min, and 30 min (bottom to top). b) magnified diffraction peaks from (112), (220)/(024), and (132)/(116) planes, which are three major XRD peaks from the kesterite structure. The purple lines show the standard peak position of kesterite CZTSe phase (JCPDS 01-070-8930) and the bright pink lines show the simulated standard peak position of kesterite CZTS phase (JCPDS 01-75-4122).

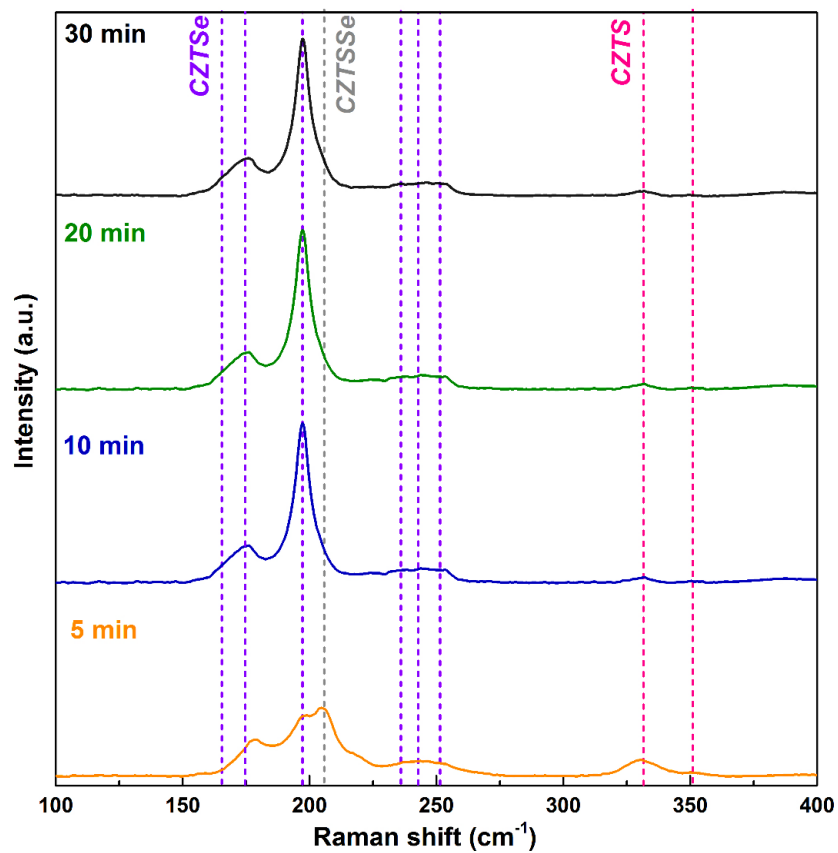


Figure 3.4: Raman spectra of the films selenized for 5 min, 10 min, 20 min, and 30 min. The purple lines show the standard peak position of kesterite CZTSe phase (JCPDS 01-070-8930) and the bright pink lines show the simulated standard peak position of kesterite CZTS phase (JCPDS 01-75-4122).

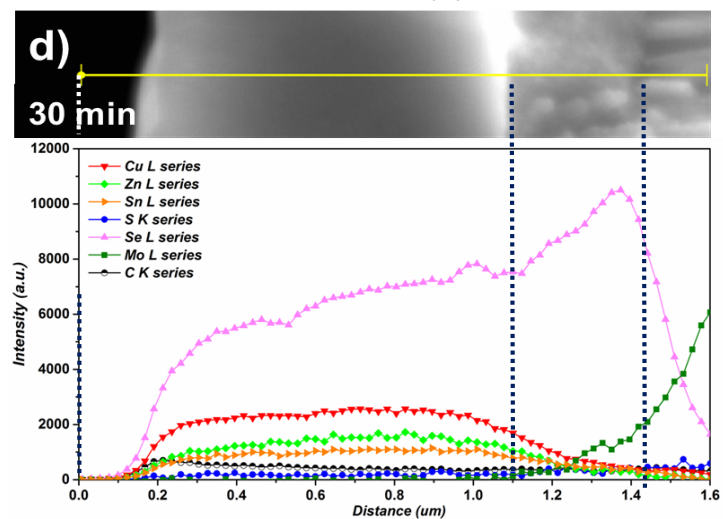
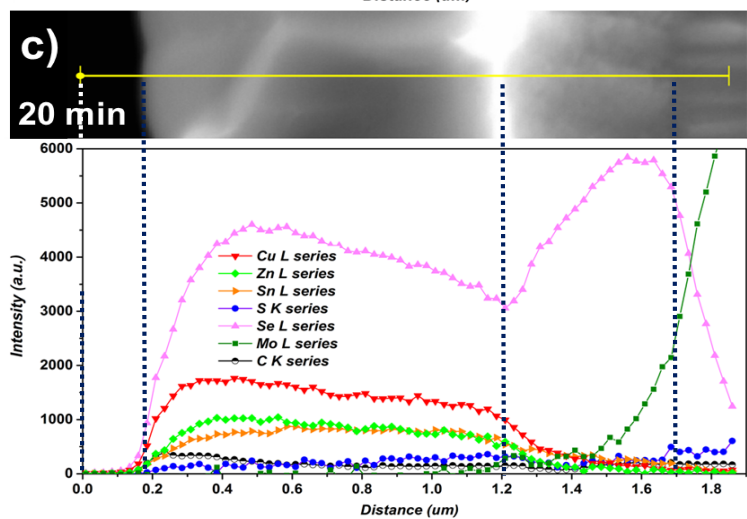
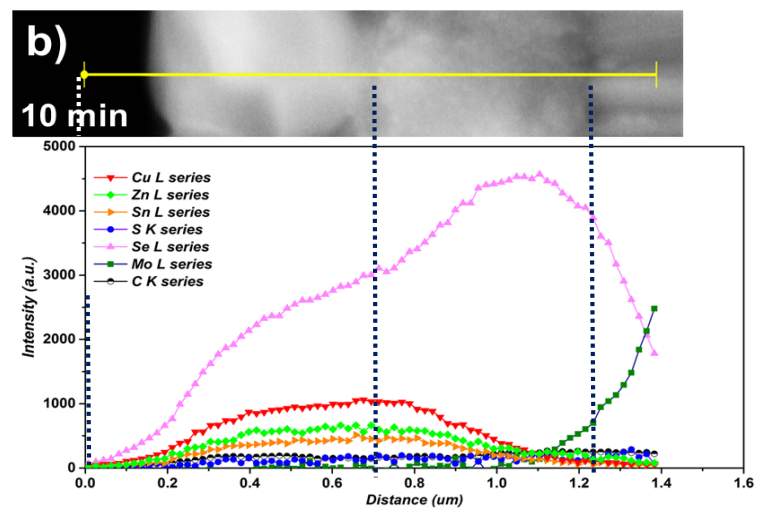
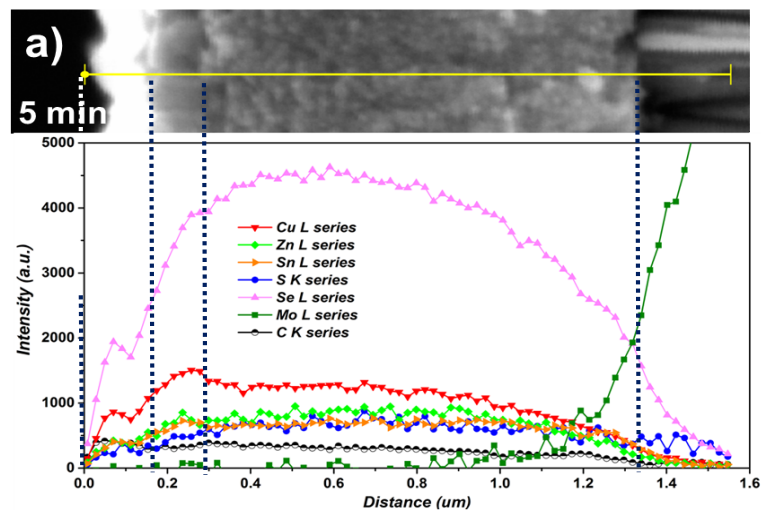


Figure 3.5: SEM-EDX linescans on cross-sections of films selenized for 5 min, 10 min, 20 min, and 30 min.

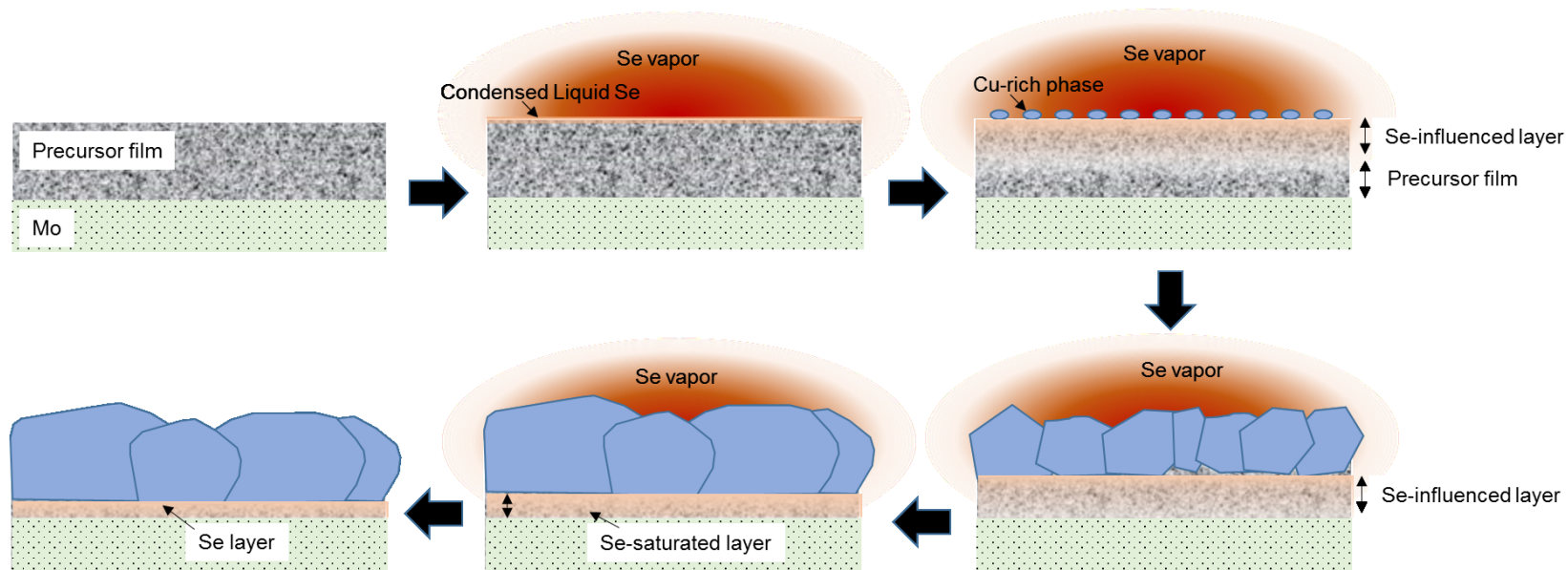


Figure 3.6: Schematic process of selenization.

3.4 Conclusion

After the annealing process, the precursor film deposited from CZTSSe molecular precursor converts into films composed of in-situ formed nanoparticles and amorphous materials. During the selenization, large grains grow by consuming those nanoparticles in the precursor films. The large grains first nucleate from the top of the precursor film, and then grow downward. The typical selenized structure contains a CZTSSe (mainly CZTSe) large-grained layer and a Se-rich fine-grained layer at the bottom. The liquid-phase assisted grain growth is expected to take place during the selenization based on three facts: 1) the rapid cation transportation from the precursor film to the reaction front leads to fast grain growth; 2) the maxima of Se concentration profile corresponds to where the large-grained layer ends; 3) a huge amount of Se is detected in the fine-grained layer formed after 30-min selenization. It is proposed that the liquid-phase Se condenses from the saturated vapor at small pores between the in-situ formed nanoparticles. Then, the liquid phase dissolves the unstable nanoparticles and serves as the mass transportation channels for the grain growth at the reaction front. During the stage of film densification and sample cooling, the densified large-grained layer traps the liquid-phase Se at the bottom, and thus a Se-rich fine-grained layer forms. Since the molecular precursor-processed films do not suffer from C contamination, it has been demonstrated that the Se condensation does not correlate to the segregation of C species in films. This study provides insights into phase transformation and microstructural evolution of the molecular precursor-processed CZTSSe thin films, and initiates the further optimization in heat treatment for high-quality films.

CHAPTER 4. DEPOSITION OF METAL CHALCOGENIDE THIN FILMS USING METAL-METAL CHALCOGENIDE PRECURSOR SOLUTIONS

4.1 Introduction

Metal chalcogenides, such as Cu_2S , Cu_2Se , CuS , CuSe , SnS , SnSe , ZnS , ZnSe , $\text{Cu}_2\text{Sn}(\text{S}_x\text{Se}_{1-x})_3$, ($0 \leq x \leq 1$) (CTSSe) and $\text{Cu}_2\text{ZnSn}(\text{S}_x\text{Se}_{1-x})_4$ ($0 \leq x \leq 1$) (CZTSSe) are important semiconductor materials receiving substantial research attention. For example, Cu_2S , Cu_2Se , SnS , and CZTSSe, are widely studied for photovoltaic applications due to their suitable band gaps, high light absorption coefficients, and earth-abundance.^{3,33,68-72} ZnS and ZnSe with different nanostructures have been synthesized for light emitting diodes,^{73,74} transparent conductive electrodes,⁷⁵ and piezoelectrics.^{76,77} Also, the thermoelectric properties of Cu_{2-x}Se , SnSe , and CZTSSe are recently investigated by many research groups.⁷⁸⁻⁸⁰ The present electronics industry trends to lower manufacturing costs and to create wearable and flexible electronic devices, call for methods allowing inexpensive and low-temperature roll-to-roll printing of semiconductor thin films on large areas. Compared to vacuum-based deposition methods (e.g. CVD, PVD, co-evaporation, and co-sputtering) which require significant capital equipment and complex procedures, the direct solution processing of the metal chalcogenide thin films/nanostructures has great potential to fulfill these requirements. However, the extremely low solubility of the metal and chalcogenide sources in most of common solvents, coupled with impurity contamination derived from the element sources and solvents, have previously slowed down the development of direct solution methods. To date, the most successful direct solution approach for depositing metal chalcogenide thin films is based on

hydrazine solutions. By using hydrazine, Mitzi et al. dissolved SnS_2 and In_2Se_3 powders and deposited $\text{SnSe}_{2-x}\text{S}_x$ and In_2Se_3 as the active layers in thin film transistors (TFTs).^{81,82} Similar methods were also applied to fabricate thin film solar cells, achieving power conversion efficiencies (PCEs) of CIGSSe solar cell as 15.2%^{41,45,83} and CZTSSe solar cell as 12.6%.^{40,46} Unfortunately, using hydrazine creates additional safety and health risks during device processing due to its high toxicity and instability. It is therefore highly favorable to develop an alternative solvent system which is less toxic, more stable, and able to dissolve more diverse materials.

Several recent studies focused on using a solvent mixture of 1,2-ethylenediamine and 1,2-ethanedithiol to dissolve metal chalcogenides.⁸⁴⁻⁸⁶ Webber et al. first reported that nine V_2VI_3 chalcogenides are soluble in a mixture of 1,2-ethylenediamine and 1,2-ethanedithiol with a volume ratio of 10:1.⁸⁴ Then, Lin et al. showed that Cu_2S , Cu_2Se , In_2S_3 , and In_2Se_3 are soluble in the same solvent, and semiconductor alloys, $\text{CuInS}_x\text{Se}_{1-x}$ ($x=0\sim 1$), were prepared by annealing combined metal-chalcogenide solutions.⁸⁶ Although those studies show that potential of implementing the precursor solutions in device fabrication, the performances of the finished devices have not been reported. In Chapter 2, a molecular precursor route using metal salt precursor solutions to process CZTSSe thin film solar cells was reviewed. The highest PCE achieved is 7.86% on a total area of 0.47 cm^2 . In this Chapter, another molecular precursor route based on metal-metal chalcogenide precursor solutions is reported. Herein, the dissolution of pure metals (e.g. Cu, Zn, Sn, and In) and metal chalcogenides (e.g. Cu_2S , Cu_2Se , CuS , CuSe , SnS , SnSe , In_2S_3 , In_2Se_3 , Ag_2S , and Ag_2Se) in a mixture of primary amine-dithiol solvent mixture, and the deposition of metal chalcogenide thin films (e.g. CuS , SnS , CTSSe , and CZTSSe) are demonstrated. Since Zn metal can readily dissolve in this primary amine-dithiol solvent mixture, resulting in a stable solution at room temperature, it is more suitable to use this solvent mixture than hydrazine or hydrazine derivatives to process CZTSSe thin films. The CZTSSe solar cells with PCEs of 6.84% and 7.02% have been fabricated using metal-chalcogenide precursor solutions and metal precursor solutions, respectively.

4.2 Experimental Section

4.2.1 Dissolution of Pure Metals and Metal Chalcogenides

A series of dissolution experiments was performed by mixing Cu, Zn, Sn, In, Cu₂S, Cu₂Se, CuS, CuSe, SnS, SnSe, In₂S₃, In₂Se₃, Ag₂S, and Ag₂Se with butylamine (BA)/hexylamine (HA) and 1,2-ethanedithiol (EDT) (vol. ratio 1:1) at room temperature in a nitrogen-filled glovebox with both water and oxygen level <0.1 ppm. The sequence of adding solutions has no observable influence on the resulting solutions. The standard preparation sequence was: (i.) solid powders, (ii.) BA/HA, (iii.) EDT. It should be noted that none of the above powders dissolve in either primary amines or 1,2-ethanedithiol. The highest solubility (wt.%) of a metal or a metal chalcogenide in primary amine-dithiol solvent mixture was determined experimentally by observing how much bulk powders dissolved in a mixture of BA-EDT (vol. ratio of 1:1) at room temperature within ten days. Although the dissolution experiment was first performed inside the nitrogen-filled glovebox, it was demonstrated that most of above bulk powders can be dissolved in BA/HA-EDT in air atmosphere.

4.2.2 Preparation of CZTSSe Precursor Solutions

The preparation of CZTSSe precursor solutions involves the formation of component solutions, and then the mixing of component solutions. The detailed procedures for component solutions and precursor preparation are described as follows.

1) Component solutions for *Solution 1: CZTS precursors* were prepared as follows: *Solution A* (Cu₂S solution) was prepared by dissolving Cu₂S powder (0.210 g) in HA-EDT solvent mixture (vol. ratio of 1:1) (3 ml), forming a clear, dark brown solution after two days of stirring. *Solution B* (Zn solution) was prepared by dissolving Zn powder (0.103 g) in HA-EDT solvent mixture (vol. ratio of 1:1) (2 ml), yielding a clear, pink solution after few hours of stirring. *Solution C* (SnS solution) was prepared by dissolving SnS powder (0.0226 g) in HA-EDT solvent mixture (vol. ratio

of 1:1) (5 ml), resulting in a colorless transparent solution after seven to ten days of stirring. *Solution 1* was prepared by mixing the above constituent solutions, and then diluted with HA at appropriate volume ratios, yielding a target concentration and elemental ratios at $[\text{Sn}] = 0.1 \text{ M}$, $[\text{Cu}]:[\text{Zn}]:[\text{Sn}] = 1.76:1.05:1$. Note that no sulfur solution was added during the preparation of the precursor solution, since 1,2-ethanedithiol and sulfides supplied the sulfur during the film formation. The solution formed is clear brown color and stable over months.

2) Component solutions for *Solution 2: CZTSSe precursor* were prepared as follows: *Solution A'* (Cu_2Se solution) was prepared by dissolving Cu_2Se powder (0.244 g) in a mixture of HA-EDT solvent mixture (vol. ratio of 1:1) (3 ml), forming a clear, dark red solution after two days of stirring. *Solution B'* (Zn solution) was formed by dissolving Zn powder (0.103 g) in HA-EDT solvent mixture (vol. ratio of 1:1) (2 ml). *Solution C'* (SnSe solution) was prepared by dissolving SnSe powder (0.297 g) in HA-EDT solvent mixture (vol. ratio of 1:1) (5 ml), resulting in a clear, orange solution after seven to ten days of stirring. *Solution D'* (S solution) was prepared by dissolving S (0.385 g) and Se (0.948 g) in HA-EDT (vol. ratio of 1:1) (6 ml). *Solution 2* was prepared by mixing the above constituent solutions at appropriate quantities and then diluted with HA, yielding a target concentration and elemental ratios at $[\text{Sn}] = 0.1 \text{ M}$, $[\text{Cu}]:[\text{Zn}]:[\text{Sn}]:[\text{S}]:[\text{Se}] = 1.45:1.05:1:2:2$. The solution is transparent red color and stable over months. It should be noted that the solvent mixture in *Solution 1* and *Solution 2* sometimes crystallize at room temperature; vortexing or stirring will reverse the crystallization. The crystallization of the solvent mixture has been demonstrated by mixing HA and EDT at volume ratio of 1:1 without the addition of solute.

3) Component solutions for *Solution 3: CZTSSe precursor* were prepared as follows: *Solution A''* (Cu solution) was prepared by dissolving Cu powder (0.092 g) in a mixture of HA-EDT solvent mixture (vol. ratio of 1:1) (4 ml), forming a clear, light red solution after three days of stirring. *Solution B''* (Zn solution) was formed by dissolving Zn powder (0.069 g) in a mixture of HA-EDT solvent mixture (vol. ratio of 1:1) (2 ml). *Solution C''* (Sn solution) was prepared by dissolving Sn

powder (0.119 g) in a mixture of HA-EDT solvent mixture (vol. ratio of 1:1) (5 ml), resulting in a clear pink, solution after five to seven days of stirring. *Solution D''* (S solution) was prepared by dissolving S (0.385 g) and Se (0.948 g) in HA-EDT solvent mixture (vol. ratio of 1:1) (6 ml). *Solution 3* was prepared by mixing the above constituent solutions at appropriate quantities, yielding a target concentration and elemental ratios of $[\text{Sn}] = 0.1 \text{ M}$, $[\text{Cu}]:[\text{Zn}]:[\text{Sn}]:[\text{S}+\text{Se}] = 1.45:1.05:1:5$. The solution is a transparent red and stable over months.

4.2.3 Deposition of Chalcogenide Thin Films

Precursor films were deposited by spin coating (or drop casting for few samples) the precursor solutions on the molybdenum-coated soda lime glasses. The spin coating and post annealing process was performed in a nitrogen-filled glovebox with water and oxygen levels $< 0.1 \text{ ppm}$. For the deposition of binary thin films, the substrates were firstly flooded with the corresponding binary precursors and then spun at 800 rpm for 30 sec.

For the deposition of CZTSSe precursor films, the spin coating process is programmed at 500 rpm for 5 sec and 1500 rpm for 25 sec. After the deposition of each precursor layer, the thin film was annealed at $\sim 300^\circ\text{C}$ for 5 min. These steps were repeated until the desired thickness was acquired. Then, the thin film was further annealed at 500°C in selenium atmosphere for 30 min to achieve a large-grained morphology. The selenization condition is described in section 2.3.3.

4.2.4 Thin Film Characterization

Powder XRD data were collected using a Rigaku diffractometer (Cu K_α radiation, 1.54 nm wavelength). Raman spectra were gathered from HORIBA with an exciton wavelength of 633 nm. The thin film morphology and compositions were characterized under FEI Quanta scanning electron microscopy (SEM) equipped with energy X-ray dispersive spectroscopy (EDX) in FEI Quanta equipped with an Oxford Aztec Xstream-2 silicon drift detector. FIB-lift off samples were

processed in FEI Helios, and then characterized with 200kV Hitachi 2700C equipped with Bruker SDD EDX.

4.2.5 Solar Cell Fabrication and Characterization

The CZTSSe absorbing layer was fabricated based on the direct solution route. The material layers from the bottom to the top of a complete device are: soda lime glass (SLG, ~2 mm), fiber-textured molybdenum film (Mo, ~800 nm), chemical bath deposited cadmium sulfide (CdS, ~50 nm), sputtered intrinsic zinc oxide (ZnO, ~80 nm) and tin-doped indium oxide (ITO, ~220 nm), and e-beam deposited Ni/Al metal contacts. A ~100 nm antireflective magnesium fluoride (MgF₂) coating was applied on the cell prepared from *Solution 2*. The J-V characteristics were measured with a four-point probe station using a Keithley 2400 series sourcemeter and a Newport Oriel simulator with AM 1.5 illumination. The solar simulator was calibrated to 100 mW/cm² using a Si reference cell certified by NIST.

4.3 Results and Discussion

4.3.1 Dissolution of Pure Metals

The bulk metals, like Cu, Zn, and Sn, are difficult to dissolve in common organic solvents. Especially, Zn, ZnS, or ZnSe are challenges for many solvents, even for anhydrous hydrazine. To compromise this situation, a hydrazine-based slurry comprised of dissolved Cu_2S , SnSe , S, Se, and insoluble $\text{ZnX}-(\text{N}_2\text{H}_4)$ ($\text{X}=\text{S}$, Se) particles, which are formed in situ in the slurry, was previously used for the deposition of CZTSSe thin films.⁸⁷ The spatial composition fluctuation of the as-deposited precursor films is significant due to the formation of $\text{ZnX}-(\text{N}_2\text{H}_4)$ ($\text{X}=\text{S}$, Se) particles in hundreds of nanometers.^{40,87} Later on, the efficiency was increased slightly by replacing insoluble Zn metal with soluble zinc chloride in hydrazine-based CZTSSe precursors.⁴² This indicates that compositionally homogeneous precursors performs better in processing good-quality films. However, it is well-known that semiconductors are highly sensitive to impurities, and thus the addition of chloride ions might introduce contamination. By introducing hydrazinocarboxylic acid into hydrazine, Yang et al. incorporated Zn metal as soluble complexes into hydrazine, resulting a real molecular precursor for CZTSSe deposition.^{50,88} Unfortunately, the formation of hydrazinocarboxylic acid is highly exothermic and this complex agent is highly corrosive and reactive to stainless steel.⁵⁰ In this present study, we report a method of using a primary amine-dithiol solvent mixture to dissolve Zn metal and then prepare compositionally homogeneous CZTSSe molecular precursors. This method completely avoids the usage of hydrazine which is highly toxic and unstable, ensures the complete incorporation of Zn ions at molecular level, eliminate the potential contamination from the metal salts, and enhances the spatial composition uniformity throughout the precursor films during the deposition.

To prepare a Zn precursor solution, Zn metal powders were weighed in a glass vial. Then, BA and EDT were sequentially added into the glass vial. A significant amount of gas was generated as

soon as EDT was added into BA. Note that neither pure BA nor EDT will dissolve Zn powders. The solution became a clear liquid with light pink color after around 2 h stirring (Figure 4.1a). The solution does not precipitate out over time, indicating very stable metal complexes was formed during the reaction between the metal and the solvent mixture. Based on a quick experiment, the solubility of Zn metal in a BA-EDT solvent mixture (vol. ratio of 1:1) is ~ 0.78 M. The same dissolution process was observed when the solvent mixture of HA-EDT (vol. ratio of 1:1) was used.

The as-deposited and annealed films of Zn solution were characterized using GIXRD (Figure 4.1a). After annealing at 300°C for 10 min, the amorphous precursor film converted to ZnS which is composed of zinc-blend (F-43m) and wurtzite ZnS (P6₃m) phases. This indicates that EDT acts as a sulfur source for the conversion of a metal into its corresponding metal sulfide. If the sulfur source is provided externally by adding a sulfur solution in pure HA into a Zn solution, the crystallinity of the film was improved. The ZnS formed also contains both zinc-blend and wurtzite crystal structures.

To qualitatively understand why pure metals can dissolve in this amine-dithiol solvent mixture, electrolytic conductivity measurements were performed on BA, HA, EDT, a solvent mixture of BA-EDT (vol. ratio 1:1; molar ratio 1:1.18), a solvent mixture of HA-EDT (vol. ratio 1:1; molar ratio 1:1.57), and solutions with dissolved Zn metals ($[\text{Zn}] = 0.3 \sim 0.7$ M) at 25°C . The electrolytic conductivities of BA, HA, and EDT were measured. Then, amine and dithiol were mixed homogeneously for the measurements of solvent mixtures. The solutions with different Zn concentrations were prepared by dissolving increasing amount of Zn metal in the same solvent mixture. Conductivity measurements were performed as soon as clear solutions formed. Table 4.1 shows the conductivities measurement results.

Table 4.1: Conductivities of solvents and Zn solutions at room temperature.

Solvent	Zn Concentration (M)	Conductivity ($\mu\text{S}/\text{cm}$)
Butylamine (BA)	N/A	0
Hexylamine (HA)	N/A	0
1,2-Ethanedithiol (EDT)	N/A	0
BA-EDT (vol. ratio 1:1)	0	1926.5
BA-EDT (vol. ratio 1:1)	0.3	1500.8
BA-EDT (vol. ratio 1:1)	0.5	1274.4
BA-EDT (vol. ratio 1:1)	0.7	960.7
HA-EDT (vol. ratio 1:1)	0	550.2
HA-EDT (vol. ratio 1:1)	0.3	502.0
HA-EDT (vol. ratio 1:1)	0.5	428.6
HA-EDT (vol. ratio 1:1)	0.7	327.7

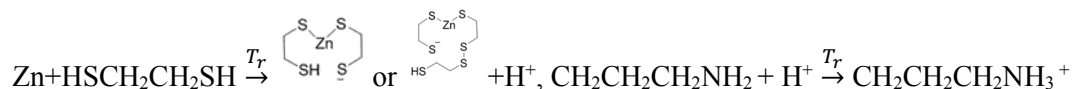
In order to analyze the equilibrium species in Zn solutions, electrospray ionization mass spectrometry (ESI-MS) was employed and the result from the negative mode is shown in Figure 4.1b. The soft character of ESI-MS can minimize fragmentation, leaving mostly unaltered species existing in the solution. As shown in Figure 4.1b, the major peak at around 249 m/z is attributed to



. The structure of this complex is similar to the reported zinc ethane-1,2-dithiolato complexes, $[\text{Zn}(\text{edt})_2]^{2-}$ by Rao et al.⁸⁹ The peak at around 341 m/z correspond to a larger complex

formed between (~249 m/z) and (~93 m/z). The speculated reactions during the

Zn dissolution is shown below:



Besides Zn metal, Cu, Sn, and In metals are also soluble in the solvent mixture of primary amine and 1,2-ethanedithiol (Figure 4.1c). Solubility limits of Cu, Zn, Sn, and In in BA-EDT (vol. ratio 1:1) at room temperature are around 0.5, 0.78, 0.3, and 0.3 M, respectively.

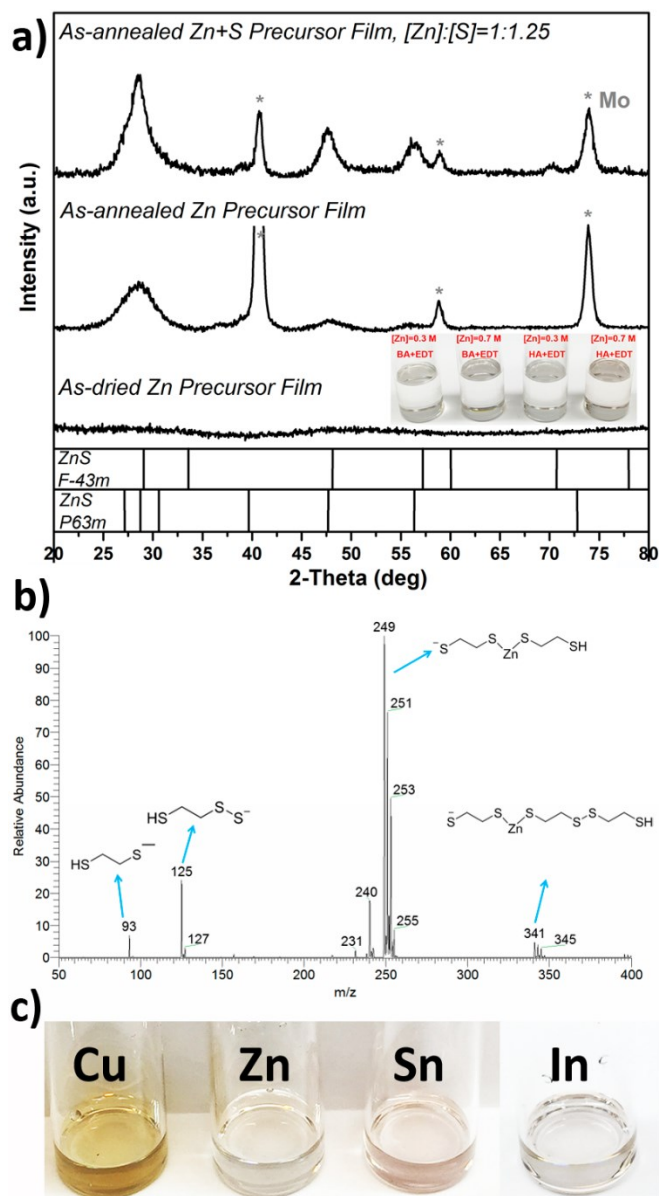


Figure 4.1: a) GIXRD patterns of the as-dried Zn precursor film, the as-annealed Zn precursor film, and the as-annealed Zn+S precursor film. b) ESI negative mode analysis of Zn solution. (Courtesy by Laurance Cain and Priya Murria at Purdue University) The insets are Zn solutions (0.3 and 0.7 M) prepared in BA-EDT and HA-EDT solvent mixtures (vol. ratio as 1:1). c) Saturated solutions of Cu, Zn, Sn, and In in HA-EDT solvent mixtures.

4.3.2 Dissolution and Deposition of Metal Chalcogenides

The use of dithiol in a primary amine-thiol solvent mixture enables the facile dissolution of a series of important metal chalcogenides. Figure 4.2 shows the solutions prepared after dissolving Cu_2S , CuS , SnS , SnSe , Cu_2Se , and CuSe in HA-EDT (vol. ratio of 1:1). The concentration of above solutions are 0.3 M. When either HA or EDT alone was added into the glass vials, the solvents and powders stayed unchanged no matter how long the suspensions were stirred. As soon as EDT was added to HA, dissolution occurred and vice versa. The solubilities of these metal chalcogenides in this particular solvent mixture range from 0.3 to 0.5 M at room temperature. In general, copper chalcogenides have higher solubilities than tin chalcogenides. From the dissolution rate perspective, copper chalcogenides dissolve faster than tin chalcogenides, and sulfides dissolve faster than selenides, when the same concentrations are prepared. All the solutions stay optically transparent over months after fully dissolution, indicating the formation of stable organometallic complexes. Moreover, the dissolution is scalable. Large quantities of these chalcogenide solutions can be prepared and stored at room temperature. Although the dissolution experiment was first performed inside the nitrogen-filled glovebox, it was demonstrated that most of above bulk powders can be dissolved in BA/HA-EDT in air atmosphere (Figure 2.11 and Table 4.3 in Supporting Information).

Re-deposition of metal chalcogenides thin films enables the rapid fabrication of many thin-film devices. Herein, we show the dissolution and re-deposition of CuS and SnS as examples. The pure solutions were spin coated on Mo substrates, followed by an annealing procedure for 10 min in N_2 atmosphere. This whole process was repeated until the desired film thickness was obtained. The phase/s and compositions of the resulting thin films varied with annealing temperatures. Figure 4.3a shows the GIXRD patterns of thin films deposited from a CuS solution (0.3 M) annealed at 150, 300, and 350°C. Several strong peaks at lower two-theta angles were detected from thin films annealed at 150°C, indicating the possible formation of organometallic compounds with long range orders. When the film was annealed at 300°C, all the XRD peaks matched the CuS standard pattern

(space group $P6_3/mmc$, JCPDS 06-0464). In Figure 4.3b, the Raman shifts acquired on this film exhibit peaks at 266 cm^{-1} and 474 cm^{-1} corresponding to the covellite CuS reported by Sukarova *et al.*⁹⁰ Higher temperature annealing at 350°C led to the formation of $\text{Cu}_{1.8}\text{S}$ from the film of CuS, indicating the annealing temperature is critical to the formation of a desired phase. In the case of SnS recovery, orthorhombic SnS was obtained after annealing at 300°C rather than annealing at 150°C (Figure 4.3c), and the thermogravimetric analysis (TGA) shows an end point of phase transformation at 300°C (Figure 4.12). The GIXRD pattern of the film annealed at 300°C matched Herzenbergite SnS (space group $Pnma$, JCPDS 39-0354). In Figure 4.3d, the peaks at 83, 95, 163, 191, and 219, 288 cm^{-1} match well with those of a single crystal SnS reported at 85, 95, 164, 192, 218, and 290 cm^{-1} .⁹¹ The above examples illustrated that using efficient deposition technique and well-controlled annealing, metal chalcogenides can be re-deposited into thin films from the precursor solutions.

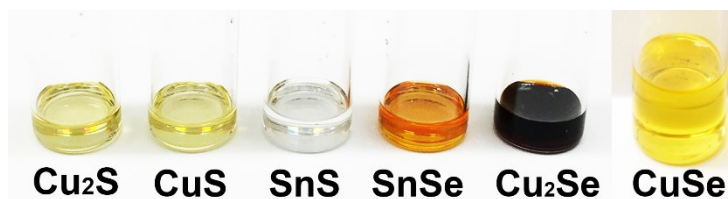


Figure 4.2: Solutions prepared by dissolving Cu_2S , CuS , SnS , SnSe , Cu_2Se , and CuSe in HA-EDT solvent mixtures with concentrations of 0.3 M at room temperature. The dissolution was performed in a N_2 -filled glovebox with both water and oxygen level <0.1 ppm.

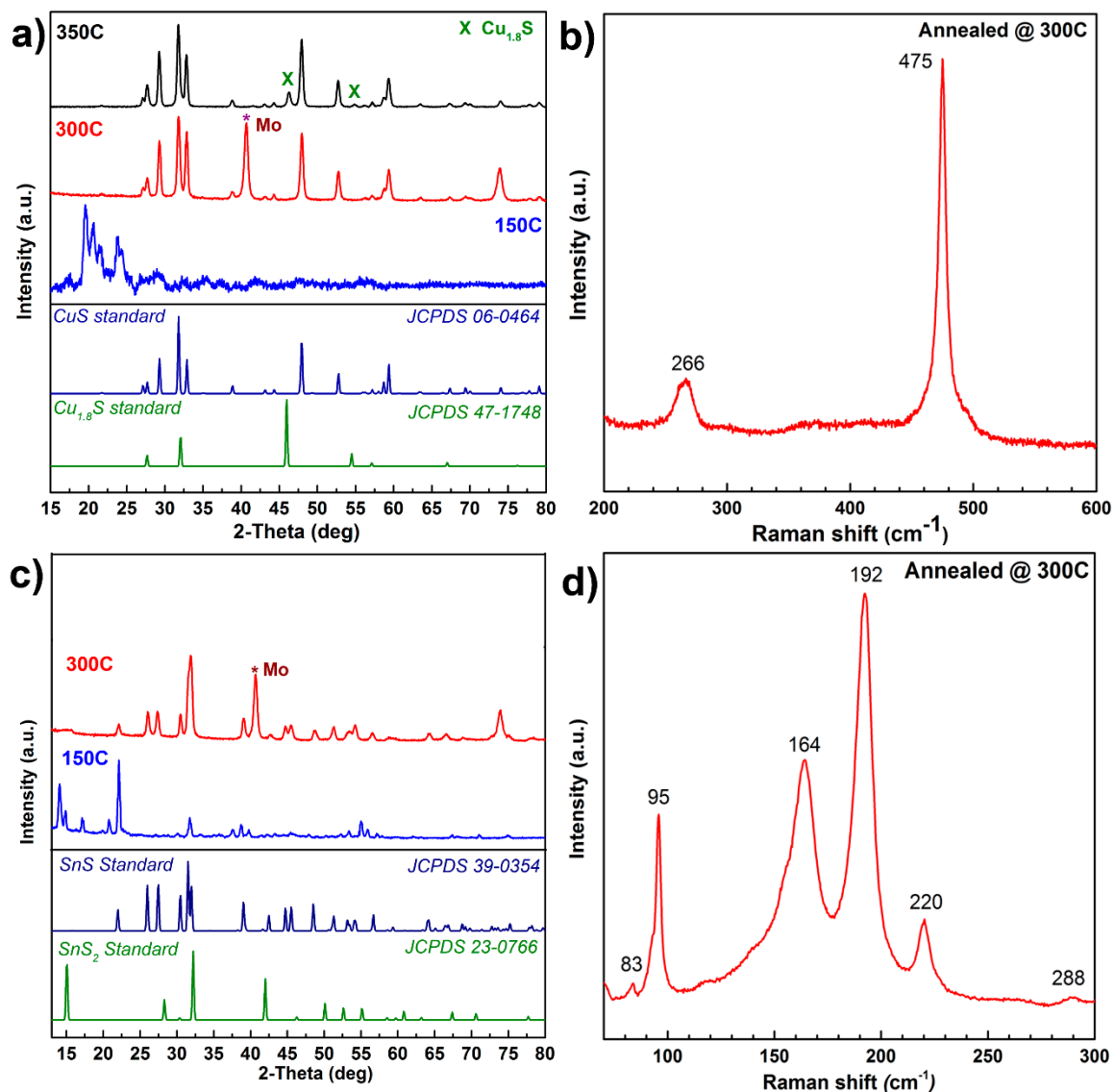


Figure 4.3: a) GIXRD patterns of CuS precursor films annealed at 150°C, 300°C, and 350°C, respectively. b) Raman spectrum of a CuS thin film recovered at 300°C. c) GIXRD patterns of SnS precursor films annealed at 150°C and 300°C, respectively. d) Raman spectrum of a SnS thin film recovered at 300°C.

4.3.3 Deposition of CZTS and CZTSSe Thin Films

Since this primary amine-dithiol solvent mixture can readily dissolve bulk metals and metal chalcogenides at significant high concentrations and form stable solutions, it offers a universal pathway to design molecular precursors for the deposition of specific metal chalcogenides,

especially for ternary and quaternary materials. In the process of preparing precursors, individual metal/chalcogen sources were firstly dissolved separately. The component solutions include Cu or Cu chalcogenide solutions, Sn or Sn chalcogenide solutions, Zn solution, and chalcogen (S/Se/S+Se) solutions. After mixing the above component solutions with appropriate volume ratios, clear and stable molecular precursors are ready for use. To make precursors for ternary $\text{Cu}_2\text{Sn}(\text{S}_x\text{Se}_{1-x})_3$ ($0 \leq x \leq 1$), solutions of $\text{Cu}_2\text{S}/\text{Cu}_2\text{Se}$, SnS/SnSe , and S/Se are mixed with proper ratios. By adjusting S:Se ratio in the precursor solution, ternary sulfoselenide $\text{Cu}_2\text{Sn}(\text{S}_x\text{Se}_{1-x})_3$ ($0 \leq x \leq 1$) with different bandgaps can be deposited. The XRD patterns and film morphology of ternary $\text{Cu}_2\text{Sn}(\text{S}_x\text{Se}_{1-x})_3$ ($0 \leq x \leq 1$) are shown in Figure 4.4.

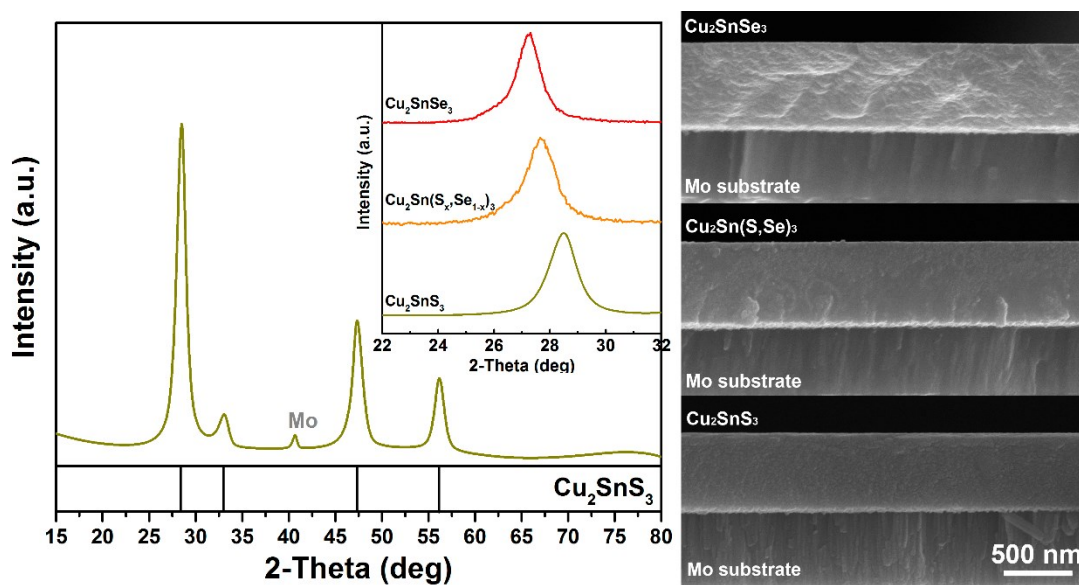


Figure 4.4: GIXRD patterns and film morphology of ternary $\text{Cu}_2\text{Sn}(\text{S}_x\text{Se}_{1-x})_3$ ($0 \leq x \leq 1$) thin films processed using mixture solutions of $\text{Cu}_2\text{S}/\text{Cu}_2\text{Se}$, SnS/SnSe , and S/Se . The compositions of the thin films are estimated using SEM-EDX. The standard pattern of Cu_2SnS_3 (PDF 01-070-6338) is labeled at the bottom. Based on Vegard's law, $x=0.35$ in the $\text{Cu}_2\text{Sn}(\text{S}_x\text{Se}_{1-x})_3$ thin film.

In order to process compositional uniform $\text{Cu}_2\text{SnZn}(\text{S}_x\text{Se}_{1-x})_4$ ($0 \leq x \leq 1$) thin films, three types of precursor solutions have been explored in this study, that is, *Solution 1*: CZTS precursor, a mixture

of Cu_2S , SnS , and Zn solutions; *Solution 2*: CZTSSe precursor, a mixture of Cu_2Se , SnSe , Zn , S , and Se solutions; and *Solution 3*: CZTSSe precursor, a mixture of Cu , Sn , Zn , S , and Se solutions. Figure 4.5 shows the constituent solutions and the as-prepared CZTS and CZTSSe precursor solutions. This solvent system offers a huge flexibility to adjust the concentration ratios between cations (e.g. Cu/Sn and Zn/Sn) and ratios of cation to anion (e.g. $\text{S}+\text{Se}/\text{Sn}$).

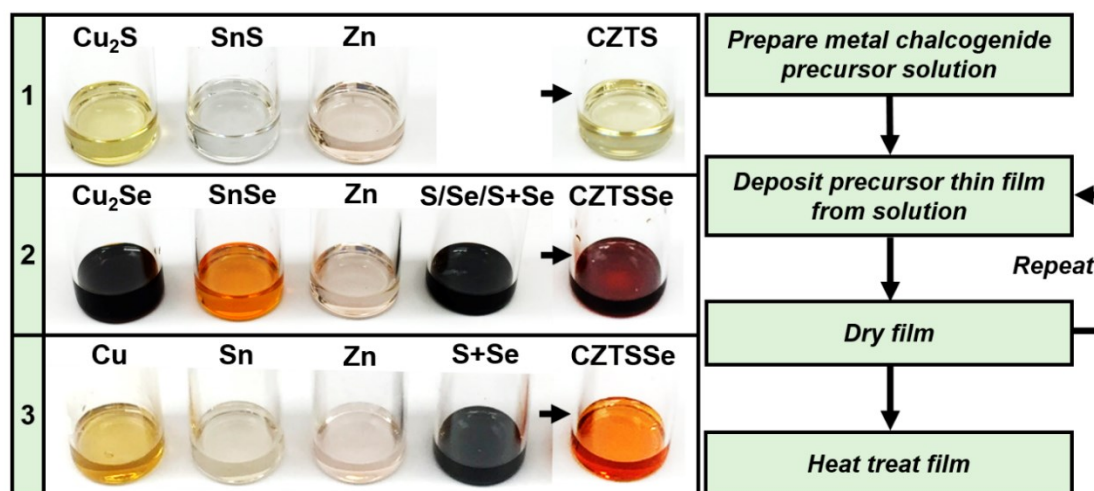


Figure 4.5: Constituent solutions and resulting precursor solutions in three example solution routes to pure CZTS or CZTSSe (left). Schematic of general deposition procedures using the above precursor solutions (right).

The CZTS precursor film was obtained after spin coating and annealing *Solution 1* at 300°C for 5 min for each layer. The top-view and cross-sectional SEM images of a precursor film are shown in Figure 4.6a and c. The annealed precursor film is flat and smooth in a large area. The total thickness of this precursor is around 800 nm for 8-layer coating, with each precursor layer densely packed onto the Mo substrate. The GIXRD and Raman spectrum in Figure 4.6e and f reveal that the precursor film consists of kesterite CZTS nanoparticles. The formation of kesterite CZTS phase at this low temperature is attributed to the low formation energy of this quaternary phase and the compositional homogeneity inside the precursor film. After selenization at 500°C for 40 min, large

grains grow from the precursor films and the grains pack in a layered structure (Figure 4.6b and d). As shown in Figure 4.6e, the sharp peaks in the GIXRD pattern are well-aligned with kesterite CZTSe phase with a slight higher angle shift. In the Raman spectrum (Figure 4.6f), the peak at 174, 196, 235, and 249 cm^{-1} correspond to kesterite CZTSe phase, while the small broaden peak at 331 cm^{-1} is attributed to kesterite CZTS phase.

To fabricate CZTSSe thin-film solar cells, same fabrication procedure for the precursor film and its subsequent selenization were also applied to *Solution 2: CZTSSe precursor solution*. Since Se ions were incorporated in the precursor solution as dissolved selenide and selenium, the phase formed in the precursor film is mainly kesterite CZTSSe, as shown in the GIXRD pattern in Figure 4.7a. In the Raman spectrum (Figure 4.7b), the peaks at 200 cm^{-1} corresponding to the A1 mode of CZTSe has a higher intensity than the peak at 334 cm^{-1} corresponding to the A1 mode of CZTS. This means more Se substitute S in the lattice of precursor film. After the selenization, the precursor film was converted into highly-crystalline CZTSe film. No secondary phases was detected with GIXRD and Raman with excitation wavelength of 633 nm. Solar cells were fabricated based on *Solution 2: CZTSSe precursor solution*. So far, the highest PCE achieved is 6.84% on a total area of 0.47 cm^2 under standard AM 1.5 illumination. Figure 4.7c shows the current density-voltage (J-V) data. The other characteristic parameters of this solar cells are: J_{sc} of 35.5 $\text{mA}\cdot\text{cm}^{-2}$, V_{oc} of 0.36 V, and FF of 53.5%. External quantum efficiency in Figure 4.7d indicates the use of metal chalcogenide precursor solutions improves the carrier collection in the longer wavelength range compared to the use of metal chloride salts in precursor solutions.

The composition and microstructure of the precursor and selenized film were characterized using SEM equipped with EDX (Table 4.2). From the precursor solution with $\text{Zn/Sn}=1.05$, $\text{Cu}/(\text{Zn}+\text{Sn})=0.71$, the final film with ion ratios of $\text{Zn/Sn}=1.18$, $\text{Cu}/(\text{Zn}+\text{Sn})=0.87$ was processed after annealing and selenization treatment.

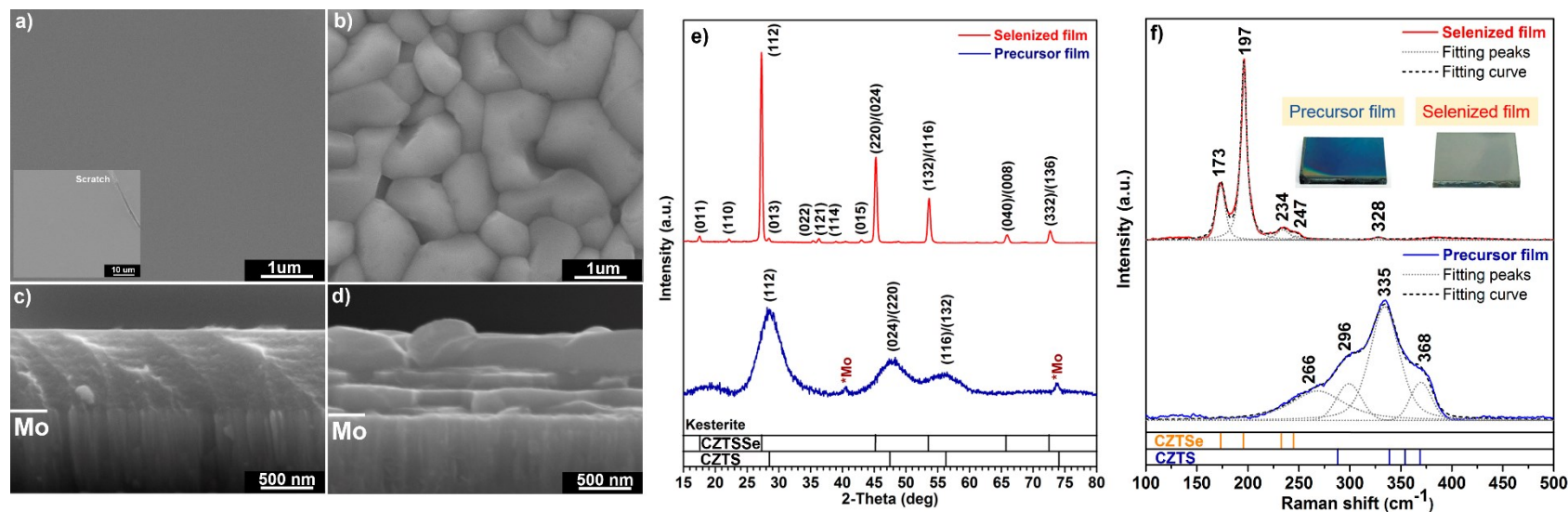


Figure 4.6: SEM images (a-d), GIXRD patterns (e), Raman spectra (f) of a precursor film and a selenized film prepared from *Solution 1*: CZTS precursor solution. a) and c) Top-view and cross-sectional images of a precursor film. b) and d) Top-view and cross-sectional images of a selenized film. Inset in a) is a low-magnification top-view image for the precursor film. A scratch in the upper right corner was intentionally put on to facilitate the focusing in microscope.

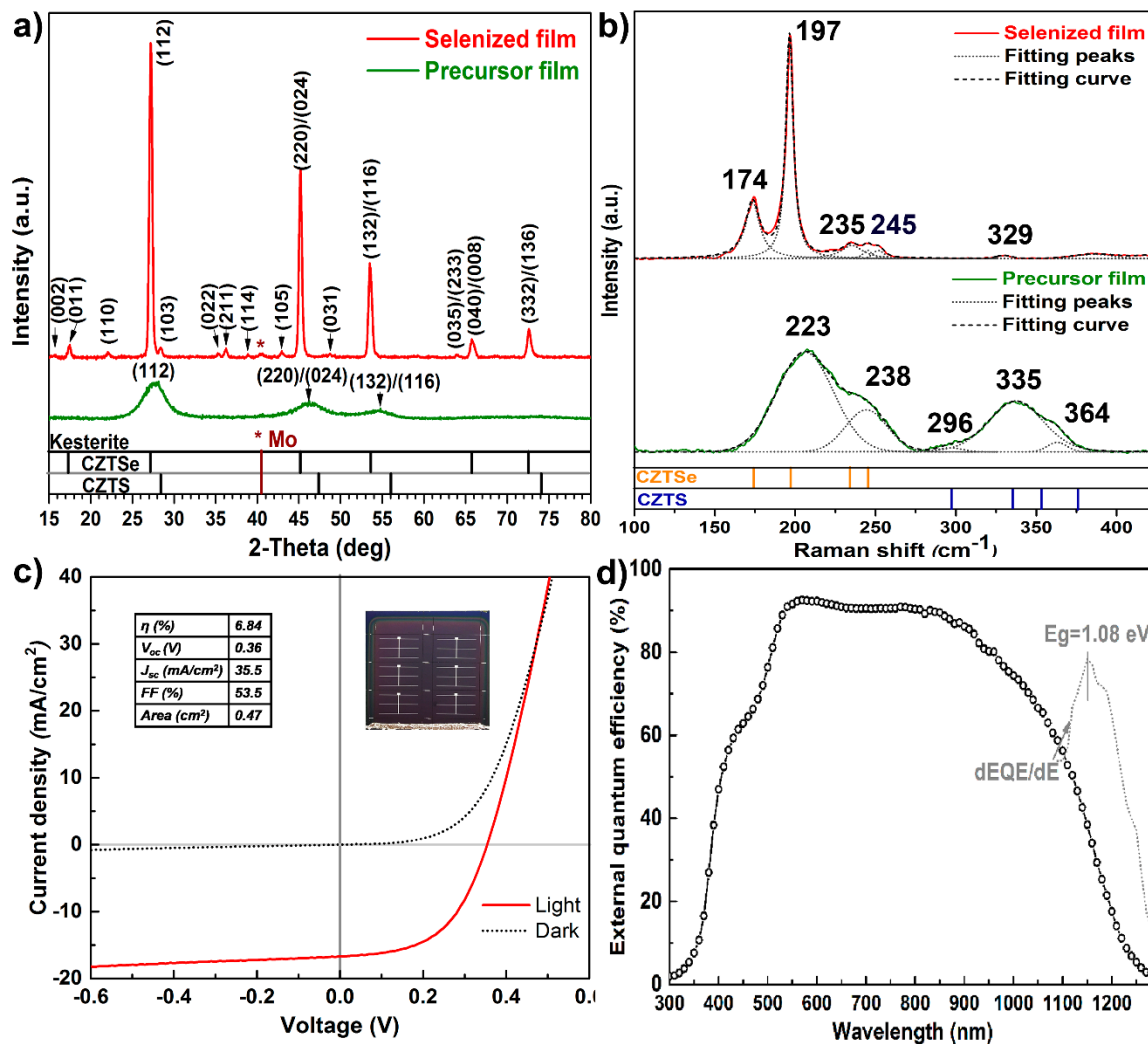


Figure 4.7: Results for *Solution 2*: CZTSSe precursor solution. a) GIXRD patterns of the precursor film and selenized film. b) Raman spectra of the precursor film and selenized film. c) J–V curves and performance parameters for the best performing cell in the dark and under AM1.5 illumination. The dotted line shows the dark current density, while the solid line represents the light current density. d) External quantum efficiency (EQE) of the same cell.

Table 4.2: Average compositions of the precursor solution, precursor film, and selenized film.

Atomic ratio	Solution	Precursor film	Selenized film
[Cu]/[Zn+Sn]	0.71	0.73	0.87
[Zn]/[Sn]	1.05	1.15	1.18
[S]+[Se]/[Sn]	4	3.98	4.12

Figure 4.8 is the high-angle annular dark field (HAADF) images of the precursor film and the elemental distribution within a precursor layer and across the precursor layers. As shown in Figure 4.8a, the precursor film consists of multiple layers which were created during the spin coating. The high and low contrast regions are attributed to the in-situ formed nanoparticles with sizes less than 5 nm (Figure 4.8d) and the low-mass residual solutions. The elemental distribution within a precursor layer and across precursor layers were characterized using EDX installed in STEM (Figure 4.8 b and c). The compositional fluctuation in this precursor film is much smaller compared that in the hydrazine-slurry processed precursor film.⁴⁰ Figure 4.9a and b are the top-view SEM image of the selenized film and cross-sectional SEM images of the solar cell prepared from *Solution 2*: CZTSSe precursor solution. Grains with in-plane diameters more than 500 nm were obtained after the selenization at 500°C for 40 min. In the absorber layer, a fine-grained layer formed underneath the large-grained layer after selenization (Figure 4.9c). The Cu, Zn, Sn, S, and Se uniformly distributed in the large-grained layer, while some fluctuations with Cu and Zn show up in the fine-grained layer (Figure 4.9d). The reason for the formation of fine-grained layer is still unclear. The S:Se ratio in the precursor film might play an important role in changing the grain growth behavior during the selenization as reported in some studies related to CZTSSe colloidal method.^{34,92} It is believed that a continual optimization in the S:Se ratios and the condition of high-temperature heat treatment (e.g. annealing temperature and time) on the precursor films will answer the question, and lead to higher efficiencies.

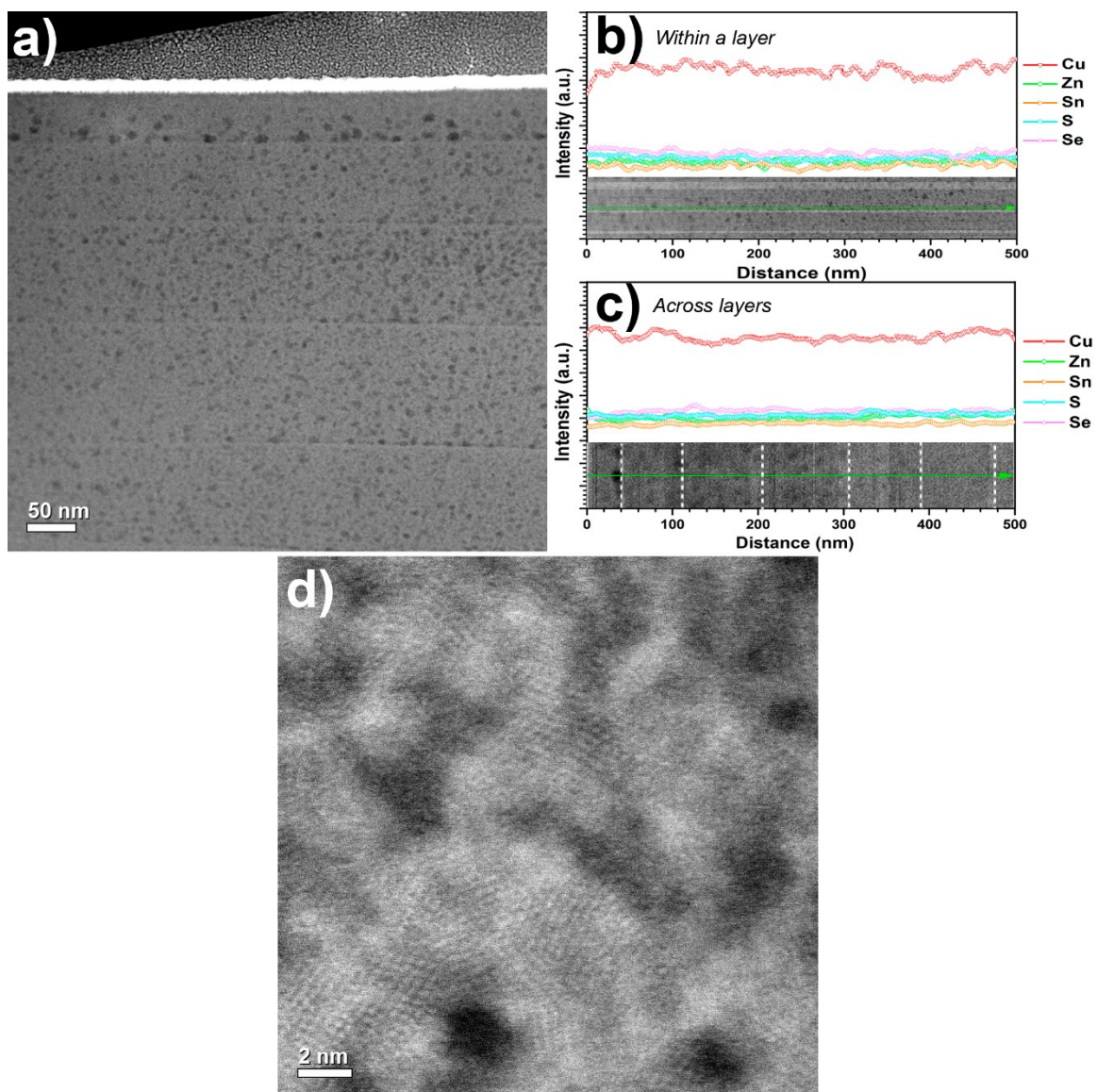


Figure 4.8: Results for *Solution 2*: CZTSSe precursor solution. a) STEM-HAADF images of CZTSSe precursor film. b) and c) Elemental distributions of Cu, Zn, Sn, S, and Se within a single layer of precursor film and across several precursor films. The compositional profiling was analyzed using STEM-EDX. The dot lines mark the layers inside the precursor film. d) High-resolution STEM-HAADF images of nanoparticles in the precursor film.

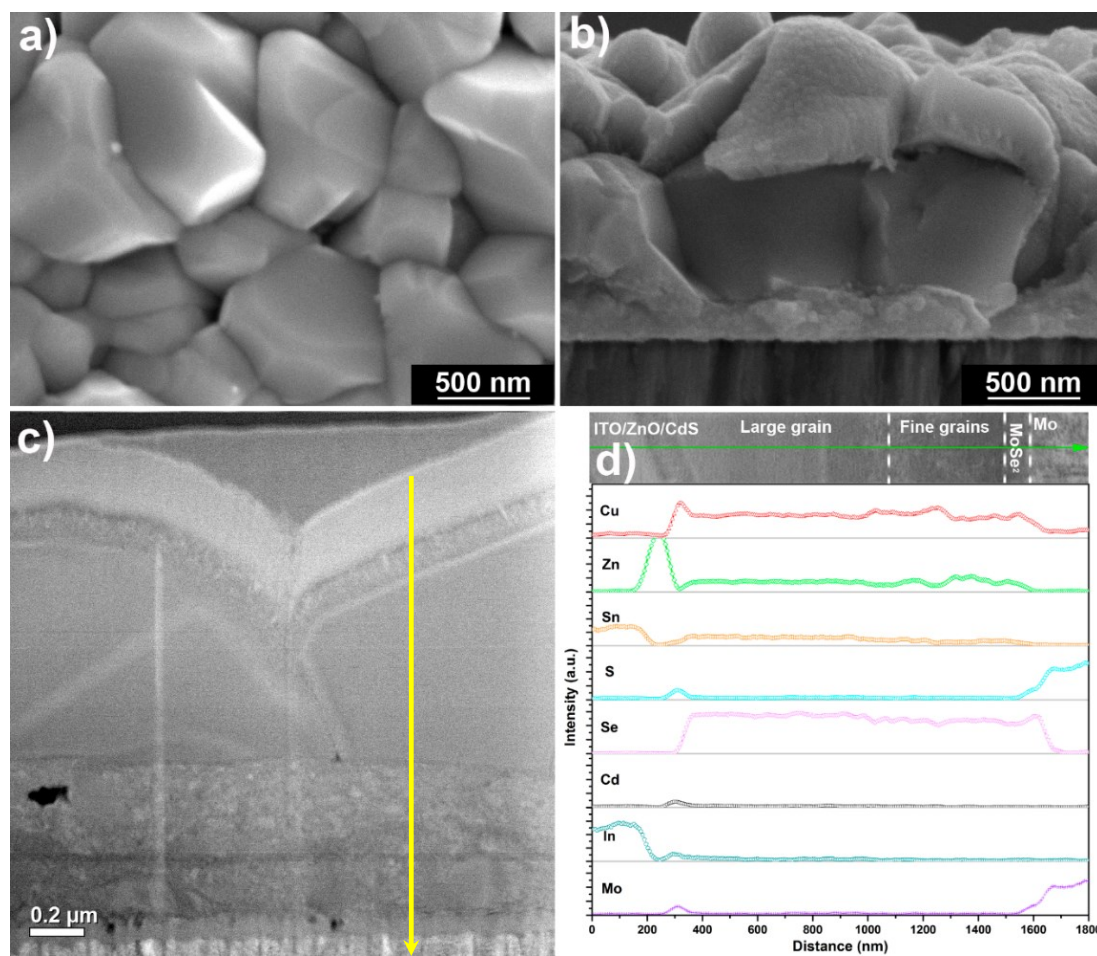


Figure 4.9: Results for Solution 2: CZTSSe precursor solution. a) Top-view SEM image of the selenized film. b) and c) cross-sectional SEM image and STEM-HAADF image of a solar cell. d) STEM-EDX compositional profiling along yellow line in c. Note that S $K\alpha$ and Mo $L\alpha$ overlap each other, thus their compositional profiles are the same.

CZTSSe solar cells were also processed from *Solution 3*, composed of dissolved solutions of Cu, Zn, Sn, S, and Se in HA-EDT solvent mixtures. The solar cell efficiency of 7.02% on an area of 0.483 cm² has been achieved based on this precursor solution (Figure 4.10). Compared to using metal chalcogenide, using bulk metals and chalcogens as the starting materials makes this solution route highly competitive in terms of cost.

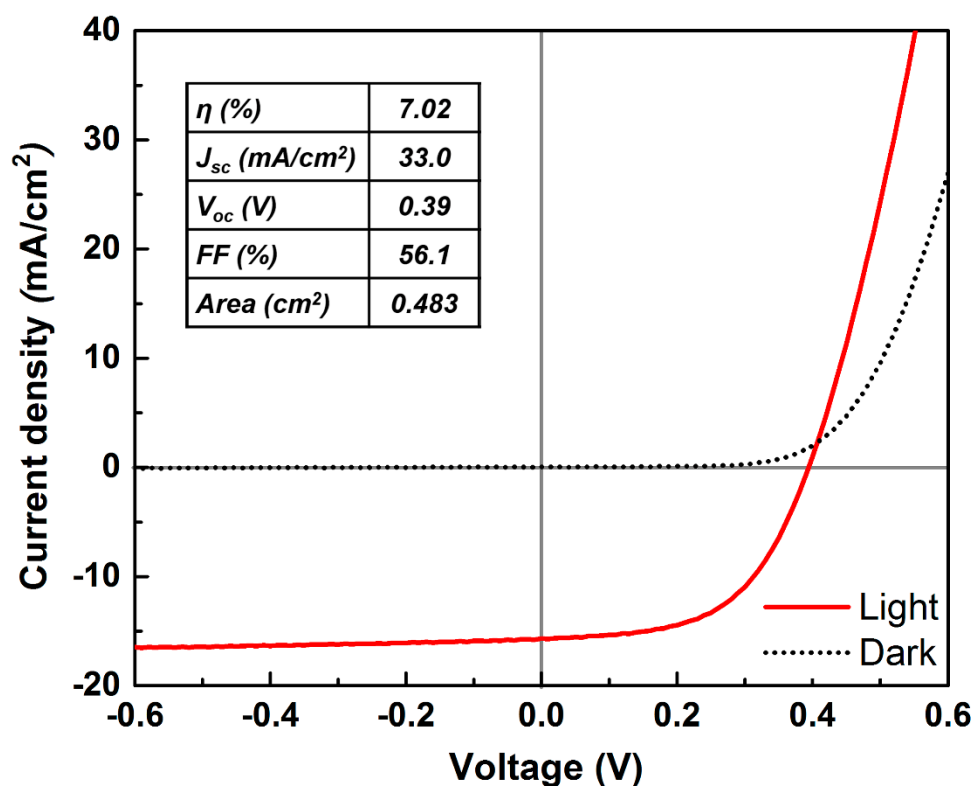


Figure 4.10 J-V curves and performance parameters for the best performing cell processed from *Solution 3*: CZTSS precursor solution. The dotted line shows the dark current density, while the solid line represents the light current density.

4.4 Conclusion

A non-hydrazine primary amine-dithiol solvent system is discovered for fast dissolution of bulk metals (e.g. Cu, Zn, Sn, and In) and metal chalcogenides (e.g. Cu_2S , Cu_2Se , CuS , CuSe , SnS , SnSe , In_2S_3 , In_2Se_3 , Ag_2S , and Ag_2Se). The extensive applications of the metal-metal chalcogenide precursor solutions based on this solvent system is demonstrated by the deposition of CuS , SnS , ZnS , CTSSe , CZTS , and CZTSSe thin films as well as the fabrication of CZTSSe solar cells. The unique capability to dissolve Zn bulk powders at room temperature allows the formation of molecular precursors for CZTSSe deposition, promoting the phase purity and compositional uniformity in the final films. Furthermore, the use of this solvent system offers flexibility in tailoring the stoichiometry of the resulting films simply by adjusting the types and concentrations of component solutions incorporated. The solar cell performances illustrate the potential of this direct solution route for photovoltaic devices and other electronic applications.

4.5 Supporting Information

Table 4.3 summarizes the tested bulk metals and metal chalcogenides, which are soluble in the primary amine-dithiol/monothiol solvent mixtures. The primary-monothiol solvent mixture cannot dissolve those tested bulk metals and metal chalcogenides except zinc powders (solubility ≤ 0.1 M). The primary amine-dithiol solvent mixture can dissolve many metals and metal chalcogenides in both inert and air atmospheres at room temperature (Figure 4.11).

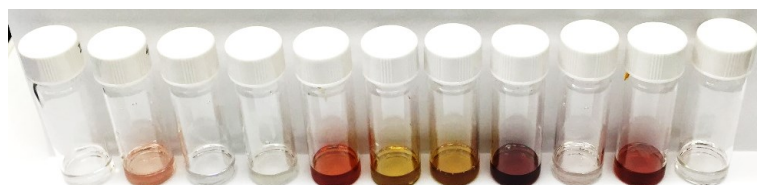


Figure 4.11: Solutions of Zn, Sn, In, SnS, SnSe, CuS, Cu₂S, Cu₂Se, In₂S₃, In₂Se₃, and Ag₂S (left to right) prepared in HA-EDT solvent mixtures at room temperature in air atmosphere. The solution concentrations are 0.2 M.

Table 4.3: Dissolution of metals and metal chalcogenides.

Bulk Material	BA/HA	BA/HA-PT BA/HA-ET	BA/HA-EDT		Color
			Air	N ₂	
Metal					
Cu				√	Clear, dark yellow
Zn		√	√	√	Clear, light pink
Sn			√	√	Clear, pink
In			√	√	Clear, colorless
Metal					
CuS			√	√	Clear, dark yellow
Cu ₂ S			√	√	Clear, dark yellow
CuSe			√	√	Clear, yellow
Cu ₂ Se			√	√	Clear, red
SnS			√	√	Clear, colorless
SnSe			√	√	Clear, orange
In ₂ S ₃			√	√	Clear, light pink
In ₂ Se ₃			√	√	Clear, red
Ag ₂ S			√	√	Clear, colorless
Ag ₂ Se				√	Clear, yellow

BA: butylamine; HA: hexylamine; PT: propanethiol; ET: ethanethiol; EDT:1,2-ethanedithiol

TGA was performed on a TA Instrument Q50 with an alumina crucible under a flowing nitrogen atmosphere. For the measurement, the following heating program was employed: isothermal at room temperature for 20 min, ramp 10°/min to 500°C with a nitrogen flow 60 mL/min. The sample sizes of ~10 mg was analyzed for SnS solution (HA-EDT, 0.3 M). The end temperature of phase transformation is 300°C, corresponding to the annealing temperature used in this study (Figure 4.12).

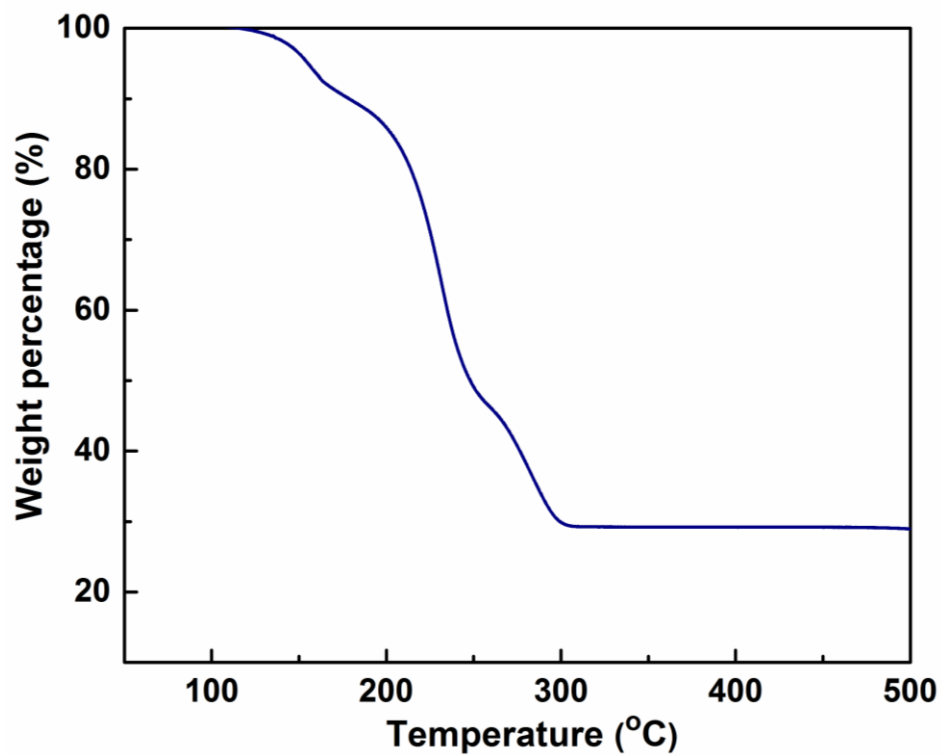


Figure 4.12: TGA trace of SnS solution.

CHAPTER 5. HYDROTHERMAL GROWTH OF ZNO THIN FILMS

5.1 Introduction

Due to its appealing properties, such as a wide bandgap of 3.37 eV, high exciton binding energy of 60 meV, and high single crystal mobility ($100\text{-}230\text{ cm}^2\text{ V}^{-1}\text{ s}^{-1}$),^{93,94} zinc oxide (ZnO) has attracted great attention in applications as diverse as blue/UV optoelectronics,⁹⁵ transparent electronics,⁹⁶⁻⁹⁸ spintronic devices,⁹⁹ sensors,¹⁰⁰ and solar cells.¹⁰¹ For transparent displays in particular, considerable research has been focused on using ZnO thin films as the channel material in transparent thin film transistors (TTFTs) or in the transparent conductive layer. In this application scenario, the formation of continuous films is critical to both carrier transport and optical transparency.

To date, both chemical and physical synthesis methods have been exploited to grow ZnO thin films. Although films with good performance have been synthesized via radio frequency magnetron sputtering,¹⁰² pulsed laser deposition (PLD),¹⁰³⁻¹⁰⁵ molecular beam epitaxy (MBE),¹⁰⁶ chemical vapor deposition (CVD)¹⁰⁷ and other vacuum-based or vapor-phase-based depositions, these methods are not ideal for mass production of ZnO films on flexible polymeric substrates. Either expensive equipment or cumbersome procedures limit their wide technological application. In contrast, aqueous solution growth of ZnO exhibits unique advantages, including ambient pressure, low temperature (less than 95°C), simple chemical processing routes, and low capital costs. For these reasons, we turned our attention to understanding the conditions for aqueous solution growth of continuous and dense ZnO thin films.

Zinc oxide has a hexagonal wurtzite structure with a space group as $P6_3mc$ (Figure 5.1). The structure contains close-packed oxygen and zinc layers stacking along the c -axis with alternating distance of 0.69 Å and 1.99 Å, respectively.¹⁰⁸ The exposed (0001) and (000 $\bar{1}$) planes composed of only Zn^{2+} or O^{2-} ions are polar facets, while $\{10\bar{1}0\}$ planes composed of Zn-O dimers are non-polar facets. This crystallographic anisotropy of ZnO results in anisotropic growth, with the highest growth rate frequently observed along the c -axis, and slower growth normal to the large prismatic facets of $\{10\bar{1}0\}$ and $\{\bar{2}110\}$. This natural tendency normally leads to the growth of needle-like or rod-like ZnO crystals from solution.

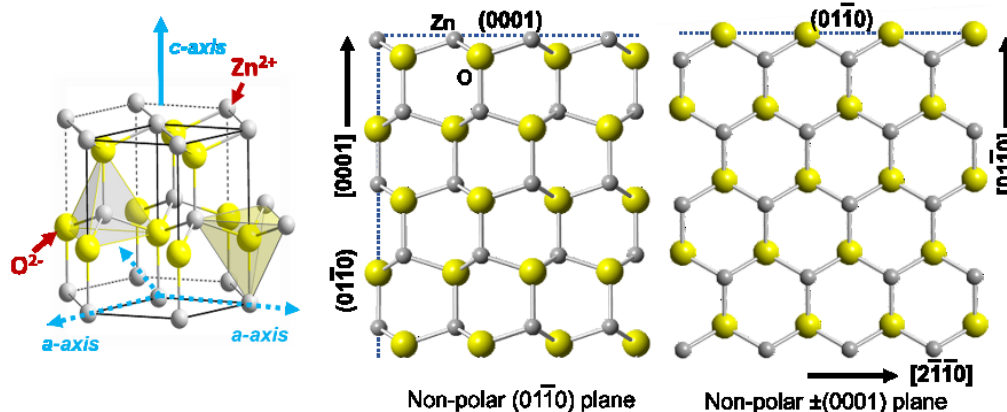


Figure 5.1: Atomic model of 3D wurtzite structure of ZnO crystal (left side) and 2D atomic projections of (01 $\bar{1}$ 0) and {0001} planes (right side). The top and bottom exposed {0001} planes can be either O^{2-} ion-terminated or Zn^{2+} ion-terminated. The 3D and 2D models are constructed in CrystalMaker software.

Since Vayssieres et al. first introduced the hydrothermal growth of arrayed ZnO nanorods/nanowires in 2001,¹⁰⁹ one-dimensional (1D) ZnO nanostructures have been studied widely and the effects of different zinc salts and chelating ligands on the density, aspect ratio, and morphology of ZnO nanorods/nanowires have been systematically examined, with a focus on creating arrays of discrete nanorods/nanowires.¹¹⁰⁻¹¹² Density-controlled ZnO nanorod arrays, for example, have been grown from patterned or unpatterned substrates using an aqueous solution of

zinc nitrate and HMTA.^{113,114} However, hydrothermal growth in terms of two-dimensional (2D) thin film growth was not widely explored, since the goal of the most previous studies was to form arrays of isolated nanorods with high aspect ratios. Consequently, it is advantageous to develop a simple, low-cost, aqueous hydrothermal growth scheme for 2D polycrystalline ZnO thin films with adequate properties for device applications.

In order to grow dense thin films within short time, three strategies are used to either increase the rod density or enhance the lateral growth of nanorods in the thin films: (1) deposition of seed layers from nanoparticle suspensions or precursor solutions, (2) use of capping ions, and (3) adjustment of pH in the aqueous solution. The influence of Cl⁻ capping ions on the anisotropic growth of ZnO nanorods and the effects of seed layers on the resulting films are systematically studied. The utility of these films in TFT applications is demonstrated in terms of microstructure, film thickness, transmittance, and preliminary I-V measurements.

5.2 Experimental Section

5.2.1 Seed Layer Deposition

In order to increase the nucleation sites of ZnO nanorods grown from solution, a seed layer was deposited on the substrates from nanoparticle suspensions or solution precursors.

5.2.1.1 Seed Layers Deposited from Nanoparticle Suspensions

Two zinc oxide nanoparticle suspensions (NanoTek R ZH1121 W and NanoShield R ZN-2000-70 nm from Alfa Aesar), with average particle sizes of 40 nm and 70 nm, respectively, were used to deposit seed layers. In the study of optimizing the growth condition for 2D films, a multilayer of seeds was deposited using the 70 nm-particle suspension. The thickness of the seed layer was around 1 μm . Once the optimum solution chemistry was developed, a suspension with 40 nm-

nanoparticles was used to deposit a monolayer of seeds. This monolayer of seed was also used in fabrication of TFTs.

Glass (0215 Corning glass slides) and oxidized Si wafers (300 nm SiO₂/p⁺⁺ Si wafers) were used as the substrates for ZnO nanorods. Glass substrates were used when optimizing the solution condition for the lateral growth of ZnO nanorods, while the Si wafers were used for the final device fabrication. Since both glass substrates and Si wafers are composed of or covered by amorphous SiO₂ (>70 at. %), the change of the substrates did not influence the formation of seed layers.

All substrates were cleaned with a sequence of rinses: acetone, 2-propanol, piranha solution (H₂SO₄, 98 vol.%: H₂O₂, 30 vol.% = 3:1), and DI water. A two-step spin coating process (step 1: 2000 rpm s⁻¹, 35 s; step 2: 4000 rpm s⁻¹, 10 s) was performed for the seed deposition. Once dried, the freshly coated substrates were annealed in air at 95°C for 2 h to remove the residual solvent.

5.2.1.2 Seed Layers Deposited from Solution Precursors

Zinc acetate solutions (0.25 M) were prepared by dissolving zinc acetate dihydrate Zn(CH₃COO)₂·2H₂O in a mixture of ethanol and diethanolamine. The diethanolamine was added drop by drop into the solution until the zinc acetate crystals were fully dissolved. The total volume added was about 9.5 μL/ml. The precursor solution was colorless after preparation. This solution was spin coated on p⁺⁺ Si wafers covered with 300 nm-SiO₂. The as-deposited precursor films were heat treated at 300 °C for 1 min. Then, the films were annealed inside a tube furnace at 350°C and 600°C for 30 min. The average size of the grains was controlled by the heating temperature.

5.2.1.3 Seed Layer Deposited by PLD

A textured seed layer of ZnO was deposited using pulsed laser deposition (PLD). The film was deposited using PLD (PVD Products, Inc) with a KrF excimer laser (Lambda Physik GmbH) at a wavelength of 248 nm. The ZnO target was purchased from Kurt J. Lesker Corp. with a purity of

99.99%. The substrate was heated to temperature about 50 to 100°C during deposition. The final thickness of the ZnO seed layer deposited was ~50 nm.

5.2.2 Solution Growth of ZnO Thin Films

An aqueous solution of 0.05 M zinc nitrate ($\text{Zn}(\text{NO}_3)_2$) and 0.05 M hexamethylenetetramine (HMTA) was used as the basis for all hydrothermal growth experiments. The influence of Cl^- ions was examined by adding different amounts of potassium chloride (KCl), and thus resulting in the $[\text{Cl}^-]/[\text{Zn}^{2+}]$ ratios within the range of 0~2. The initial pH of the solution was intentionally adjusted by adding glacial acetic acid (CH_3COOH , pH=2.4 at 20°C) or ammonium hydroxide ($\text{NH}_3\cdot\text{H}_2\text{O}$, pH=11.7 at 20°C) to the solution.

Before starting the reaction, annealed substrates were inverted in the container with the aid of a polypropylene holder (Figure 5.2). This configuration could effectively prevent the ZnO crystallites inside the bulk solution from depositing on the thin film. The reaction was initiated by mixing zinc nitrate (50 ml) and HMTA (50 ml) aqueous solutions at 90°C. The mixed solution was immersed in an oil bath to maintain 90°C and stirred at 400 rpm throughout the reaction. Since the ramp time of the real temperature within the bulk solution is short compared to the total growth time, it is regarded that the reaction was performed at a constant temperature. After the reaction, the as-fabricated films were rinsed twice in DI water and dried with dry air.

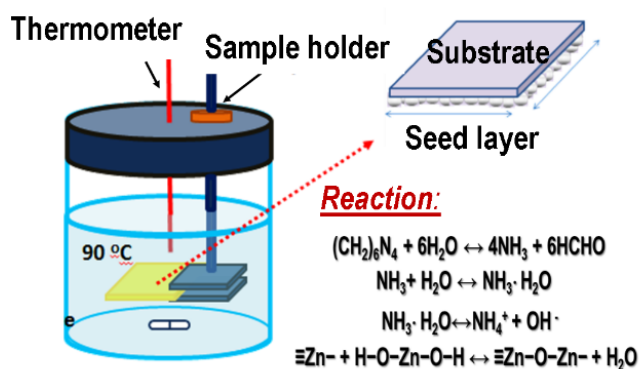


Figure 5.2: Experiment setup for the hydrothermal growth.

5.2.3 Characterization and Measurement

A bottom-gate and top-contact design was used in our ZnO TFTs. The p⁺⁺ silicon was used as the bottom gate and the silicon dioxide layer was used as the dielectric layer ($C=11.5 \text{ nF}\cdot\text{cm}^{-2}$). After the growth of a ZnO thin film on the Si wafer, photolithography was applied to pattern the film and lift-off was performed to define contact regions.

Aluminum source and drain electrodes were deposited via e-beam evaporation. The width of the channel was 50 μm and the length was 10 μm . The I–V characteristics of all transistors were measured in the dark in ambient air using a four-probe station.

The top-view and cross-section microstructures of the ZnO films were characterized using scanning electron microscopy (SEM, Hitachi S-4800 at 10 kV) and SEM/FIB (focused ion beam, FEI Nova 200 NanoLab DualBeam R at 10 kV/5 kV). X-ray diffraction (XRD) was carried out using Cu K_{α} radiation in a Bruker D8 diffractometer. Two parameters, the average diameter of individual nanorods and the rod area density, were introduced and measured using Image J software. Using FIB cross-sections, the fabricated structures were characterized in terms of the four types of layers: the seed layer (SL), the dense layer (DL), the porous layer (PL), and the nanorod layer (NRL). The quality of the fabricated film is represented by RDL, that is, the ratio of DL thickness to NRL (PL+DL) thickness, with RDL=1 being the target film quality. At least five samples were made from each growth condition, and ten regions of $2\times 2 \mu\text{m}^2$ at 20 kx magnification SEM images of each sample were used for measurements. The measurement of film texture was performed using high-resolution x-ray diffraction (XRD, Bruker AXS general area detector diffraction system (GADDS) equipped with a HI-Star area detector). The diffraction geometry can be seen in Figure 5.8a. A section of a Debye–Scherrer ring was studied using a 2D detector system. The detector center was positioned 60 mm away from the illuminated midpoint of the sample. Data correction and processing was performed using the Bruker GADDS software. The resulting Debye–Scherrer rings were converted to multiple line scans as a function of 2θ by integrating with respect to χ in 5°

increments. The series of line scans were processed using MAUD (version 2.33) to generate the inverse pole figures and calculate multiples of random distribution (MRD). The MRD is defined as the ratio of the volume fraction of crystallites of a particular orientation in a measured sample to the volume fraction observed for a powder sample at a specific orientation relative to a direction in the sample reference frame. For this study, MRDs are shown with respect to the film normal direction. A harmonic model for fiber texture was used to fit the integrated line scans in MAUD.

5.3 Results and Discussion

5.3.1 Modification of Anisotropic Growth of ZnO Nanorods

Figure 5.3a and b show SEM top-view images of a typical seed layer prepared from the nanoparticle suspension and of ZnO nanorods grown from it after 10 h reaction. Figure 5.3c shows the normalized XRD patterns of the ZnO seed layer and nanorods after hydrothermal growth. The peak positions for both cases are consistent with the standard powder XRD for ZnO wurtzite phase (JCPDS 79-0206). This indicates that homoepitaxy occurred during the hydrothermal growth. After the hydrothermal growth, the peak of (0002) became the most intense peak, indicating the ZnO crystal has a preferred growth orientation along *c*-axis. A HRTEM image of a nanorod is shown in Figure 5.3d. The elongated direction is along [0001]. The lattice planes with a spacing of 0.26 nm are (0002) planes. Two reasons lead to this anisotropic behavior: i) The polarized {0001} planes have higher surface energies compared to non-polar {0110} planes.¹¹⁵ ii.) During solution growth, Zn²⁺ and OH⁻ ions are easily adsorbed to the polar facets by electrostatic forces, enhancing the anisotropic growth of the crystal along <0001>. Consequently, instead of producing a continuous film, this aqueous solution normally produces ZnO films composed of discrete nanorods.

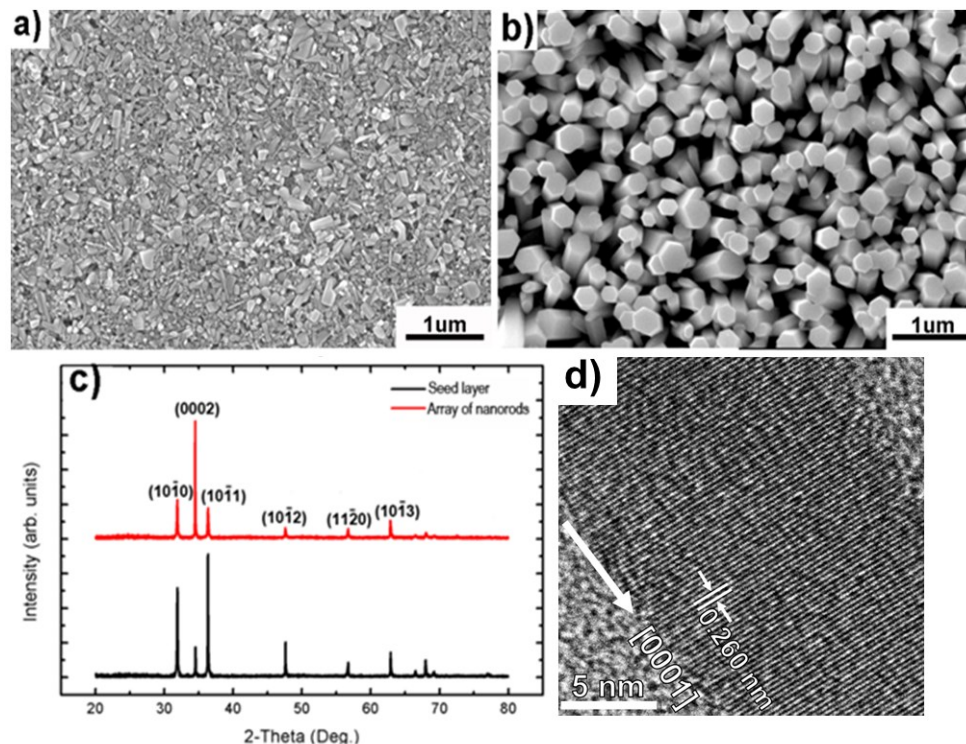


Figure 5.3: SEM images of a) a typical ZnO nanoparticle seed layer fabricated on a glass substrate, and b) the array of nanorods formed from the solution of zinc nitrate and HMTA (1:1, 0.05 M, 10 h hydrothermal growth). c) XRD patterns for the seed layer and the array of nanorods. The black and red patterns represent the seed layer and the array of nanorods after hydrothermal growth, respectively. d) Typical HRTEM image of a ZnO nanorod grown on the seed layer.

5.3.1.1 Modification of ZnO Anisotropic Growth using Chloride Ions

In order to control the anisotropic growth, chloride ions (Cl^-) were introduced into the solution during nanorod growth. Figure 5.4 displays the morphological evolution of ZnO films grown from solutions with and without Cl^- ions. Solutions of zinc nitrate and HMTA with Cl^- ion concentrations of 0.05, 0.075, and 0.1 M, corresponding to the ratios $[\text{Cl}^-]:[\text{Zn}^{2+}]$ of 1, 1.5, and 2, were contrasted with the Cl^- -free solution. The continuity of the film is characterized by the rod area density, defined as the total area of ZnO nanorods per unit area. Two factors contribute to the rod area density, the average diameter of ZnO nanorods and the number density of nanorods. In general, both the average nanorod diameter and rod area density increased with growth time. From the solution containing

only zinc nitrate and HMTA, randomly oriented ZnO nanorods formed after hydrothermal growth and the intercrystal porosity is high. In contrast, films grown from solutions with Cl⁻ additions showed not only larger nanorod diameters, but also higher rod area densities at all growth times (Figures 5.4 c-h and Figure 5.5). For example, after 1 h of growth, the nanorods grown from all three Cl⁻ ion containing solutions exhibited average diameters greater than 100 nm and rod area densities of ~70%, 82%, and 55% were achieved with [Cl⁻]:[Zn²⁺]=1, 1.5, and 2, respectively. The rod area density resulting from the Cl⁻-free solution was only ~23%. After 5 h of growth, ZnO films grown from solutions containing Cl⁻ ions were composed of closely packed, aligned single crystals with few intercrystal channels, and crystal coalescence occurred at several sites, indicated by arrows in Figures 5.4d, f, and h. The average diameters of nanorods in Cl⁻-containing solutions were approximately twice as large as those in Cl⁻-free solutions. Also, the rod area density increased by at least 10% using Cl⁻ ions. The above general phenomena indicated that ZnO growth in $\langle 10\bar{1}0 \rangle$ was promoted by Cl⁻ ion additions.

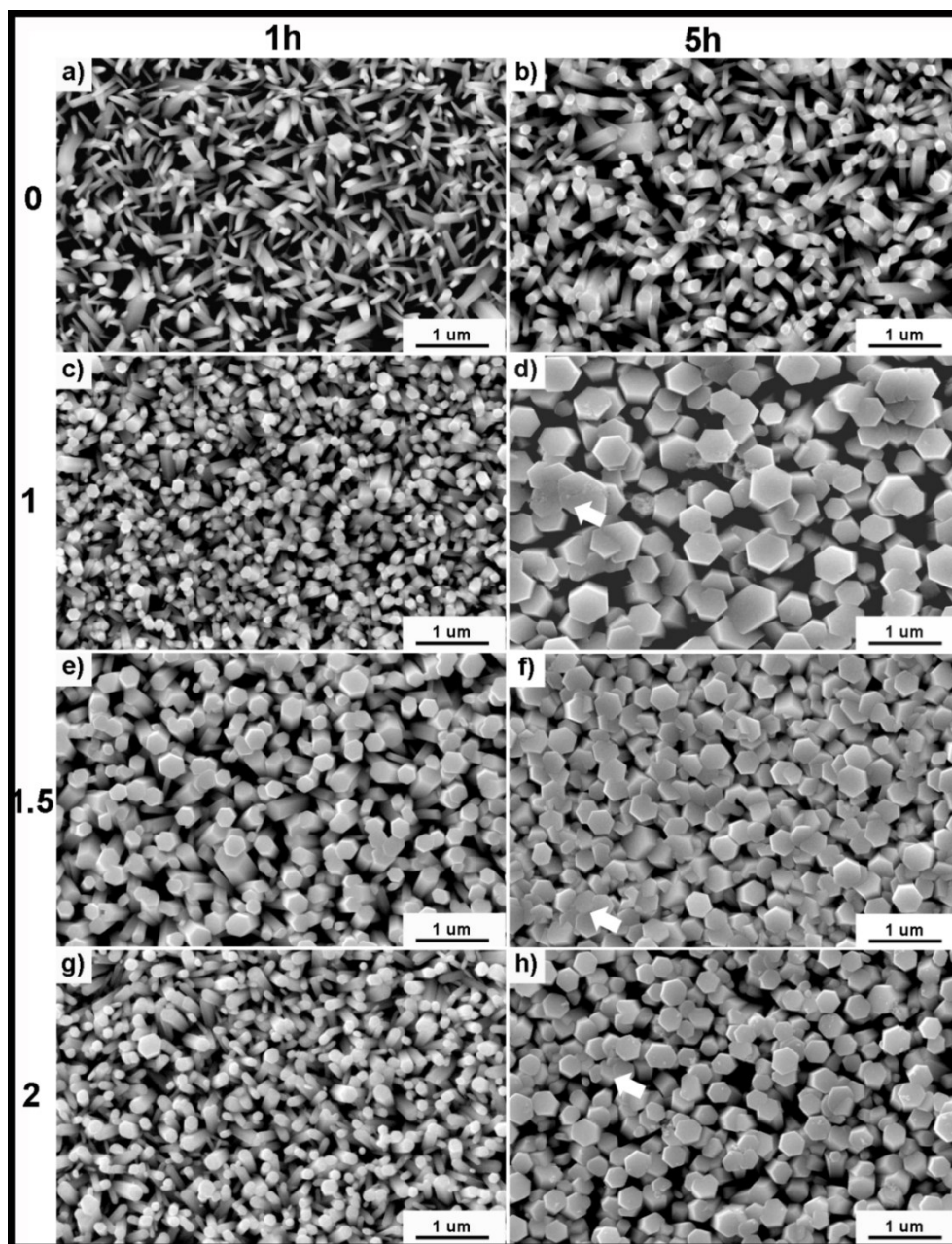


Figure 5.4: SEM images showing the morphology of the ZnO thin films formed on nanoparticle seed layers (glass substrates) from zinc nitrate and HMTA solution with different Cl^- concentrations after 1 h and 5 h growth. a) and b) $[\text{Cl}^-]/[\text{Zn}^{2+}]=0$; c) and d) $[\text{Cl}^-]/[\text{Zn}^{2+}]=1$; e) and f) $[\text{Cl}^-]/[\text{Zn}^{2+}]=1.5$; g) and h) $[\text{Cl}^-]/[\text{Zn}^{2+}]=2$.

By comparing films grown from solutions with different Cl^- concentrations, an optimized process for short-time hydrothermal growth was established. Thin films grown in the solution with $[\text{Cl}^-]:[\text{Zn}^{2+}]=1.5$ showed the highest rod area densities for all growth times (Figures 5.4e, f and Figure 5.5b). In particular, during the first hour of growth, the rod area density reached 80% due to the coalescence of large diameter nanorods. Although solutions with $[\text{Cl}^-]:[\text{Zn}^{2+}]=1$ yields slightly larger average diameters after 5 h growth, solutions with $[\text{Cl}^-]:[\text{Zn}^{2+}]=1.5$ were more effective for short time synthesis of high-density films based on rod area density measurements. When $[\text{Cl}^-]:[\text{Zn}^{2+}]=2$, the average diameter decreased relative to solutions with $[\text{Cl}^-]:[\text{Zn}^{2+}]=1.5$. Furthermore, patches of electron transparent hexagonal plates were found on the top of the films (Figure 5.6). The formation of similar ZnO platelets has been reported previously by Govender et al and Hong et al.^{110,116} These platelets consume the Zn^{2+} ions and quenched the growth of nanorods beneath them, leading to the formation of nanorods with smaller diameters.

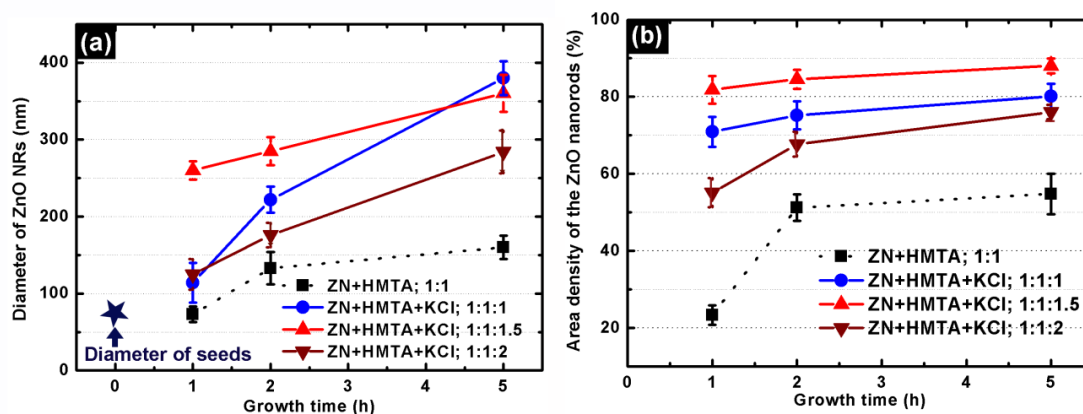


Figure 5.5: Plots of a) average rod diameters and b) rod area density in films formed under different conditions.

Figure 5.7 shows SEM images of FIB cross-sections of the films grown from solution with different $[\text{Cl}^-]/[\text{Zn}^{2+}]$ ratios corresponding to the top views in Figure 5.4. A Pt layer was deposited on the top of the films to minimize beam damage of the film surfaces during milling, and define

the nanorod growth profiles. In Figure 5.7, three distinct layers can be seen in each fabricated structure: a porous seed layer (SL), a dense layer (DL) and a nanorod layer (NRL). The total film thicknesses (DL+NRL) and R_{DL} of the four types of films were $1.57 \pm 0.5 \mu\text{m}$ and $R_{DL} = 0.2$ ($[\text{Cl}^-]/[\text{Zn}^{2+}] = 0$); $1.75 \pm 0.06 \mu\text{m}$ and $R_{DL} = 0.6$ ($[\text{Cl}^-]/[\text{Zn}^{2+}] = 1$), $1.61 \pm 0.05 \mu\text{m}$ and $R_{DL} = 0.7$ ($[\text{Cl}^-]/[\text{Zn}^{2+}] = 1.5$), and $1.04 \pm 0.07 \mu\text{m}$ and $R_{DL} = 0.4$ ($[\text{Cl}^-]/[\text{Zn}^{2+}] = 2$). Solutions with $[\text{Cl}^-]/[\text{Zn}^{2+}] = 1.5$ therefore produced films with the highest R_{DL} .

Texture analysis was performed on films grown for 5 h in solutions of zinc nitrate and HMTA (without Cl^-), and zinc nitrate and HMTA with $[\text{Cl}^-]/[\text{Zn}^{2+}] = 1.5$. The equal area inverse pole figures for the sample normal direction are illustrated in Figure 5.8. Figure 5.8b shows that the MRD of the 0001 pole in ZnO film grown from solution of zinc nitrate and HMTA was 1.5, indicating the absence of a preferred orientation after hydrothermal growth from the randomly oriented seed layer (Figure 5.8b). However, when the Cl^- ions were added to the solution, the resulting film had a MRD of 4.3 along the 0001 pole normal to the sample surface, showing a much stronger preferred orientation. The increase of MRD value, from ~ 1 to 4.3, was correlated with the effects from Cl^- ions. During hydrothermal growth, nanorods oriented perpendicular to the substrate can grow continuously while tilted nanorods gradually impinge into adjacent vertical nanorods. The impingement frequency is determined by the nanorod number density and average diameter. The increase in nanorod diameter associated with Cl^- addition increased the impingement frequency of the tilted and vertical nanorods. The resulting decrease in the tilted nanorod population led to the increased film fiber texture associated with Cl^- addition. Therefore, the addition of Cl^- ions effectively increased the continuity and the texture of ZnO films, and the highest density films were produced with $[\text{Cl}^-]/[\text{Zn}^{2+}] = 1.5$.

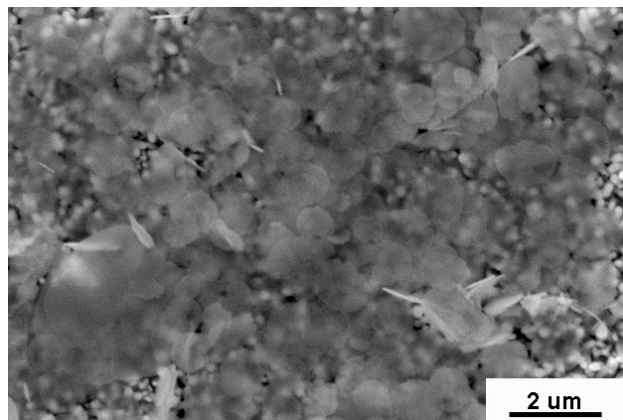


Figure 5.6: Patches of electron transparent hexagonal plates formed on the top of films grown from solution with $[\text{Cl}^-]/[\text{Zn}^{2+}] = 2$. Glass substrate was used.

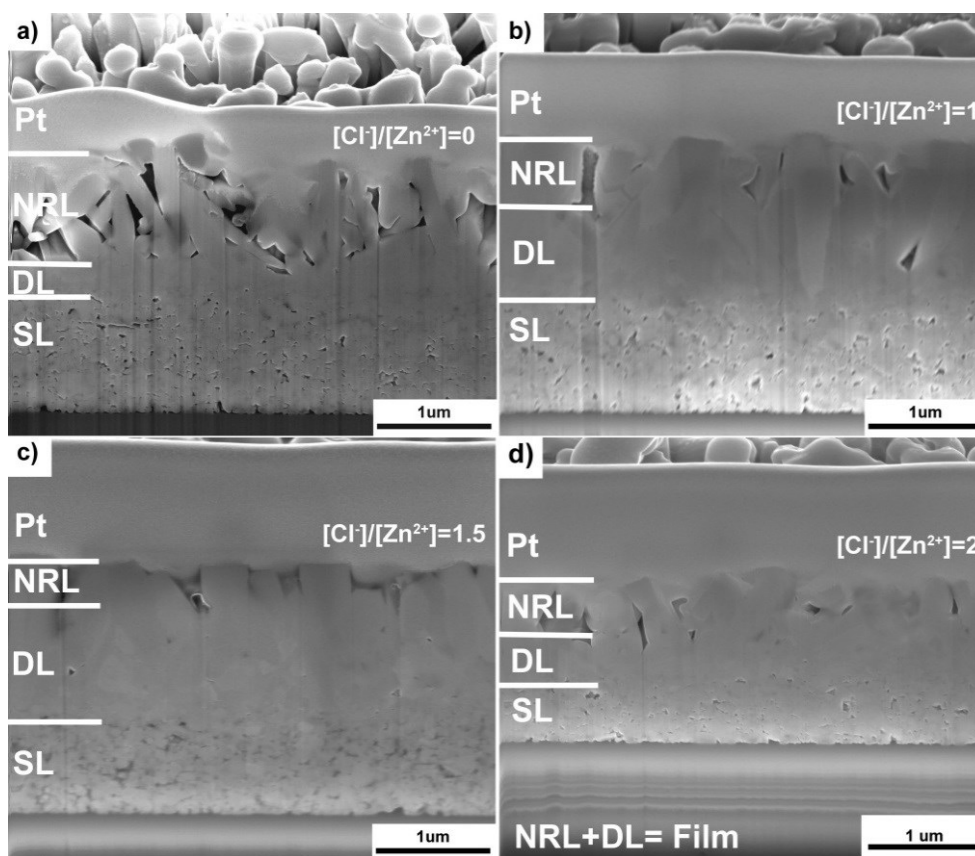


Figure 5.7: Cross-section images of ZnO films grown from the following solution after 5 h. a) $[\text{Cl}^-]/[\text{Zn}^{2+}] = 0$, b) $[\text{Cl}^-]/[\text{Zn}^{2+}] = 1$, c) $[\text{Cl}^-]/[\text{Zn}^{2+}] = 1.5$, and d) $[\text{Cl}^-]/[\text{Zn}^{2+}] = 2$. Pt, NRL, DL, and SL represent ion-beam deposited platinum layer on the top of films, the low density nanorod layer, the dense film layer, and the seed layer, respectively.

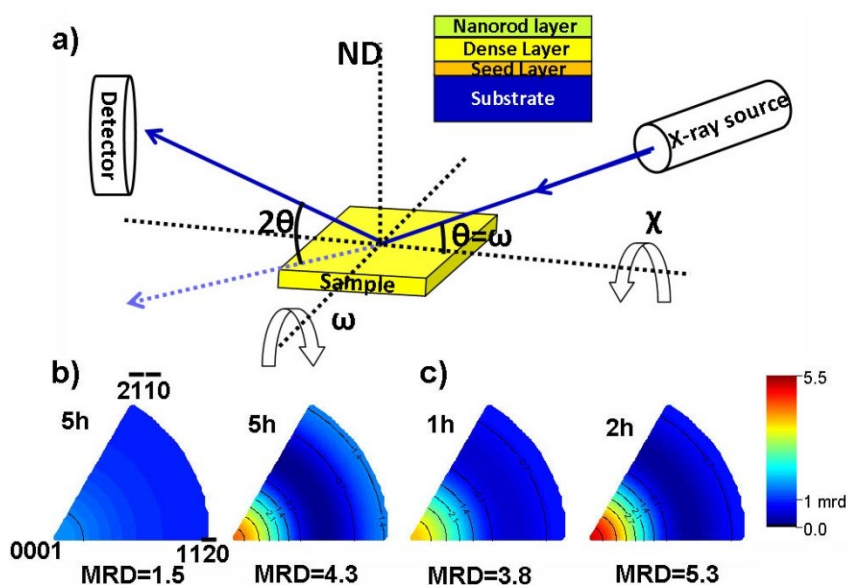


Figure 5.8: a) Schematic illustration of the reflection mode GADDS measurement. Equal area inverse pole figures in sample normal directions of films grown in different solution conditions (left to right): b) film grown from solution of zinc nitrate and HMTA (1:1, 0.05 M), 5 h, and film grown from solution with zinc nitrate and HMTA with $[Cl^-]/[Zn^{2+}] = 1.5$ and $pH = 5.4 \pm 0.1$, 5 h; and c) film growth from solution of zinc nitrate and HMTA with $[Cl^-]/[Zn^{2+}] = 1.5$ and $pH = 4.8 \pm 0.1$, 1 h, and film grown from the same solution for 2 h.

In order to confirm that it is Cl^- ions rather than K^+ ions influence the anisotropic growth of ZnO, we compare the morphologies of films grown from solutions with KCl or NH_4Cl . The films were grown from solutions with $Zn(NO_3)_2$, HMTA, and NH_4Cl ($[Zn^{2+}]: [HMTA]: [Cl^-] = 1:1:1.5$, $pH = 4.8 \pm 0.1$) for 1 h and 2 h. As seen in Figures 5.9a and b, the lateral growth of ZnO nanorods was also enhanced by adding NH_4Cl . Therefore, Cl^- ions should play a dominant role in changing the grain growth of ZnO nanorods.

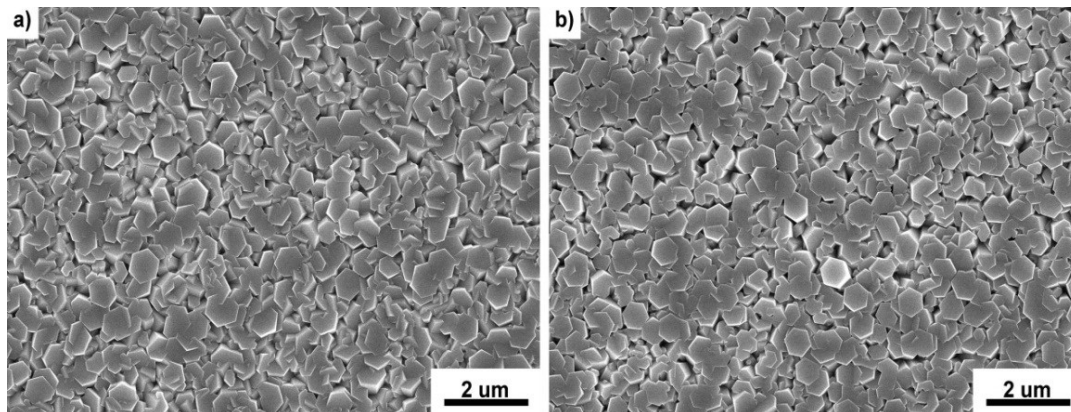
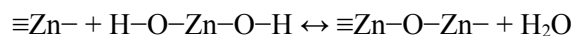


Figure 5.9: SEM images of ZnO films grown on nanoparticle seeds (glass substrates) from solution with $\text{Zn}(\text{NO}_3)_2$, HMTA, and NH_4Cl ($[\text{Zn}^{2+}]: [\text{HMTA}]: [\text{Cl}^-]=1:1:1.5$, $\text{pH}=4.8 \pm 0.1$). (a) 1 h growth and (b) 2 h growth.

Figure 5.10 and Figure 5.11 are XPS results of a ZnO thin film grown from solution of zinc nitrate and HMTA with $[\text{Cl}^-]/[\text{Zn}^{2+}]=1.5$, $\text{pH}=4.8 \pm 0.1$. The in-situ sputtering process helped the measurement of composition and phase changes throughout the sample thickness. As shown in Figure 5.10, the spectra show primarily Zn 2p and O 1s features, along with small C 1s and Cl 2s features on the sample surface. Although the C contamination is a big issue for XPS samples, the amount of C decreased significantly after sputtering. Figure 5.11 shows the Cl 2p, Zn 2p and O 1s peaks at different sputtering time. The O 1s peak can be deconvoluted into two peaks, Zn-O at 530.7 eV and Zn-OH at 532.5 eV. The major peak for all spectra is the Zn-O peak, indicating the major material in the film is ZnO rather than $\text{Zn}(\text{OH})_2$. The existence of Zn-OH peak is reasonable, since $\text{Zn}(\text{OH})_2$ is the precursor that forms ZnO and H_2O . The peak intensity of Zn-O increases and the peak intensity of Zn-OH decreases with the sampling depth, indicating that the conversion from $\text{Zn}(\text{OH})_2$ to ZnO occurred inside the film while it was growing. This also has been confirmed by Nicolas et al.¹¹⁷ The Zn 2p peaks do not change in position and intensity as the sampling depth increases. The intense Zn $2p_{3/2}$ represents the Zn^{2+} divalent state which corresponding to both $\text{Zn}(\text{OH})_2$ and ZnO phases. The intensity did not changed between spectra, indicating that the

amount of Zn(OH)_2 is small relative to ZnO . Otherwise, as reported in study of Pradhan et al., the intensity should change due to the higher mass density of Zn in ZnO compared to that in Zn(OH)_2 .¹¹⁸ The Cl is very small compared to Zn and O in the film, but the Cl 2s feature can be seen through the whole film, as shown in Figure 5.11. The Cl 2p peak consists of Cl 2p_{3/2} and Cl 2p_{1/2} features, with a spin-orbit splitting of ~ 1.6 eV. Due to the low concentration, the peaks are broad. Note that the intensity of Cl peaks is high at the sample surface. The existence of Cl throughout the film thickness and the higher intensity near the surface reveals that the Cl^- ions played an important role in changing the ZnO (0001) planes during the hydrothermal growth. In contrast, no K features can be found in any spectra during the sputtering, although the same amount of K^+ ions as Cl^- ions were added into the solution.

The growth mechanism of ZnO nanorods in solution without and with Cl^- ions is shown schematically in Figure 5.12. The common crystal habits in ZnO include a basal polar oxygen plane (000 $\bar{1}$), a tetrahedron corner-exposed zinc polar plane (0001) and six symmetric nonpolar $\{10\bar{1}0\}$ planes parallel to the c -axis. When the solution of zinc nitrate and HMTA is used, the surface charge of the Zn-terminated plane generates a double layer of $\text{OH}^-/\text{Zn}^{2+}$, and Zn(OH)_2 acts as the precursor for the formation of ZnO by the following reaction:



where $\equiv\text{Zn}^-$ is the Zn atom at Zn-terminated planes and $\text{H}-\text{O}-\text{Zn}-\text{O}-\text{H}$ represents the Zn(OH)_2 .¹¹⁹ Therefore, the growth preferentially occurs on the Zn-terminated (0001) planes.¹²⁰⁻¹²² The growth rates of different crystallographic directions can be described as $\vec{r}[0001] > \vec{r}[01\bar{1}0] > \vec{r}[000\bar{1}]$.^{120,121,123} Furthermore, being a non-polar chelating agent, HMTA preferentially attaches to the non-polar facets of ZnO single crystals.¹²⁴ The nanorods with high aspect ratios are expected to grow under the influence of this selective adsorption effect (Figure 5.12a). Since the seed layer does not exhibit a preferred crystallographic orientation, the resulting nanorods are weakly textured. The intergrowth of oblique nanorods results in the formation of pores in the film.

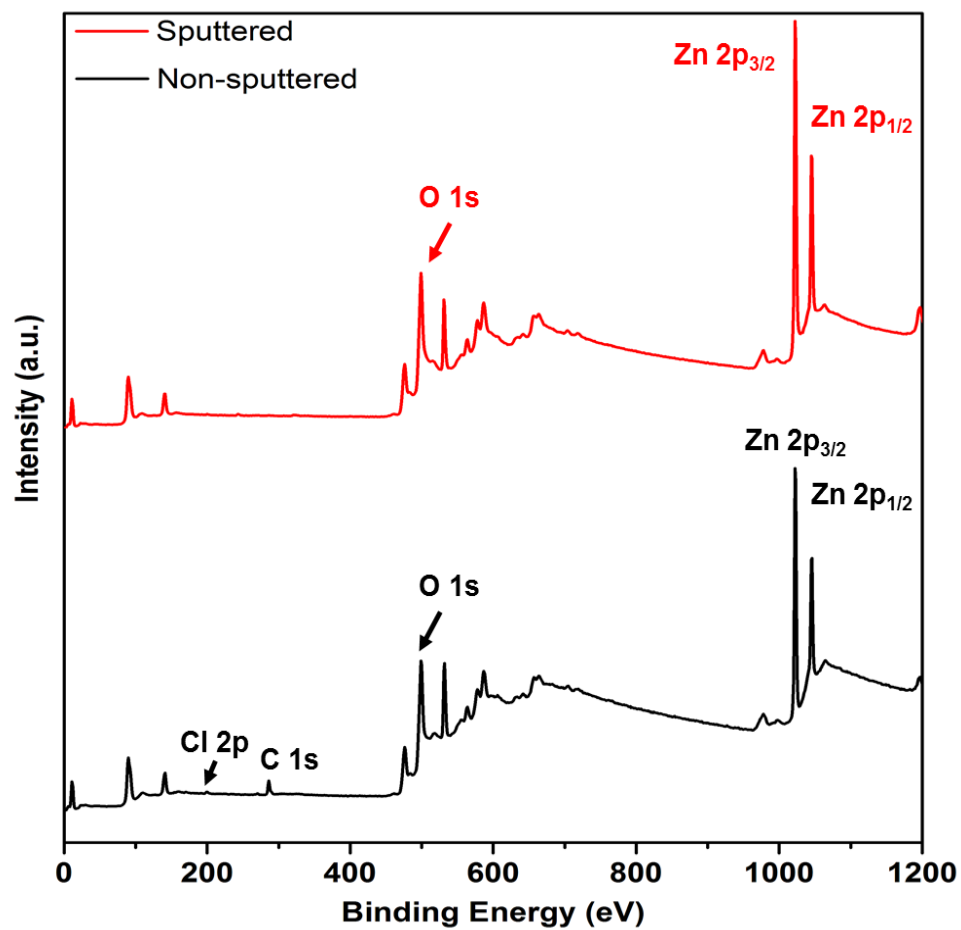


Figure 5.10: XPS full spectra of ZnO thin film surface (without sputtering) and the interior (with ion sputtering). On the sample surface, Cl 2p, C 1s, O 1s, and Zn 2p show up, while inside the sample only O 1s and Zn 2p peaks have significant intensity.

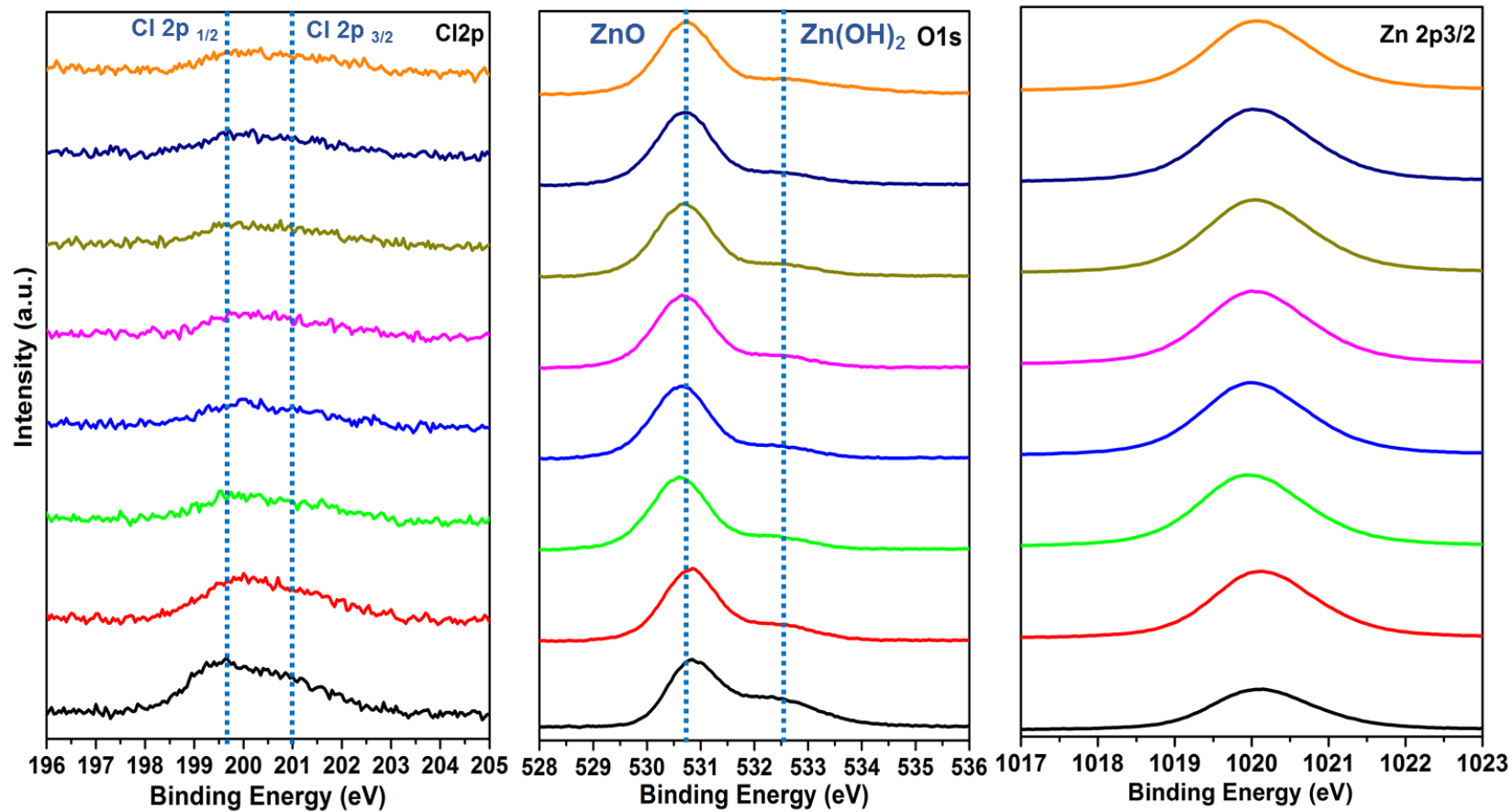


Figure 5.11: XPS spectra of Cl 2p, O1s, and Zn 2p_{3/2}. The ZnO thin film was ion sputtered from the surface to the bottom during the XPS measurement. The spectra going upward from black lines to orange lines were collected with increasing sputtering time. The black lines represent the spectra of the film surface, and the orange lines represent the spectra of the film bottom.

When negatively-charged Cl^- ions are added to the solution, they selectively attach to the Zn-terminated surfaces. The growth rate along the c -axis decreases while growth in $\langle 11\bar{2}0 \rangle$ and $\langle 10\bar{1}0 \rangle$ directions is enhanced (Figure 5.12b). Both the intergrowth of nanorods due to the enhanced lateral growth and the diffusion of ions into intercrystal space lead to the formation of continuous 2D films. The formation of large ZnO platelets is also consistent with the strong adsorption effect of Cl^- ions on the polar facets of single crystals when a high concentration of Cl^- was used ($[\text{Cl}^-]/[\text{Zn}^{2+}]=2$). Studies involving the effects of Cl^- ions on electro-/photochemical deposition of Zn on ZnO also illustrate this proposed mechanism.^{121,125-127} For example, Podlogar et al. stated that the capping effect of Cl^- ions resulted in the formation of ZnO nanowalls using electrochemical deposition.¹²¹ Similarly, Read et al. reported that preferential Cl^- adsorption on the polar planes of ZnO nanorods led to preferential Au particle deposition on the non-polar planes of ZnO during photochemical deposition.¹²⁵

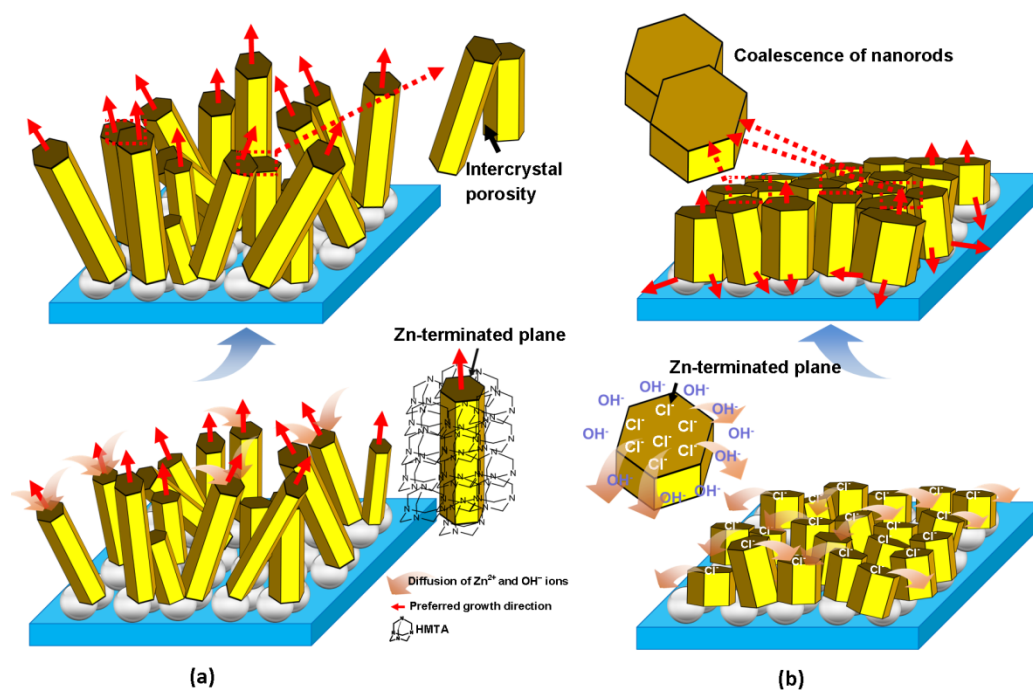


Figure 5.12: Schematic illustration of 2D film growth from solution (a) without and (b) with Cl^- ions. The effect of HMTA was drawn based on an article published by Sugunan et al.¹²⁴

5.3.1.2 Effects of Solution pH on Anisotropic Growth

The pH of a solution can strongly influence the hydrolysis of HMTA. If the selective adsorption effects of HMTA and Cl^- ions are as illustrated above, the competition between these two effects on film growth can be tailored by adjusting the pH of the solution. In this experiment, glacial acetic acid and ammonia hydroxide were used to adjust the pH of the optimized solution with $[\text{Cl}^-]/[\text{Zn}^{2+}]=1.5$ and $\text{pH}=5.4\pm 0.1$ at 90°C . Figure 5.13 shows the morphologies of ZnO thin films formed in the solutions with pH equals to 4.8 ± 0.1 (a-c) and 9.9 ± 0.1 (d-f). At the lower pH, the hexagonal ZnO nanorods showed substantial intergrowth, forming a dense and continuous film after 1 h of growth. The average diameter of the nanorods increased to almost $1 \mu\text{m}$. Compared to the average diameter ($\sim 280 \text{ nm}$) achieved after 1 h of growth with $([\text{Cl}^-]/[\text{Zn}^{2+}]=1.5)$ at the original solution pH of 5.4, the nanorod diameter increased by a factor of three. The R_{DL} of the film (NRL+DL) changed from 0.7 to 1, indicating the formation of a fully dense film with a thickness of $1.7 \mu\text{m}$, as shown in Figure 5.13c. When the initial pH of the solution was adjusted to 9.9 ± 0.1 , high-aspect-ratio nanorods formed (Figure 5.13d-e). After 2 h of growth (Figure 5.13f), the overall density of the fabricated structure was low and there was no dense layer apparent. The fabricated structure consisted only of a porous layer (PL), with a density less than 80%, and a nanorod layer (NRL). Given that it is difficult to distinguish the interface where nanorod growth began from the seed layer, the porous layer contains both the seed layer and the region below the NRL. The R_{DL} equals 0.

The results of pH adjustment strongly support our model of the roles of the HMTA ligand and Cl^- ions on ZnO anisotropic growth. At lower pH, hydrolysis of HMTA is accelerated, and thus the preferred capping effect from Cl^- ions dominates, leading to the formation of larger diameter nanorods and substantial impingement. At higher pH, the selective adsorption of HMTA dominates due to very limited HMTA consumption. Based on the texture analysis of films grown from solutions with $[\text{Cl}^-]/[\text{Zn}^{2+}]=1.5$ and $\text{pH}=4.8\pm 0.1$, the fiber texture was enhanced by lowering the

solution pH. The MRD for the film grown for 2 h at pH= 4.8 ± 0.1 was 5.3, higher than the MRD of the film grown for 5 h from the solution with $[\text{Cl}^-]/[\text{Zn}^{2+}] = 1.5$ and pH= 5.4 ± 0.1 (Figure 5.14b). As mentioned above, the accelerated lateral growth, which increased the average diameter of the nanorods, contributed to the enhanced fiber texture in the film. An optimized solution was obtained in this set of experiments: $[\text{Zn}^{2+}] = 0.05 \text{ M}$, $[\text{Zn}^{2+}]:[\text{HMTA}]:[\text{Cl}^-] = 1:1:1.5$, and initial pH= 4.8 ± 0.1 .

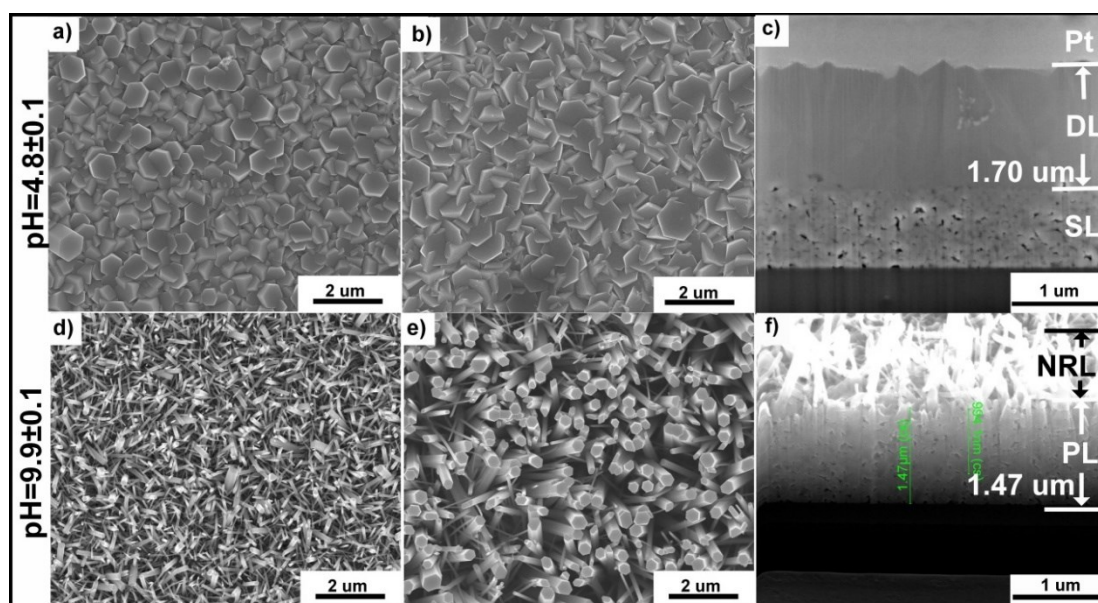


Figure 5.13: SEM images of ZnO film acquired from the solution with $[\text{Cl}^-]/[\text{Zn}^{2+}] = 1.5$ at 90°C . (a-c) pH= 4.8 ± 0.1 , adjusted from 5.4 ± 0.1 , (d-f) pH= 9.9 ± 0.1 , adjusted from 5.4 ± 0.1 . (a, d) for 1 h growth and (b, c, e, and f) for 2 h growth. Films were grown on glass substrates. Pt, DL, PL, and SL represent the ion beam deposited platinum layer, the dense layer, the porous layer, and the seed layer, respectively.

The focused ion beam images exhibit a better contrast for different materials and pores inside the film. The focused ion beam image for the films grown from solution with $[\text{Cl}^-]/[\text{Zn}^{2+}] = 0$ and $[\text{Cl}^-]/[\text{Zn}^{2+}] = 1.5$, pH= 4.8 ± 0.1 are shown in Figure 5.14. It is clear that the film grown from solution with $[\text{Cl}^-]/[\text{Zn}^{2+}] = 0$ is composed of separate nanorods and a very thin dense layer. In contrast, the films grown from solution with $[\text{Cl}^-]/[\text{Zn}^{2+}] = 1.5$, pH= 4.8 ± 0.1 only has a dense layer above the seed layer.

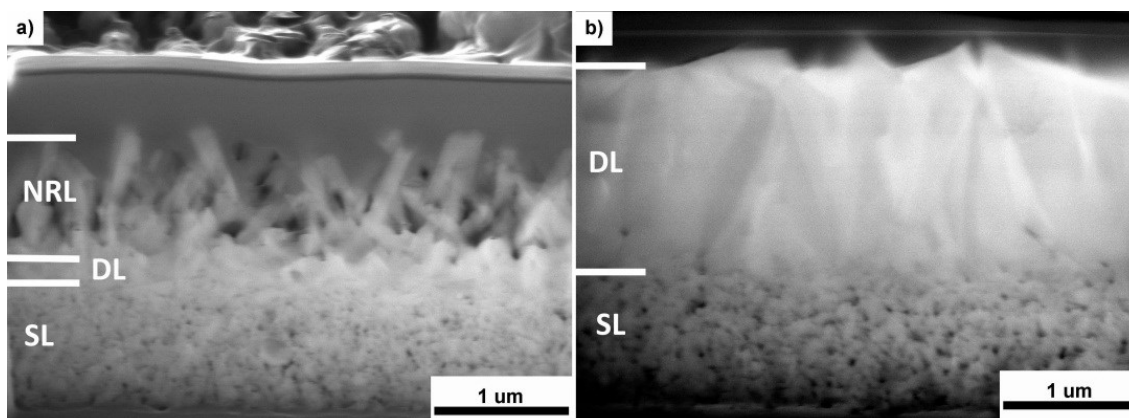


Figure 5.14: Focused ion beam images of ZnO films grown on nanoparticle seed layers (glass substrates) from solution with (a) zinc nitrate and HMTA, $[\text{Cl}^-]/[\text{Zn}^{2+}]=0$ and (b) $[\text{Cl}^-]/[\text{Zn}^{2+}]=1.5$, $\text{pH}=4.8\pm 0.1$. NRL, DL, and SL represent the nanorod layer, the dense layer, and the seed layer, respectively.

5.3.1.3 Device Fabrication

By tuning the anisotropic growth of single ZnO nanorods, continuous ZnO polycrystalline thin films were obtained from short-time hydrothermal growth. To obtain a fully dense thin film for TFT application, a single seed layer of 40 nm nanoparticles was deposited on the p^{++} Si wafer with 300-nm SiO_2 on the top (Figure 5.15a). After 15 min of hydrothermal growth with the optimized solution condition, dense ZnO thin films with a thickness of ~ 100 nm were obtained (Figure 5.15b). These films were fabricated into TFTs for optical and electrical property measurements as described below.

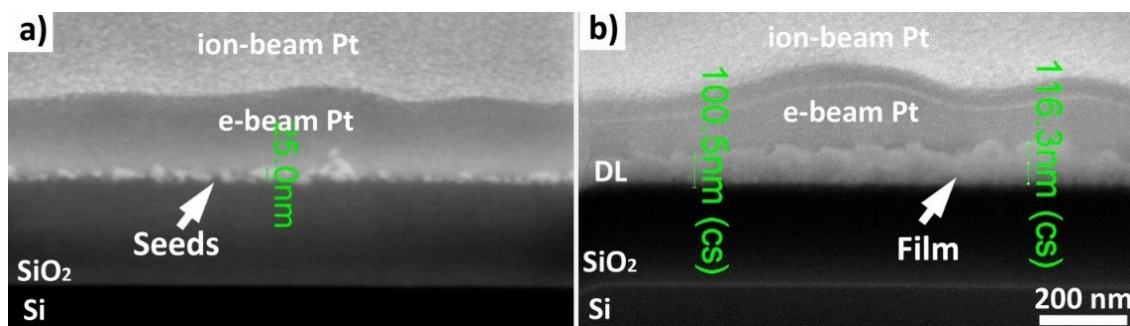


Figure 5.15: Cross-section of a) a single seed layer on Si wafer (300 nm SiO₂/p++ Si wafers) and b) ~100 nm ZnO thin film formed from 15-min hydrothermal growth on the seed layer. Ion-beam Pt and e-beam Pt represent the ion beam deposited and electron beam deposited platinum layers, respectively. DL is the dense layer.

The dense ZnO film in Figure 5.15 was more than 80% transparent in the visible spectrum, as shown in transmittance measurements (Figure 5.16a). This is comparable to studies by Kim et al. and Li et al., in which much thinner films (few nm) were fabricated via direct solution routes.^{96,97} To determine the optical band gap of the ZnO thin film, a relationship in which the absorption coefficient (α) of ZnO is a parabolic function of the incident energy ($h\nu$) and the optical band gap (E_g) was applied:

$$\alpha(h\nu) = A(h\nu - E_g)^{n/2}$$

where A is a function of the refractive index of the material, the reduced mass, and the speed of light in vacuum.¹²⁸ For a direct bandgap semiconductor like ZnO, n is equal to 1. The band edge of ZnO was evaluated from a plot of α^2 versus $h\nu$ by extrapolating the linear part of the curve to intercept the energy axis. The inset of Figure 5.16a exhibits the square of the absorption coefficient versus photon energy, showing that the bandgap of the ZnO film was 3.28 eV. This measured optical bandgap is smaller than the theoretical value of ZnO (3.37 eV), but it is still within the range that has been reported in other similar studies.^{118,129}

Electrical characterization was performed by fabricating ZnO TFTs. The drain current (I_d)-drain voltage (V_d) characteristics of the TFT at different gate voltages (V_g) were plotted in Figure 5.16b.

Since Ohmic contacts were constructed after depositing the Al contacts on the film, nearly straight line I_d - V_d curves were obtained. With increasing the gate voltage, the drain current increased as well, indicating that the film was n-type. The field-effect mobility, as extracted from the electrical characteristics, is $2.730 \text{ cm}^2/\text{V}\cdot\text{s}$ at zero back-gate bias. A high current at zero gate voltage may be attributed to a high concentration of defects, such as oxygen vacancies and zinc interstitials, in the thin film resulting from hydrothermal growth. The performance of ZnO thin film TFTs in terms of on-and-off ratio and current may be improved by annealing the films in oxygen at temperatures less than 300°C , as reported by Richardson.¹³⁰

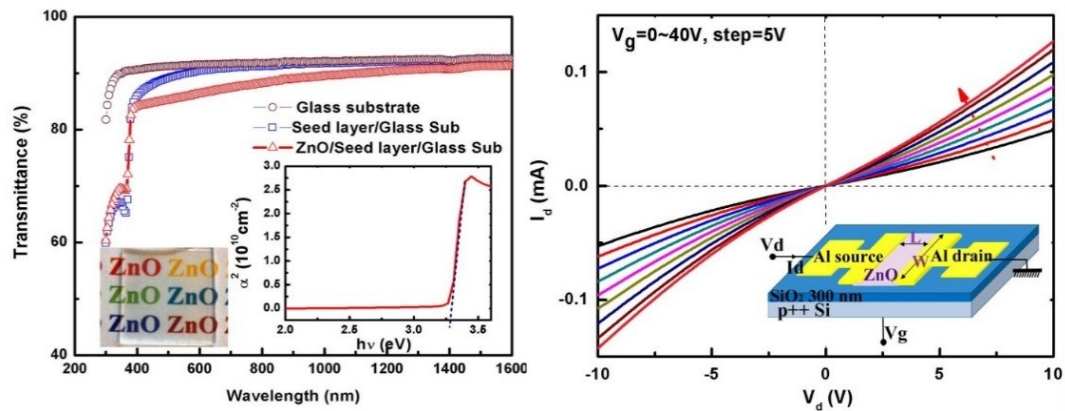


Figure 5.16: a) Transmittance spectrum of ZnO film with $\sim 100 \text{ nm}$ thickness on a glass substrate. The inset shows the square on the absorption coefficient versus photon energy. b) Current-voltage characteristics of ZnO film plotted for different back gate biases. Inset shows the configuration of devices.

5.3.2 Effects of Seed Layers on ZnO Thin Films

5.3.2.1 Seed Layer Characteristics

Solution growth is regarded as a cost-effective method to prepare thin films of semiconductor materials or transparent conductive oxides. Epitaxial growth or seed-assisted growth were employed during the solution growth in order to control the orientation, growth density, and properties of the resulting thin films. Epitaxial growth of ZnO thin films on GaN (0001), Au (111), and Mg₂AlO₄ (1010) substrates have been reported.¹³¹⁻¹³³ Despite highly textured films and good electronic properties, the single crystal substrates for epitaxy are expensive, or not compatible with flexible electronic applications. The pre-deposition of a seed layer of ZnO nanoparticles on the substrates is an alternative, cost-effective route to grow the high packing density ZnO thin film. It can facilitate the heterogeneous growth of ZnO nanorods and enable the growth of ZnO thin films on any substrate compatible with the solution growth condition. This advantage offers the possibility to grow ZnO thin films on non-crystalline and/or flexible polymer substrates. In this section, the effects of ZnO seed layers on the resulting polycrystalline ZnO thin films are discussed.

Figure 5.17 shows ZnO nanorods grown from a seed layer compared with ZnO nanorods grown on an untreated glass substrate. The use of a continuous seed layer serves as a template for the homoepitaxial growth of nanorods, thus efficiently increases the number density of nanorods grown on the substrate.

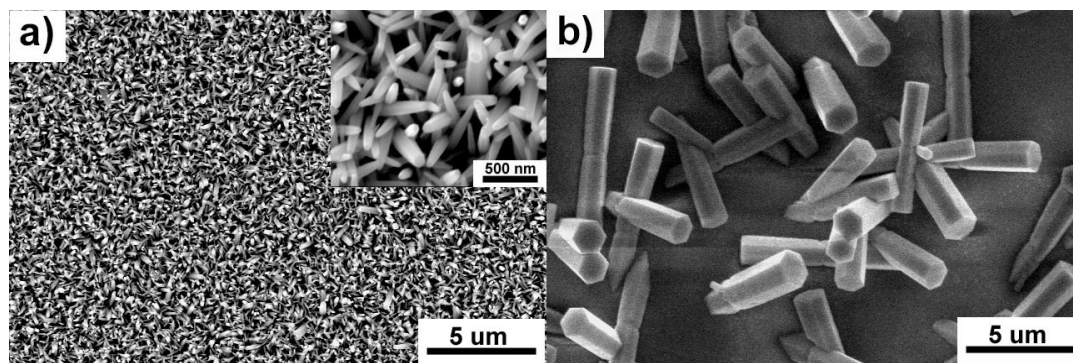


Figure 5.17: Anisotropic growth of ZnO nanorods from a solution of zinc nitrate and HMTA after 5 h on (a) a seeded glass substrate (nanoparticles with diameter ~ 70 nm) and (b) an unseeded glass substrate. The inset is morphology of nanorods at higher magnification.

In this study, two types of seed layers (SL1 and SL2) were prepared by the calcination of saturated $\text{Zn}(\text{Ac})_2$ precursor film at 350°C and 600°C for 1 h, respectively. Another type of seed layer (SL3) was deposited by PLD. Figure 5.18 shows the morphology of the three types of seed layers from the top-view and the side-view. The area density of the seed layer can be quantified by measuring the intergranular areas and calculating the ratio between the total area subtracted by the intergranular area and the total imaging area. The estimated areal densities for SL1, SL2, and SL3 are 14.3%, 11.1% and 0%, respectively. Due to the coarsening of pores during the higher temperature annealing, SL2 has larger gaps between some particles compared to SL1. According to the measurement performed on SEM images, the average in-plane diameter of grains in SL1 and SL2 are ~ 10 nm and ~ 40 nm, respectively. The thickness of SL1 and SL2 is similar to the average diameter of the particles, indicating single seed layers were obtained. Since the seed layer deposited by PLD is continuous, it is hard to measure the average diameter of the particles.

The phase purity of the calcinated SL1 and SL2 was confirmed by powder XRD (Figure 5.19). All the peaks within 2θ range of 20° to 70° corresponding to $(10\bar{1}0)$, (0002) , $(10\bar{1}1)$, $(10\bar{1}2)$, $(11\bar{2}0)$, $(10\bar{1}3)$, and $(11\bar{2}2)$ planes align with the standard XRD pattern of wurtzite ZnO (JCPDS 79-0206). A HRTEM image of a ZnO grain inside the calcinated SL1 confirms pure ZnO is formed

after annealing the $\text{Zn}(\text{Ac})_2$ precursors (Figure 5.18f). Based on Scherrer equation ($\tau = \frac{K\lambda}{\beta \cos\theta}$), the mean particle size of SL1, SL2, and SL3 are 12.2 nm, 36.3 nm, and 7.9 nm, respectively, which match with the measurements on SEM images. The degree of preferred c -axis orientation for the seed layers was estimated quantitatively by calculating Harris's texture coefficient, C_{hkl} , based on the XRD data. C_{hkl} is defined as

$$C_{hkl} = n \frac{I_m(hkil)/I_0(hkil)}{\sum_1^n I_m(hkil)/I_0(hkil)}$$

where $I_m(hkil)$ and $I_0(hkil)$ are the intensities of the measured peak corresponding to the (hkl) in the present sample and in a powder standard sample, respectively, and $n (\geq 1)$ is the total number of diffraction peaks considered in the evaluation. In this study, C_{0002} is evaluated by using above equation and seven diffractions ($n=7$): $(10\bar{1}0)$, (0002) , $(10\bar{1}1)$, $(10\bar{1}2)$, $(11\bar{2}0)$, $(10\bar{1}3)$, and $(11\bar{2}2)$, are taken into account for this texture coefficient calculation. C_{0002} can take value from ~ 1 to 7, which are two extremes representing a randomly oriented sample and a perfect oriented sample, respectively. Based on the calculation, SL1 and SL2 have similar C_{0002} are 0.84 and 0.97 respectively, while PLD has texture value as 7. This means the SL1 and SL2 are randomly oriented, while SL3 exhibits a perfect orientation along $\langle 0002 \rangle$ direction. Table 5.1 shows a summary of structural properties of the above three types of seed layers.

Table 5.1: Structural properties of ZnO seed layers.

Seed layer ID	Diameter (nm)	Number density ($\#/\mu\text{m}^2$)	Porosity (%)	C0002 (for n=7) (a.u.)
1	12.2	452	34.0	0.84
2	36.3	251	42.4	0.97
3	7.9	N/A	0	7

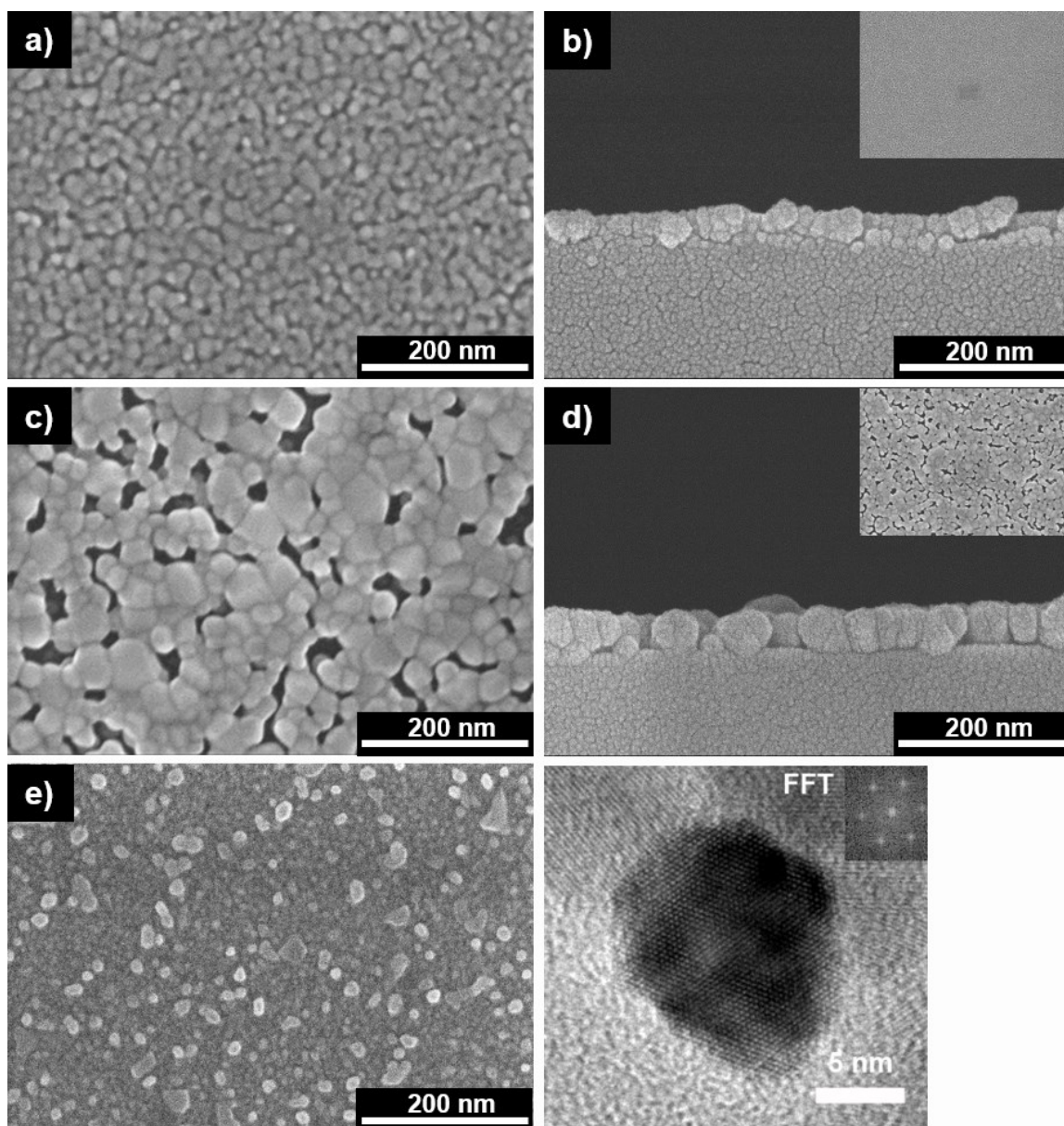


Figure 5.18: Top-view and side-view SEM images of three types of seed layers. a) and b) shows top-view and side-view images of SL1. c) and d) shows top-view and side-view images of SL2. e) shows top-view image of SL3. f) HRTEM image of a nanoparticle formed in SL1.

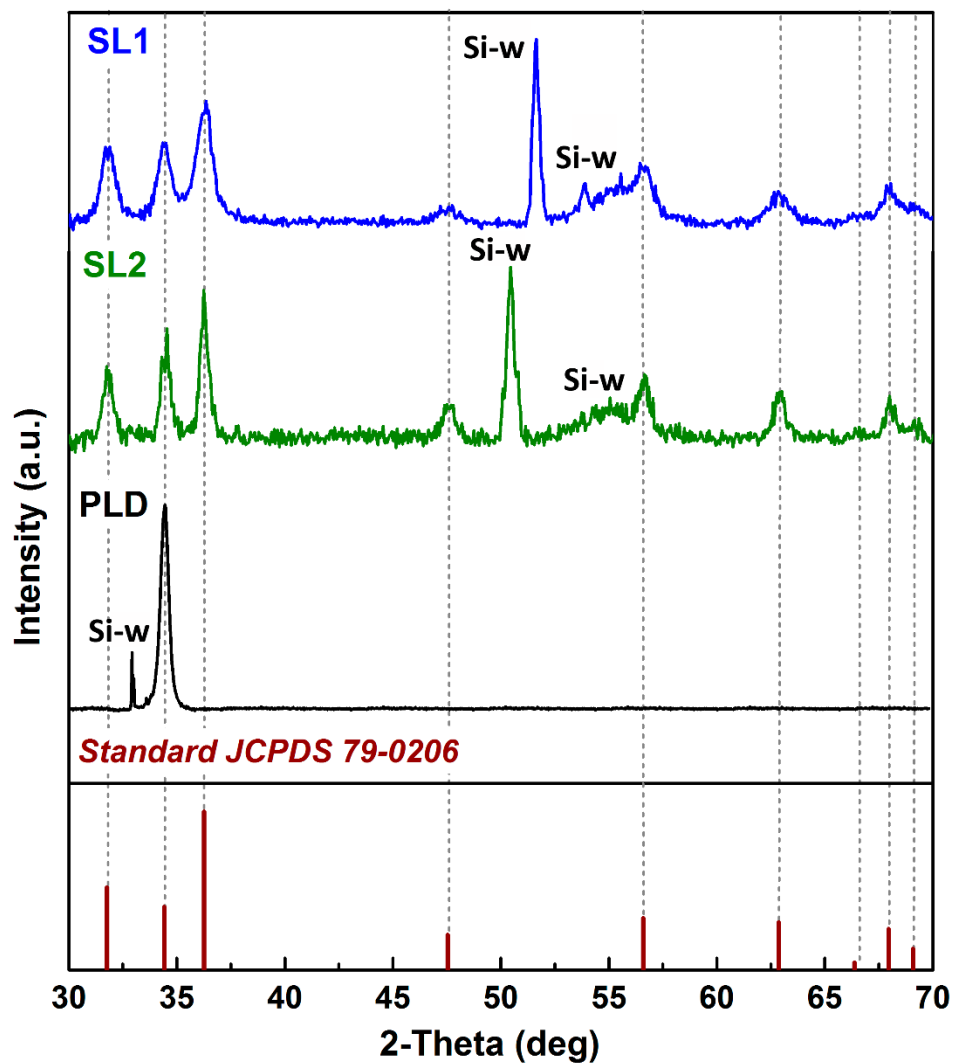


Figure 5.19: XRD patterns of the seed layers. The notation, Si-w, represents the peak/s contributed by SiO₂ (300 nm)/Si wafers. The peak/s are attributed to the miscut of Si wafer and the existence of crystalline SiO₂.

5.3.2.2 ZnO Thin Films Grown from Seed Layers

The ZnO films were grown from the three types of seed layers in Solution 1 comprising zinc nitrate and HMTA, and Solution 2 comprising zinc nitrate, HMTA, and KCl. After 120 min hydrothermal growth, all thin films show dominant orientations along [0001], as shown in Figure 5.20. Although SL1 and SL2 are randomly oriented, the films grown from them in both solutions

show textured structure at different levels. When Solution 1 is used, dominant peaks of (0002) and small peaks of (10 $\bar{1}$ 0) and (10 $\bar{1}$ 1) are observed in the XRD patterns. When Solution 2 is used, only (0002) peaks shows up in the XRD patterns. The film grown from perfectly-oriented SL3 in Solution 1 only exhibits the (0002) diffraction, indicating the texture was maintained after the hydrothermal growth. The results imply that the perfectly-oriented seed layer directly result in an oriented film, and the randomly-oriented seed layers can be grown into oriented films, especially when the growth behavior of individual nanorods are modified properly. The next experiment was performed to answer what are the major parameters of a seed layer controlling the structure of resulting films, and how the randomly-oriented seed layers grow into textured films from solutions.

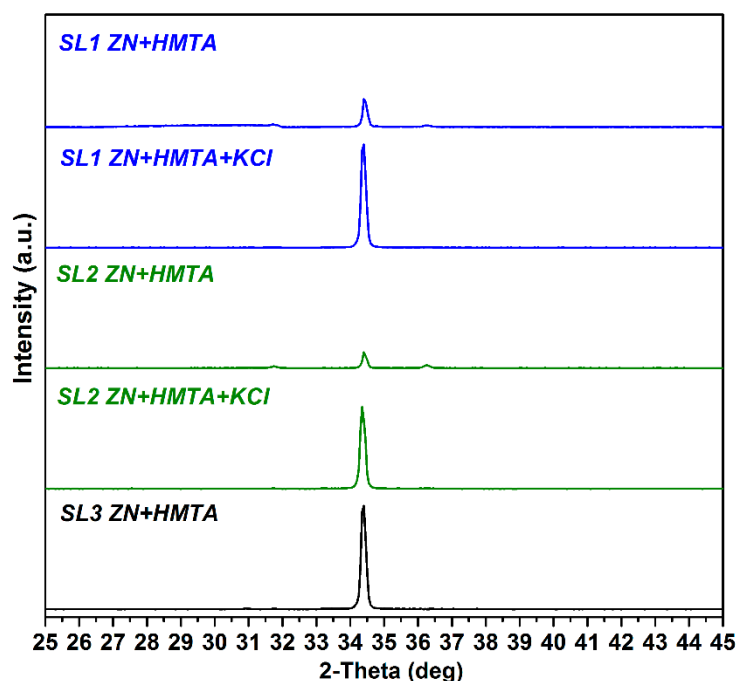


Figure 5.20: p-XRD of films grown on SL1 and SL2 from Solution 1 and Solution 2 and p-XRD of the film grown on SL3 from Solution 1.

The effects of seed layers on the resulting films in terms of average size, number density of nanorods, thickness, and texture were studied by comparing the films grown from SL1 and SL2 in

Solution 1 and Solution 2, respectively. The top-view and cross-sectional SEM images of the resulting ZnO films grown in different periods of time are shown in Figure 2.21 to Figure 2.24, and the corresponding statistic results of the average nanorod size, the nanorod density, and the film thickness are shown in Figure 5.25. The nanorods grown from SL2 have larger diameters than the nanorods grown from SL1 on matter which solution is used for growth (Figure 5.21 to Figure 5.25a). It can be concluded that the average diameter of individual nanorods have a positive relationship with the size of seeds. Another observation is that nanorods grown from Solution 2 on SL1 are much larger than those grown from Solution 1 on SL2 beyond 15 min hydrothermal growth (Figure 5.21, Figure 5.22, and Figure 5.25a). This indicates that rational modifying the anisotropic growth of individual nanorods can offset the size effect from the seed layer in order to grow larger nanorods.

When ZnO thin films were grown from Solution 1, the number density of nanorods grown on SL1 is much higher than that grown on SL2 (Figure 5.21 and Figure 5.25b). With the increase of the growth time, the number density of nanorods dropped continuously. When ZnO thin films were grown from Solution 2, the number density dropped significantly within 30 min growth compared to the growth in Solution 1. Beyond 30 min, the number density of rods in films grown from SL1 and SL2 are similar. There is a positive relationship between the number density of nanoparticles in a seed layer and the number density of nanorods grown from it. However, this influence can be diminished by changing the solution conditions. The enhanced later growth in Solution 2 accelerated the geometric selection, which significantly reduced the total number of nanorods.

The cross-sectional SEM images (Figure 5.23 and Figure 5.24) and the statistics of the film thicknesses (Figure 5.25c) show that the films grown in Solution 2 are thinner, but much denser compared to the films grown from Solution 1 for both SL1 and SL2 cases. As aforementioned, the films grown from both SL1 and SL2 in Solution 2 are more textured compared to the corresponding films grown in Solution 1 (Figure 5.20). The films grown from SL2 are less dense, but thicker than the films grown from SL1, while films grown from SL1 are more oriented along normal directions.

A geometric selection model is introduced to link these phenomena to the size and number density of seeds. The prerequisite of geometric selection is that the individual crystals adopt anisotropic growth behavior, meaning the crystal growth rate along one specific crystallographic direction is much faster than the rates along the other directions. There are three stages in the geometric selection: isolation, competition, and parallel growth. During the isolation growth stage, randomly oriented seeds grow independently, corresponding to the growth within 15 min in this study. The impingement between nanorods occurs when the crystals grow long enough to touch each other. This impingement stops the continual growth of those nanorods with growth direction deviated from the normal direction of the substrate. Therefore, only the nanorods with preferred orientation align with the normal direction of the substrates survive from this competition stage. The growth from 15 min to 120 min corresponds to the competition stage. The final stage is parallel growth stage when the survival nanorods continually grow along the preferred orientation, resulting in a textured film. The growth beyond 120 min should be in this stage. The competition stage is when the preferred orientation of the film starts to show up. The diameter of nanorods, the distance between nanorods, and the number density of nanorods determine when the impingement occurs and the frequency of the impingement. Therefore, SL1 which has higher nanorods density and smaller distance between the nanorods shows higher level of orientation. In addition, the more nanorods formed and impinged, the denser the film will be generated during the competition stage and the more survival nanorods continually grow during the parallel stage. This is the reason why denser film was grown from SL1 rather than SL2.

In conclusion, this section focuses on studying the effect of the seed layer to the morphology and orientation of the resulting film. The randomly oriented seed layer can be used for the growth of textured films composed of anisotropic nanorods. The size and number density of the particles in the seed layer directly influence the resulting film density and continuity by affecting the size and number density of nanorods grown from the seed layer. Modification in the solution condition can

enhance or diminish the influence from the seed layer. For example, for SL1 which is composed of small nanoparticles (few nm) and high number density of nanoparticles, the use of Solution 2 compensates the influence of the particle size while enhancing the influence of the number density. These results indicated that randomly oriented seed layer which are readily obtained using solution processing can be used for the growth of continuous ZnO thin film as long as the size, particle number density, and the solution condition are properly selected. This solution method can be applied to the growth of polycrystalline films of other crystals showing similar anisotropic growth behaviors, such as ZnS, ZnSe, CdS, CdSe, etc.

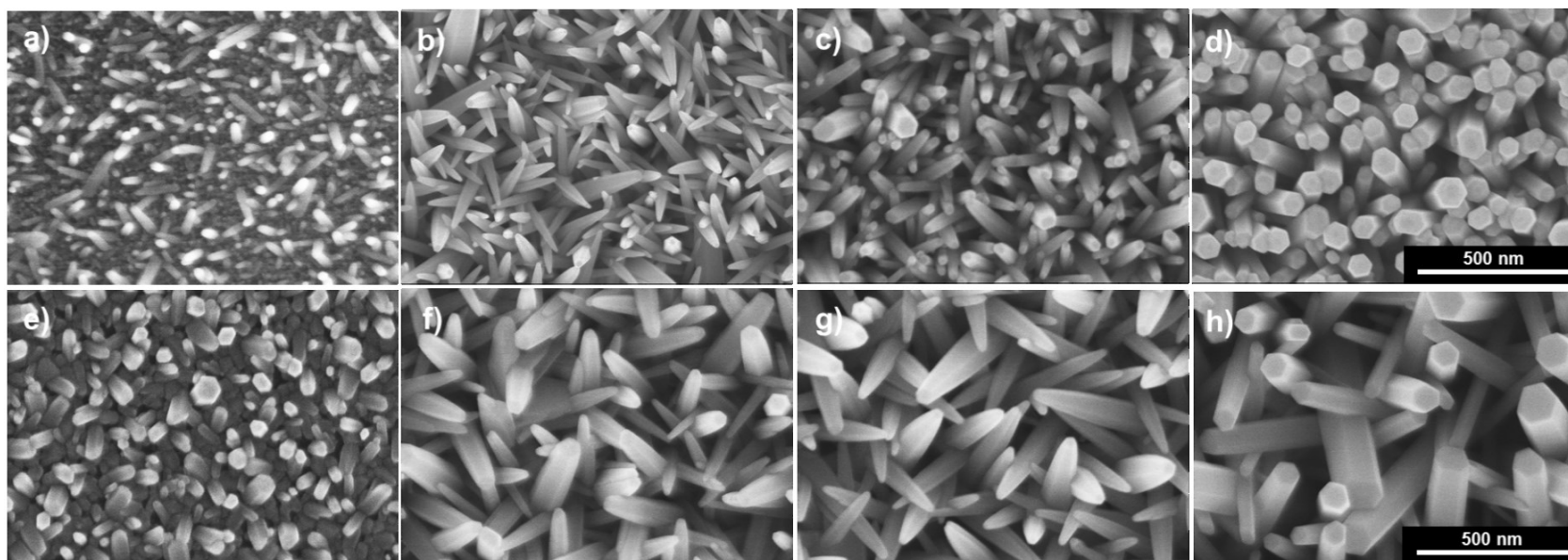


Figure 5.21: Top-view SEM images of ZnO films grown on SL1 and SL2 in solution 1. a)-d) films grown on SL1 for 15 min, 30 min, 60 min, and 120 min. e)-h) films grown on SL2 for 15 min, 30 min, 60 min, and 120 min.

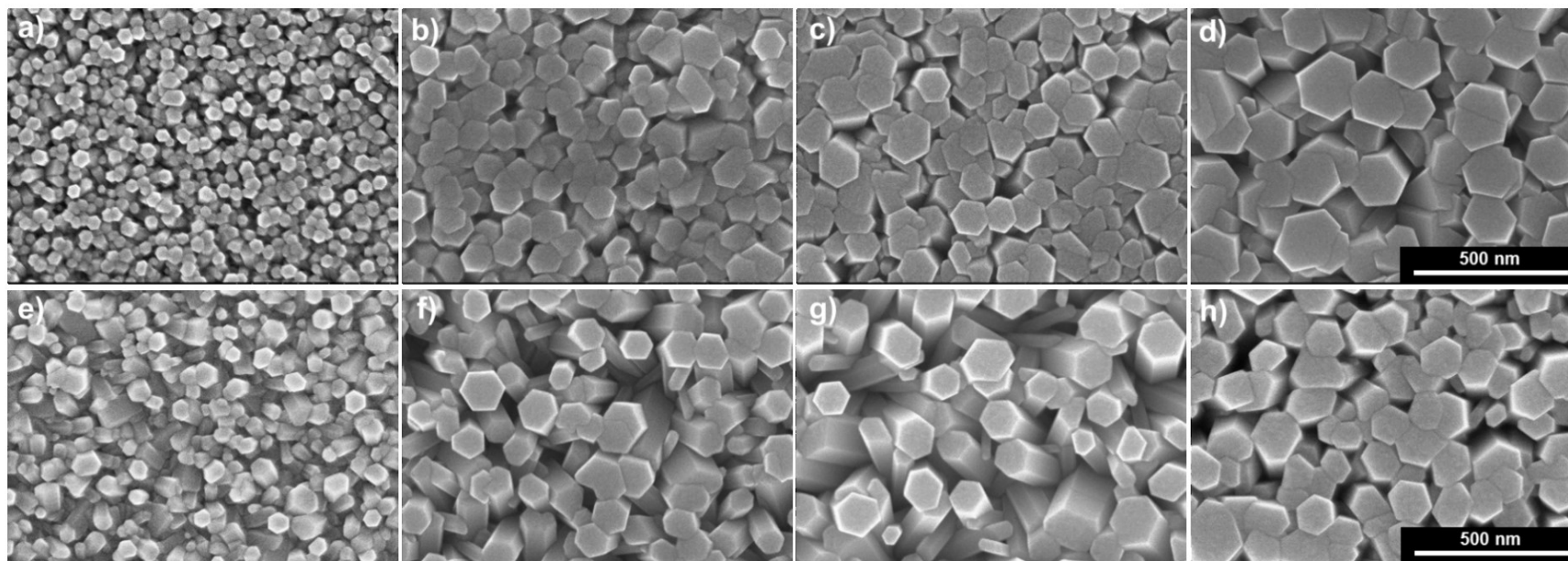


Figure 5.22: Top-view SEM images of ZnO films grown on SL1 and SL2 in solution 2. a)-d) films grown on SL1 for 15 min, 30 min, 60 min, and 120 min. e)-h) films grown on SL2 for 15 min, 30 min, 60 min, and 120 min.

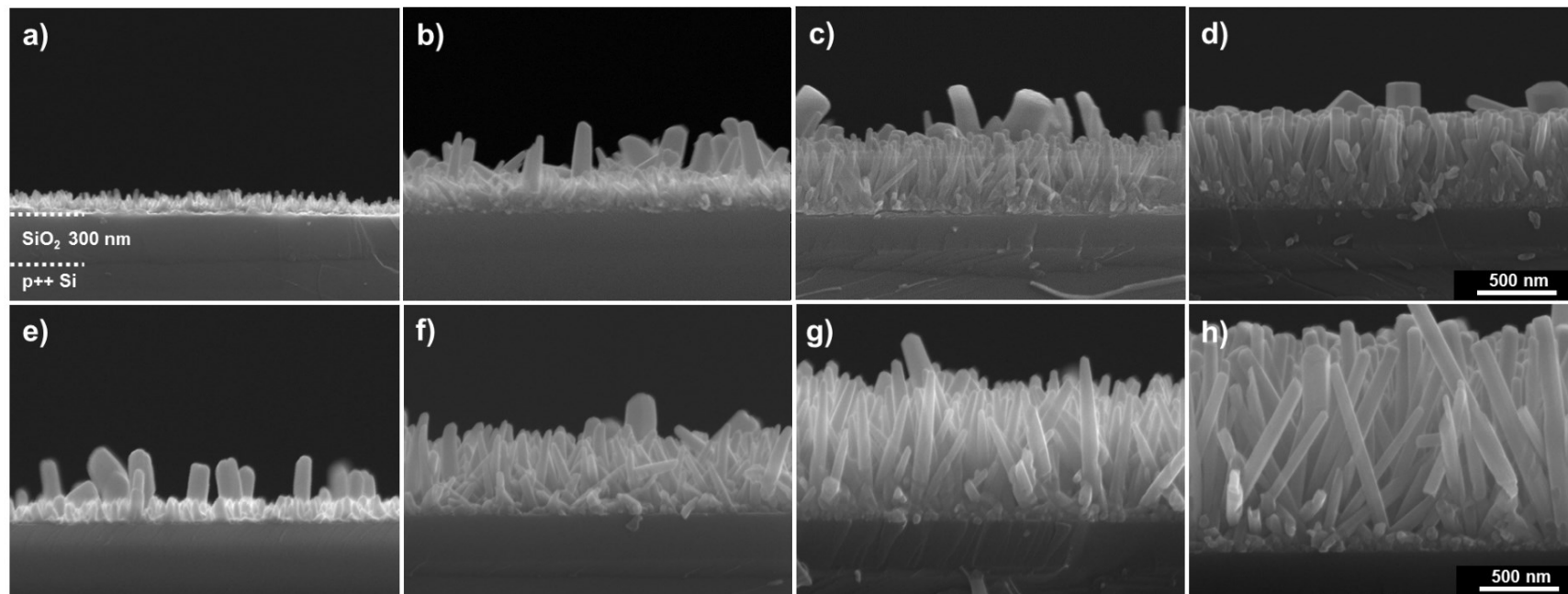


Figure 5.23: Cross-section SEM images of ZnO films grown on SL1 and SL2 in solution 1. a)-d) films grown on SL1 for 15 min, 30 min, 60 min, and 120 min. e)-h) films grown on SL2 for 15 min, 30 min, 60 min, and 120 min.

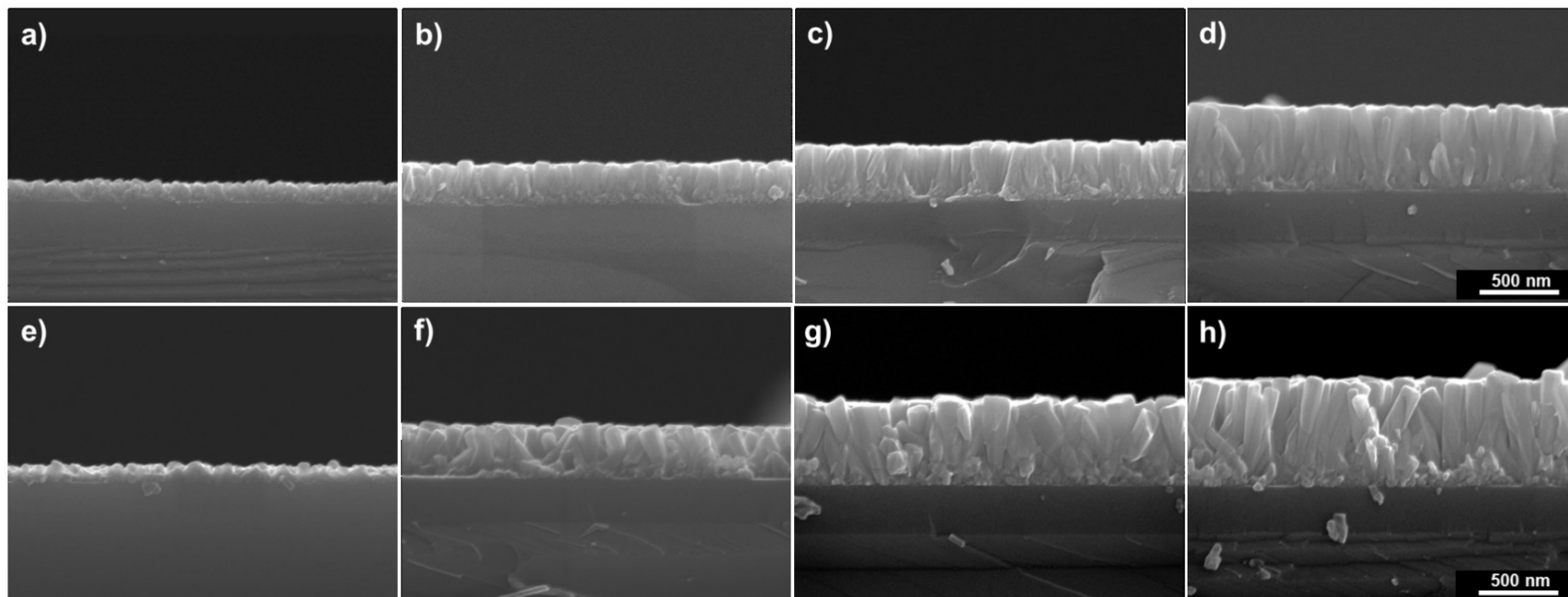


Figure 5.24: Cross-section SEM images of ZnO films grown on SL1 and SL2 in solution 2. a)-d) films grown on SL1 for 15 min, 30 min, 60 min, and 120 min. e)-h) films grown on SL2 for 15 min, 30 min, 60 min, and 120 min.

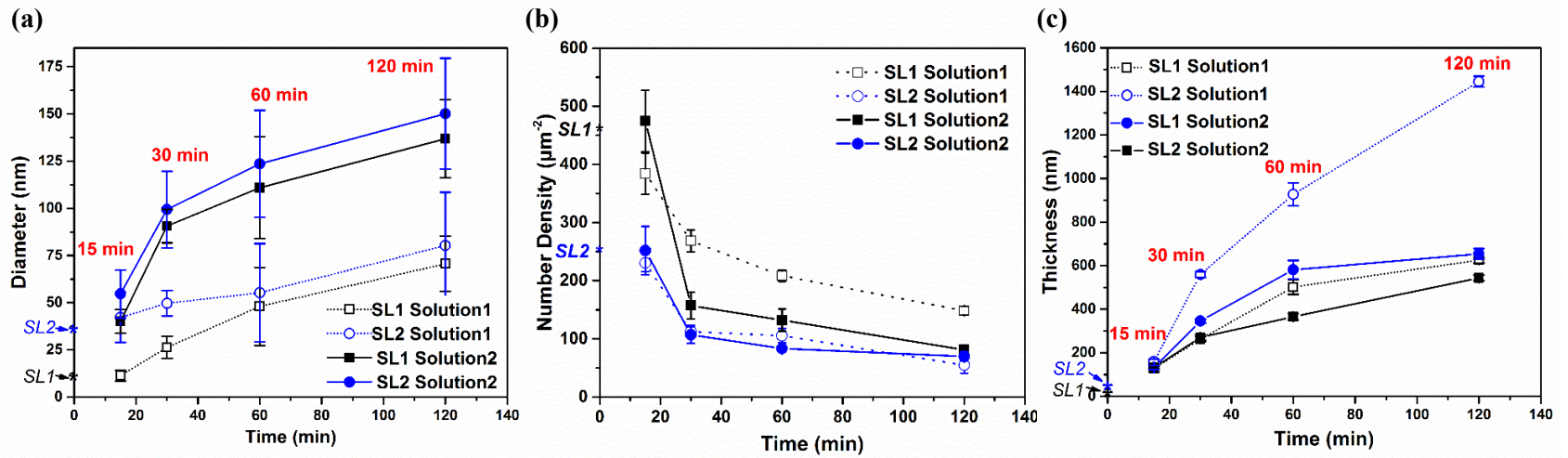


Figure 5.25: a) Average diameters of nanorods (plotted based on Figure 5.27), b) number density of nanorods, and c) film thickness versus growth time.

5.4 Conclusion

Continuous and dense polycrystalline ZnO thin films were grown from aqueous solutions under low temperature. The solution conditions and the seed layers have profound influences on the morphology of the resulting thin films. The effects of Cl⁻ ions and pH adjustment on the growth rate anisotropy of single ZnO crystals and the morphology of thin films were examined. Due to the capping effect of Cl⁻ ions on the Zn-terminated polar facets, the lateral growth, which is perpendicular to [0001] direction, was enhanced significantly during solution growth. ZnO nanorods grown from chloride-containing solutions have much larger diameters than those grown from chloride-free solutions. The competitive effects of Cl⁻ ions and HMTA on the anisotropic growth were confirmed by film growth under pH control. At a lower pH, the selective adsorption of Cl⁻ ions was the dominant factor in accelerating the lateral growth, and thus improving the film continuity. At a high pH, however, the preferred adsorption of HMTA on the non-polar facets enhanced the growth of thinner nanorods. After optimizing the growth condition, dense ZnO thin films were grown from the aqueous solutions of zinc nitrate and HMTA with $[Cl^-]/[Zn^{2+}] = 1.5$ and $pH = 4.8 \pm 0.1$. ZnO thin films with thicknesses of ~ 100 nm were grown from monolayers of seeds within 15 min. A good transparency and field effect were exhibited by the ZnO thin films, indicating the potential of using this solution method to fabricate printable electronics.

The effects of seed layers were studied. The size, number density, and orientation of nanoparticles in a seed layer directly determine the diameter, number density, and orientation of nanorods formed in the resulting film. The geometric selection mechanism explains how textured films grow from randomly-oriented seed layers during solution growth. It has been demonstrated that a dense and textured ZnO film can be grown from a randomly-oriented seed layer with a high nanoparticle number density (SL1 in this study) in the solution containing Cl⁻ ions. This advantage offers the opportunity to grow ZnO thin films on non-crystalline and/or flexible polymer substrates.

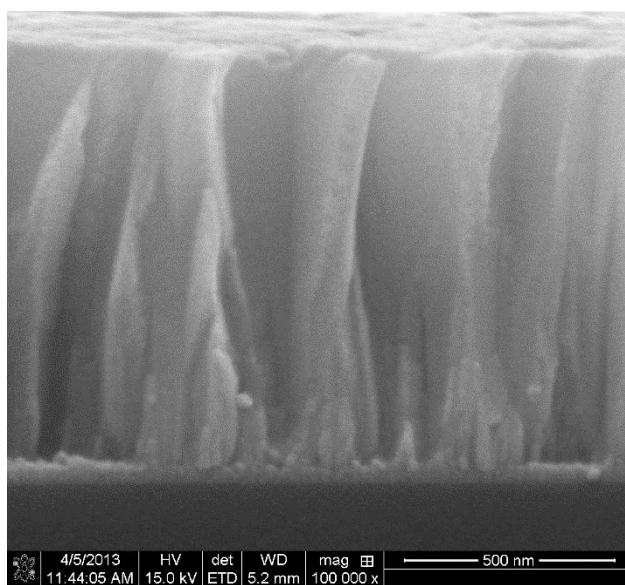
5.5 Supporting Information

Figure 5.26 Cross-sectional SEM image of a ZnO film grown from SL3 after 120-min solution growth.

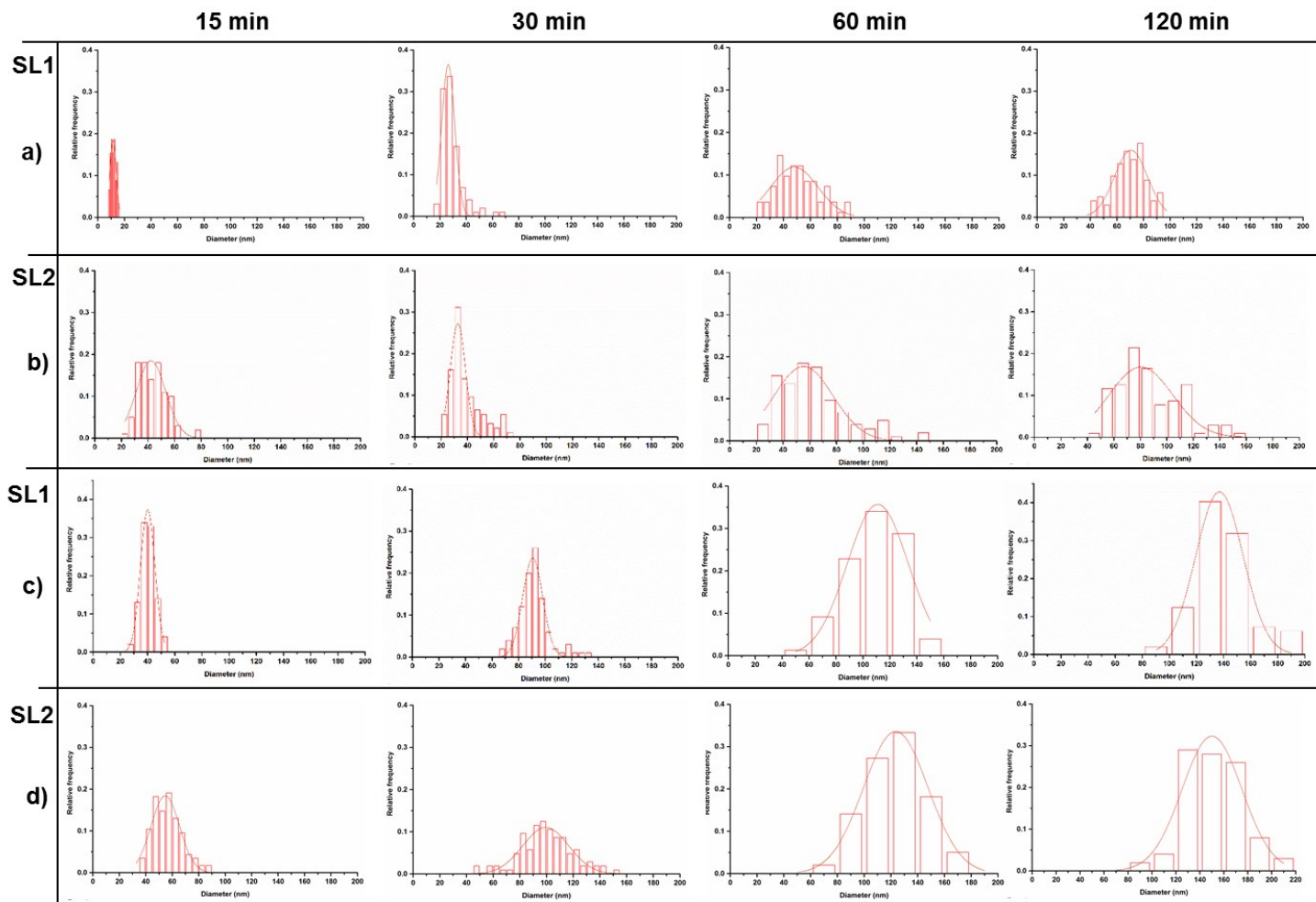


Figure 5.27: Distributions of nanorod diameters in films grown from SL1 and SL2 in Solution 1 (a and c) and Solution 2 (b and d).

CHAPTER 6. CONCLUSION

In this work, direct solution methods based on novel amine-thiol solvent mixtures have been developed to manufacture earth-abundant CZTSSe thin-film solar cells. The phase transformation and microstructural evolution from precursor films to CZTSSe polycrystalline films have been studied to gain insights in the relationship of processing-structure-performance of the CZTSSe absorber layers.

A primary amine-thiol solvent system is found for the rapid dissolution of metal salts, organometallic compounds, chalcogens, and chalcogenides. A CZTSSe molecular precursor was prepared by dissolving CuCl, ZnCl₂, SnCl₂, S, and Se in a solvent mixture of HA-PT at room temperature. After deposition and annealing processes, kesterite CZTS phase was formed with no secondary phases detected. The kesterite CZTS was converted into a high-crystallinity CZTSSe phase after selenization. The homogeneity of the precursor solution ensured phase purity in final films, and thus good solar cell performances. With this molecular precursor route, a power conversion efficiency of 7.86% (8.09%) has been achieved on a total area of 0.47 cm² (an active area of 0.456 cm²) under AM 1.5 illumination.

Despite the extremely low solubilities in most organic solvents, bulk metals (e.g. Zn, Cu, Sn, and In) and metal chalcogenides (e.g. Cu₂S, Cu₂Se, CuS, SnS, SnSe, In₂S₃, In₂Se₃, Ag₂S, and Ag₂Se) dissolve at high concentrations in primary-dithiol solvent mixtures at ambient conditions. Desired binary, ternary, and quaternary thin films, such as CuS, SnS, ZnS, Cu₂Sn(S_xSe_{1-x})₃ and Cu₂ZnSn(S_xSe_{1-x})₄ (0 ≤ x ≤ 1), were successfully deposited using the as-dissolved solutions or mixtures of constituent solutions. CZTSSe precursor solutions containing dissolved Zn, Cu/copper

sulfide/selenide, and Sn/tin sulfide/selenide in HA-EDT solvent mixtures were used for solar cell fabrication, and a solar cell PCE of 7.02% on a total area of 0.483 cm² has been achieved. Without introducing any impurity ion (e.g. O²⁻ or Cl⁻) in the absorber layers, this solution route becomes a robust and alternate approach to hydrazine-based solution route.

To understand the phase transformation and microstructural evolution during the heat treatment of solution-processed CZTSSe films, the precursor films were characterized under HRTEM after annealing, and the precursor films were selenized for different periods of time, and then characterized in terms of phases, compositions, and morphology. After annealing at low temperature, the solution-deposited film is composed of CZTSSe nanoparticles (1-4 nm) and amorphous materials. Within the first 5 min of selenization, the Se vapor has condensed and diffused throughout the precursor film. The large selenide grains nucleated at the top of the precursor film, then grew downward, forming a large-grained layer. The precursor film kept shrinking due to the out diffusion of Cu, Zn, and Sn to the large-grained layer. The densification in the final stage of selenization created a continuous film with a low porosity, which is desired for high-efficiency solar cells. The liquid-phase assisted grain growth is indicated by three facts during the selenization: 1) rapid cation transportation to the reaction front leads to the fast grain growth; 2) the maxima of Se concentration profile corresponds to where the large-grained layer ends; 3) a Se-rich fine-grained layer is formed after the final stage of selenization.

Solution-processed ZnO thin films are promising candidates for low-cost thin-film electronics. In this study, growth rate anisotropy of ZnO crystals and the film morphology were tuned by varying the concentrations of Cl⁻ ions and the initial pH of solutions. By using an optimized growth condition, [Cl⁻]/[Zn²⁺] = 1.5 and pH = 4.8 ± 0.1, dense ZnO films were fabricated within 15 min of solution growth. These films show >80% optical transmittance and field-effect mobilities of ~2.70 cm² V⁻¹ s⁻¹ at zero back-gate bias. The effects of seed layers were investigated systematically. The diameter, number density, and orientation of nanorods formed in thin films are influenced by

the size, number density, and orientation of nanoparticles in seed layers. However, it has been demonstrated that dense and textured ZnO films can be grown from randomly-oriented seed layers with high nanoparticle number densities by improving the lateral growth of individual nanorods. This advantage offers the opportunity to grow ZnO thin films on non-crystalline and/or flexible polymer substrates.

LIST OF REFERENCES

LIST OF REFERENCES

- (1) Ahn, S.; Jung, S.; Gwak, J.; Cho, A.; Shin, K.; Yoon, K.; Park, D.; Cheong, H.; Yun, J. H. *Appl Phys Lett* **2010**, *97*, 021905.
- (2) Chen, S.; Walsh, A.; Gong, X.-G.; Wei, S.-H. *Adv Mater* **2013**, *25*, 1522.
- (3) Guo, Q.; Ford, G. M.; Yang, W.-C.; Walker, B. C.; Stach, E. A.; Hillhouse, H. W.; Agrawal, R. *J Am Chem Soc* **2010**, *132*, 17384.
- (4) Katagiri, H.; Jimbo, K.; Maw, W. S.; Oishi, K.; Yamazaki, M.; Araki, H.; Takeuchi, A. *Thin Solid Films* **2009**, *517*, 2455.
- (5) Lindholm, F.; Fossum, J. G.; Burgess, E. L. *Electron Devices, IEEE Transactions on* **1979**, *26*, 165.
- (6) Luque, A.; Hegedus, S. *Handbook of photovoltaic science and engineering*; John Wiley & Sons, 2011.
- (7) US Department of Energy, N. **2010**, *Report no. TP-6A2-46025*, 1.
- (8) Ito, K.; Nakazawa, T. *Japanese Journal of Applied Physics* **1988**, *27*, 2094.
- (9) Katagiri, H.; Nishimura, M.; Onozawa, T.; Maruyama, S.; Fujita, M.; Sega, T.; Watanabe, T. *Power Conversion Conference-Nagaoka, Proceedings of IEEE*: **1997**, *2*, 1003.
- (10) Kessler, F.; Rudmann, D. *Sol Energy* **2004**, *77*, 685.
- (11) Visoly-Fisher, I.; Cohen, S. R.; Ruzin, A.; Cahen, D. *Adv Mater* **2004**; *16*, 879.
- (12) Solibro Press Release, *Hanergy's Solibro Has 20.5% CIGS Solar Cell Verified by NREL*, **2014**, http://www.pvtech.org/news/hanergys_solibro_has_20.5_cigs_solar_cell_verified_by_nrel.
- (13) First Solar Press Release, *First Solar Raises Bar for CdTe with 21.5% Efficiency Record*, **2014**, http://www.pv-magazine.com/news/details/beitrag/first-solar-raises-bar-for-cdte-with-215-efficiency-record_100018069/#axzz3svggPUI0.

- (14) Nikkei BP Clean Tech Institute, *NIMS Achieves 15% Efficiency with Perovskite PV Cell*, **2015**, http://techon.nikkeibp.co.jp/english/NEWS_EN/20150512/417866/?ST=msbe.
- (15) Liu, M.; Johnston, M. B.; Snaith, H. J. *Nature* **2013**, *501*, 395.
- (16) Hodes, G. *Science* **2013**, *342*, 317.
- (17) Kodigala, S. R. *Thin Film Solar Cells From Earth Abundant Materials: Growth and Characterization of Cu₂(ZnSn)(SSe) 4 Thin Films and Their Solar Cells*; Newnes, **2013**.
- (18) Mitzi, D. B.; Gunawan, O.; Todorov, T. K.; Wang, K.; Guha, S. *Solar Energy Materials and Solar Cells* **2011**, *95*, 1421.
- (19) Repins, I.; Beall, C.; Vora, N.; DeHart, C.; Kuciauskas, D.; Dippo, P.; To, B.; Mann, J.; Hsu, W.-C.; Goodrich, A.; Noufi, R. *Solar Energy Materials and Solar Cells* **2012**, *101*, 154.
- (20) Walsh, A.; Chen, S.; Wei, S. H.; Gong, X. G. *Adv Energy Mater* **2012**, *2*, 400.
- (21) Chen, S. Y.; Gong, X. G.; Walsh, A.; Wei, S. H. *Appl Phys Lett* **2010**, *96*.
- (22) Polizzotti, A.; Repins, I. L.; Noufi, R.; Wei, S.-H.; Mitzi, D. B. *Energ Environ Sci* **2013**, *6*, 3171.
- (23) Olekseyuk, I.; Dudchak, I.; Piskach, L. *J Alloy Compd* **2004**, *368*, 135.
- (24) Siebentritt, S.; Schorr, S. *Progress in Photovoltaics: Research and Applications* **2012**, *20*, 512.
- (25) Washio, T.; Shinji, T.; Tajima, S.; Fukano, T.; Motohiro, T.; Jimbo, K.; Katagiri, H. *J Mater Chem* **2012**, *22*, 4021.
- (26) Chawla, V.; Clemens, B. In *Photovoltaic Specialists Conference (PVSC), 2012 38th IEEE*; IEEE: **2012**, 002990.
- (27) Katagiri, H.; Jimbo, K.; Moriya, K.; Tsuchida, K. In *Photovoltaic Energy Conversion, 2003. Proceedings of 3rd World Conference on*; IEEE: **2003**; *3*, 2874.
- (28) Shin, B.; Gunawan, O.; Zhu, Y.; Bojarczuk, N. A.; Chey, S. J.; Guha, S. *Progress in Photovoltaics: Research and Applications* **2013**, *21*, 72.
- (29) Wang, K.; Gunawan, O.; Todorov, T.; Shin, B.; Chey, S.; Bojarczuk, N.; Mitzi, D.; Guha, S. *Appl Phys Lett* **2010**, *97*, 3508.

- (30) Weber, A.; Krauth, H.; Perlt, S.; Schubert, B.; Kötschau, I.; Schorr, S.; Schock, H. *Thin Solid Films* **2009**, *517*, 2524.
- (31) Cao, Y.; Denny, M. S., Jr.; Caspar, J. V.; Farneth, W. E.; Guo, Q.; Ionkin, A. S.; Johnson, L. K.; Lu, M.; Malajovich, I.; Radu, D.; Rosenfeld, H. D.; Choudhury, K. R.; Wu, W. *J Am Chem Soc* **2012**, *134*, 15644.
- (32) Guo, Q.; Hillhouse, H. W.; Agrawal, R. *Journal of the American Chemical Society* **2009**, *131*, 11672.
- (33) Guo, Q.; Kim, S. J.; Kar, M.; Shafarman, W. N.; Birkmire, R. W.; Stach, E. A.; Agrawal, R.; Hillhouse, H. W. *Nano Lett* **2008**, *8*, 2982.
- (34) Miskin, C. K.; Yang, W.-C.; Hages, C. J.; Carter, N. J.; Joglekar, C. S.; Stach, E. A.; Agrawal, R. *Progress in Photovoltaics: Research and Applications* **2014**, *23*, 654.
- (35) Riha, S. C.; Parkinson, B. A.; Prieto, A.L. *J Am Chem Soc* **2009**, *131*, 12054.
- (36) Steinhagen, C.; Panthani, M. G.; Akhavan, V.; Goodfellow, B.; Koo, B.; Korgel, B. A. *Journal of the American Chemical Society* **2009**, *131*, 12554.
- (37) Yang, W. C.; Miskin, C. K.; Hages, C. J.; Hanley, E. C.; Handwerker, C.; Stach, E. A.; Agrawal, R. *Chem Mater* **2014**, *26*, 3530.
- (38) Bag, S.; Gunawan, O.; Gokmen, T.; Zhu, Y.; Mitzi, D. B. *Chem Mater* **2012**, *24*, 4588.
- (39) Schnabel, T.; Löw, M.; Ahlswede, E. *Solar Energy Materials and Solar Cells* **2013**, *117*, 324.
- (40) Todorov, T.; Sugimoto, H.; Gunawan, O.; Gokmen, T.; Mitzi, D. B. *IEEE J Photovolt* **2014**, *4*, 483.
- (41) Todorov, T. K.; Gunawan, O.; Gokmen, T.; Mitzi, D. B. *Prog Photovoltaics* **2013**, *21*, 82.
- (42) Todorov, T. K.; Tang, J.; Bag, S.; Gunawan, O.; Gokmen, T.; Zhu, Y.; Mitzi, D. B. *Adv Energy Mater* **2013**, *3*, 34.
- (43) Xin, H.; Katahara, J. K.; Braly, I. L.; Hillhouse, H. W. *Adv Energy Mater* **2014**, *4*, 1301823.
- (44) Hages, C. J.; Levenco, S.; Miskin, C. K.; Alsmeyer, J. H.; Abou-Ras, D.; Wilks, R. G.; Bär, M.; Unold, T.; Agrawal, R. *Progress in Photovoltaics: Research and Applications* **2015**, *23*, 376.

- (45) Mitzi, D. B.; Todorov, T. K.; Gunawan, O.; Min, Y.; Qing, C.; Wei, L.; Reuter, K. B.; Kuwahara, M.; Misumi, K.; Kellock, A. J.; Chey, S. J.; de Monsabert, T. G.; Prabhakar, A.; Deline, V.; Fogel, K. E. In *Photovoltaic Specialists Conference (PVSC), 2010 35th IEEE 2010*, p 000640.
- (46) Wang, W.; Winkler, M. T.; Gunawan, O.; Gokmen, T.; Todorov, T. K.; Zhu, Y.; Mitzi, D. B. *Adv Energy Mater* **2014**, *4*, 1301465.
- (47) Carter, N. J.; Yang, W. C.; Miskin, C. K.; Hages, C. J.; Stach, E. A.; Agrawal, R. *Solar Energy Materials and Solar Cells* **2014**, *123*, 189.
- (48) Yang, W.-C.; Miskin, C. K.; Carter, N. J.; Agrawal, R.; Stach, E. A. *Chem Mater* **2014**, *26*, 3530.
- (49) Hsu, C.-J.; Duan, H.-S.; Yang, W.; Zhou, H.; Yang, Y. *Adv Energy Mater* **2014**, *4*, 1301287.
- (50) Yang, W.; Duan, H.-S.; Bob, B.; Zhou, H.; Lei, B.; Chung, C.-H.; Li, S.-H.; Hou, W. W.; Yang, Y. *Adv Mater* **2012**, *24*, 6323.
- (51) Park, S.-N.; Sung, S.-J.; Son, D.-H.; Kim, D.-H.; Gansukh, M.; Cheong, H.; Kang, J.-K. *Rsc Adv* **2014**, *4*, 9118.
- (52) Tian, Q.; Wang, G.; Zhao, W.; Chen, Y.; Yang, Y.; Huang, L.; Pan, D. *Chem Mater* **2014**, *26*, 3098.
- (53) Wang, G.; Zhao, W.; Cui, Y.; Tian, Q.; Gao, S.; Huang, L.; Pan, D. *ACS Appl Mater Interfaces* **2013**, *5*, 10042.
- (54) Agrawal, R.; Zhang, R. H.; Walker, B. C.; Handwerker, C. A. *Non-provisional Patent Application..US 14824913* **2015**.
- (55) Zhang, R.; Szczepaniak, S. M.; Carter, N. J.; Handwerker, C. A.; Agrawal, R. *Chem Mater* **2015**, *27*, 2114.
- (56) Grossberg, M.; Krustok, J.; Raudoja, J.; Timmo, K.; Altosaar, M.; Raadik, T. *Thin Solid Films* **2011**, *519*, 7403.
- (57) Fella, C. M.; Uhl, A. R.; Hammond, C.; Hermans, I.; Romanyuk, Y. E.; Tiwari, A. N. *J Alloy Compd* **2013**, *567*, 102.
- (58) Šćepanović, M.; Grujić-Brojčin, M.; Nesheva, D.; Levi, Z.; Bineva, I.; Popović, Z. V. *Acta Physica Polonica A* **2009**, *116*, 708.

- (59) Gokmen, T.; Gunawan, O.; Todorov, T. K.; Mitzi, D. B. *Appl Phys Lett* **2013**, *103*.
- (60) Hages, C. J.; Carter, N. J.; Agrawal, R.; Unold, T. *J Appl Phys* **2014**, *115*, 234504.
- (61) Hegedus, S. S.; Shafarman, W. N. *Progress in Photovoltaics: Research and Applications* **2004**, *12*, 155.
- (62) Jiang, C.; Liu, W.; Talapin, D. V. *Chem Mater* **2014**, *26*, 4038.
- (63) Carter, N. J.; Mainz, R.; Walker, B. C.; Hages, C. J.; Just, J.; Klaus, M.; Schmidt, S. S.; Weber, A.; Yang, W.-C. D.; Zander, O. *J Mater Chem C* **2015**, *3*, 7128.
- (64) Mainz, R.; Walker, B. C.; Schmidt, S. S.; Zander, O.; Weber, A.; Rodriguez-Alvarez, H.; Just, J.; Klaus, M.; Agrawal, R.; Unold, T. *Phys Chem Chem Phys* **2013**, *15*, 18281.
- (65) Denton, A. R.; Ashcroft, N. W. *Physical Review A* **1991**, *43*, 3161.
- (66) *Binary Alloy Phase Diagrams*; American Society for Metals, Materials Park, OH, **1986**.
- (67) Klenk, R.; Walter, T.; Schock, H. W.; Cahen, D. *Adv Mater* **1993**, *5*, 114.
- (68) Bragagnolo, J. A.; Barnett, A. M.; Phillips, J. E.; Hall, R. B.; Rothwarf, A.; Meakin, J. D. *Electron Devices, IEEE Transactions on* **1980**, *27*, 645.
- (69) Tang, J.; Huo, Z.; Brittman, S.; Gao, H.; Yang, P. *Nat Nano* **2011**, *6*, 568.
- (70) Okimura, H.; Matsumae, T.; Makabe, R. *Thin Solid Films* **1980**, *71*, 53.
- (71) Sinsersuksakul, P.; Hartman, K.; Bok Kim, S.; Heo, J.; Sun, L.; Hejin Park, H.; Chakraborty, R.; Buonassisi, T.; Gordon, R. G. *Appl Phys Lett* **2013**, *102*, 053901.
- (72) Ramakrishna Reddy, K. T.; Koteswara Reddy, N.; Miles, R. W. *Solar Energy Materials and Solar Cells* **2006**, *90*, 3041.
- (73) Lim, J.; Park, M.; Bae, W. K.; Lee, D.; Lee, S.; Lee, C.; Char, K. *Acs Nano* **2013**, *7*, 9019.
- (74) Shen, H.; Bai, X.; Wang, A.; Wang, H.; Qian, L.; Yang, Y.; Titov, A.; Hyvonen, J.; Zheng, Y.; Li, L. S. *Adv Funct Mater* **2014**, *24*, 2367.
- (75) Nakada, T.; Mizutani, M.; Hagiwara, Y.; Kunioka, A. *Solar Energy Materials and Solar Cells* **2001**, *67*, 255.

- (76) Catti, M.; Noel, Y.; Dovesi, R. *J Phys Chem Solids* **2003**, *64*, 2183.
- (77) Lu, M.-Y.; Song, J.; Lu, M.-P.; Lee, C.-Y.; Chen, L.-J.; Wang, Z. L. *Acs Nano* **2009**, *3*, 357.
- (78) Liu, H.; Shi, X.; Xu, F.; Zhang, L.; Zhang, W.; Chen, L.; Li, Q.; Uher, C.; Day, T.; Snyder, G. J. *Nat Mater* **2012**, *11*, 422.
- (79) Sassi, S.; Candolfi, C.; Vaney, J.-B.; Ohorodniichuk, V.; Masschelein, P.; Dauscher, A.; Lenoir, B. *Appl Phys Lett* **2014**, *104*, 212105.
- (80) Zhao, L.-D.; Lo, S.-H.; Zhang, Y.; Sun, H.; Tan, G.; Uher, C.; Wolverton, C.; Dravid, V. P.; Kanatzidis, M. G. *Nature* **2014**, *508*, 373.
- (81) Mitzi, D. B. *J Mater Chem* **2004**, *14*, 2355.
- (82) Mitzi, D. B. *Adv Mater* **2009**, *21*, 3141.
- (83) Mitzi, D. B.; Yuan, M.; Liu, W.; Kellock, A. J.; Chey, S. J.; Deline, V.; Schrott, A. G. *Adv Mater* **2008**, *20*, 3657.
- (84) Webber, D. H.; Brutchey, R. L. *Journal of the American Chemical Society* **2013**, *135*, 15722.
- (85) Webber, D. H.; Buckley, J. J.; Antunez, P. D.; Brutchey, R. L. *Chemical Science* **2014**, *5*, 2498.
- (86) Antunez, P. D.; Torelli, D. A.; Yang, F.; Rabuffetti, F. A.; Lewis, N. S.; Brutchey, R. L. *Chem Mater* **2014**, *26*, 5444.
- (87) Todorov, T. K.; Reuter, K. B.; Mitzi, D. B. *Adv Mater* **2010**, *22*, E156.
- (88) Yang, W.; Duan, H. S.; Cha, K. C.; Hsu, C. J.; Hsu, W. C.; Zhou, H.; Bob, B.; Yang, Y. *J Am Chem Soc* **2013**, *135*, 6915.
- (89) Rao, C. P.; Dorfman, J.; Holm, R. *Inorg Chem* **1986**, *25*, 428.
- (90) Minceva-Sukarova, B.; Najdoski, M.; Grozdanov, I.; Chunnillall, C. *Journal of molecular structure* **1997**, *410*, 267.
- (91) Chandrasekhar, H.; Humphreys, R.; Zwick, U.; Cardona, M. *Phys Rev B* **1977**, *15*, 2177.

- (92) McLeod, S. M.; Hages, C. J.; Carter, N. J.; Agrawal, R. *Progress in Photovoltaics: Research and Applications* **2015**.
- (93) K. Maeada, M. S., I Niikura, and T. Fukuda *Semicond Sci Tech* **2005**, *20*, S49.
- (94) Lin, W.; Chen, D.; Zhang, J.; Lin, Z.; Huang, J.; Li, W.; Wang, Y.; Huang, F. *Crystal Growth & Design* **2009**, *9*, 4378.
- (95) Jeong, I. S.; Kim, J. H.; Im, S. *Applied Physics Letters* **2003**, *83*, 2946.
- (96) Kim, K.; Park, S.; Seon, J.-B.; Lim, K.-H.; Char, K.; Shin, K.; Kim, Y. S. *Advanced Functional Materials* **2011**, *21*, 3546.
- (97) Li, C.-s.; Li, Y.-n.; Wu, Y.-l.; Ong, B.-S.; Loutfy, R.-O. *Journal of Materials Chemistry* **2009**, *19*, 1626.
- (98) Song, K.; Noh, J.; Jun, T.; Jung, Y.; Kang, H. Y.; Moon, J. *Advanced materials* **2010**, *22*, 4308.
- (99) Lawes, G.; Risbud, A. S.; Ramirez, A. P.; Seshadri, R. *Physical Review B* **2005**, *71*, 045201.
- (100) N. Golego, S. A. S., and M. Cocivera *J Electrochem Soc* **2000**, *147*, 1592.
- (101) Chu, S.; Li, D.; Chang, P.-C.; Lu, J. G. *Nanoscale Research Letters* **2010**, *6*, 38.
- (102) Carcia, P. F.; McLean, R. S.; Reilly, M. H.; Nunes, G. *Applied Physics Letters* **2003**, *82*, 1117.
- (103) Christoulakis, S.; Suche, M.; Katharakis, M.; Katsarakis, N.; Koudoumas, E.; Kiriakidis, G. *Reviews on Advanced Materials Science* **2005**, *10*, 331.
- (104) Yamaguchi, H.; Komiyama, T.; Yamada, M.; Sato, K.; Aoyama, T. *Physica B: Condensed Matter* **2007**, *39*, 401-402.
- (105) Zhaoyang, W.; Liyuan, S.; Lizhong, H. *Vacuum* **2010**, *85*, 397.
- (106) El-Shaer, A.; Mofor, A. C.; Bakin, A.; Kreye, M.; Waag, A. *Superlattices and Microstructures* **2005**, *38*, 265.
- (107) Y. Liu, C. R. G., S. Liang, N. Emanetogu, Y. Lu, H. Shen, and M. Wraback *J electrochem Mater* **2000**, *29*, 69.

- (108) Dulub, O.; Diebold, U.; Kresse, G. *Physical review letters* **2003**, *90*, 016102.
- (109) Vayssieres, L.; Keis, K.; Lindquist, S.-E.; Hagfeldt, A. *The Journal of Physical Chemistry B* **2001**, *105*, 3350.
- (110) Govender, K.; Boyle, D. S.; Kenway, P. B.; O'Brien, P. *Journal of Materials Chemistry* **2004**, *14*, 2575.
- (111) Guo, M.; Diao, P.; Cai, S. *Journal of Solid State Chemistry* **2005**, *178*, 1864.
- (112) Tak, Y.; Yong, K. *The Journal of Physical Chemistry B* **2005**, *109*, 19263.
- (113) Xu, S.; Adiga, N.; Ba, S.; Dasgupta, T.; Wu, C. F.; Wang, Z. L. *ACS nano* **2009**, *3*, 1803.
- (114) Xu, S.; Lao, C.; Weintraub, B.; Wang, Z. L. *Journal of Materials Research* **2011**, *23*, 2072.
- (115) Jiang, Z. Y.; Kuang, Q.; Xie, Z. X.; Zheng, L. S. *Adv Funct Mater* **2010**, *20*, 3634.
- (116) Hong, J. I.; Choi, J.; Jang, S. S.; Gu, J.; Chang, Y.; Wortman, G.; Snyder, R. L.; Wang, Z. L. *Nano letters* **2012**, *12*, 576.
- (117) Nicholas, N. J.; Franks, G. V.; Ducker, W. A. *CrystEngComm* **2012**, *14*, 1232.
- (118) Pradhan, D.; Leung, K. T. *Langmuir : the ACS journal of surfaces and colloids* **2008**, *24*, 9707.
- (119) Sun, Y.; Riley, D. J.; Ashfold, M. N. *The Journal of Physical Chemistry B* **2006**, *110*, 15186.
- (120) Liu, J.; Xu, L.; Wei, B.; Lv, W.; Gao, H.; Zhang, X. *CrystEngComm* **2011**, *13*, 1283.
- (121) Podlogar, M.; Richardson, J. J.; Vengust, D.; Daneu, N.; Samardžija, Z.; Bernik, S.; Rečnik, A. *Advanced Functional Materials* **2012**, *22*, 3136.
- (122) Yu, Q.; Fu, W.; Yu, C.; Yang, H.; Wei, R.; Li, M.; Liu, S.; Sui, Y.; Liu, Z.; Yuan, M. *The Journal of Physical Chemistry C* **2007**, *111*, 17521.
- (123) Lee, J. S.; Wiederhorn, S. M. *Journal of the American Ceramic Society* **2004**, *87*, 1319.
- (124) Sugunan, A.; Warad, H. C.; Boman, M.; Dutta, J. *Journal of Sol-Gel Science and Technology* **2006**, *39*, 49.

- (125) Read, C. G.; Steinmiller, E. M.; Choi, K.-S. *Journal of the American Chemical Society* **2009**, *131*, 12040.
- (126) Tena-Zaera, R.; Elias, J.; Wang, G.; Levy-Clement, C. *The Journal of Physical Chemistry C* **2007**, *111*, 16706.
- (127) Xu, L.; Guo, Y.; Liao, Q.; Zhang, J.; Xu, D. *The Journal of Physical Chemistry B* **2005**, *109*, 13519.
- (128) Tauc, J. *Amorphous and Liquid Semiconductors*; Springer **1974**, 159.
- (129) Gao, Y.; Nagai, M.; Chang, T.-C.; Shyue, J.-J. *Crystal Growth and Design* **2007**, *7*, 2467.
- (130) Richardson, J. J.; Lange, F. F. *J. Mater. Chem.* **2011**, *21*, 1859.
- (131) Joo, J. H.; Greenberg, K. J.; Baram, M.; Clarke, D. R.; Hu, E. L. *Crystal Growth & Design* **2013**, *13*, 986.
- (132) Nijikovsky, B.; Richardson, J. J.; Garbrecht, M.; DenBaars, S. P.; Kaplan, W. D. *Journal of Materials Science* **2013**, *48*, 1614.
- (133) Vispute, R.; Talyansky, V.; Choopun, S.; Sharma, R.; Venkatesan, T.; He, M.; Tang, X.; Halpern, J.; Spencer, M.; Li, Y. *Applied Physics Letters* **1998**, *73*, 348.

VITA

VITA

Ruihong Zhang was born in Chicheng, Hebei province in China. After living in Xi'an for 3 years, she moved to Beijing with her parents. She graduated from the Beijing National Day School in 2000. She first received a Bachelor Degree in Materials Engineering from Beijing University of Technology in June 2003. During her years at Beijing University, she was heavily involved in undergraduate research, and have led seminars for students in the Department of Materials Science and Engineering. She has presented her research work in MS&T'07 conference. Later, she then continued her Master's program with the guidance of Dr. Fu Guo in Beijing University of Technology. Her Master's thesis was related to the reliability of lead-free solar joints under current stressing. She was awarded her Master's Degree in June 2010.

In August 2010, Ruihong came to Purdue University to pursue her PhD. She was working on the research in hydrothermal growth of polycrystalline ZnO thin films, advised by Professor Carol Handwerker and Professor Elliott Slamovich, and later the solution processing of earth-abundant metal chalcogenide thin-film solar cells, guided by Professor Rakesh Agrawal and Professor Carol Handwerker.

PUBLICATIONS

PUBLICATIONS

R. Zhang, S. Cho, D. Lim, R. Agrawal, C. A. Handwerker, Metal-Metal Chalcogenide Molecular Precursors to Multinary Metal Chalcogenide for Electronic Device. (In Review, ChemComm)

R. Zhang, S. M. Szczepaniak, R. Agrawal, C. A. Handwerker, A Versatile Solution Route to Efficient $\text{Cu}_2\text{ZnSn}(\text{S},\text{Se})_4$ Thin Film Solar Cells, Chemistry of Materials. 2015, 27, 6.

R. Zhang, S. Cho, R. Agrawal, C. A. Handwerker, Metal-Chalcogen Precursors to $\text{Cu}_2(\text{Zn}, \text{Cd})\text{Sn}(\text{S},\text{Se})_4$ Thin-Film Solar Cells. (In preparation)

R. Zhang, E. Slamovich, C.A. Handwerker, Controlling growth rate anisotropy for formation of continuous ZnO thin films from seeded substrates, Nanotechnology, 2013, 24, 19. (Featured article)